Quantitative Multi-Phase Field Modeling of Polycrystalline Solidification in Binary Alloys

Quantitative Multi-Phase Field Modeling of Polycrystalline Solidification in Binary Alloys

By

Nana Ofori-Opoku, B.Eng

A Thesis

Submitted to the School of Graduate Studies

in Partial Fulfilment of the Requirements

for the Degree

Master of Applied Science

McMaster University

MASTER OF APPLIED SCIENCE (2009) McMaster University

(Department of Materials Science and Engineering) Hamilton, Ontario

TITLE: Quantitative Multi-Phase Field Modeling of Polycrystalline Solidification in Binary Alloys

AUTHOR: Nana Ofori-Opoku, B.Eng

SUPERVISORS: H.S. Zurob and N. Provatas

NUMBER OF PAGES: xii, 113

Abstract

This thesis develops a new quantitative multi-phase field model for polycrystalline solidification of binary alloys. We extend the thin interface formalism of Karma and co-workers to multiple order parameters. This makes it possible to model segregation and interface kinetics during equiaxed dendritic growth quantitatively, a feature presently lacking from polycrystalline or multi-phase solidification models. We study dendrite tip speed convergence as a function of interface width during free dendritic growth. We then analyze the steady state and grain coalescence properties of the model. It is shown that the model captures the correct physics of back diffusion and repulsive grain boundary coalescence as outlined by Rappaz and co-workers. Finally, the model is applied to simulate solidification and coarsening in delta-ferrite solidification.

Acknowledgements

I would like to express my sincerest thanks and gratitude to my supervisors, Drs. Hatem Zurob and Nikolas Provatas. If they had not taken a chance on me, this work would not have been possible. Their patience and insight was instrumental in my success and the success of this work. My thanks also goes to the respective research groups of which I am honoured to be a part.

To my family, for their support through this endavour, their encouragement when things seemed impossible and for their love, you have my thanks. Finally, I thank God. If not by His grace all this would have been for naught.

To my parents Emmanuel and Comfort Ofori

Table of Contents

List of Figures

List of Tables

Chapter 1

Introduction

The search for more innovative and optimum materials has sparked wide spread research into such areas as, solidification, grain growth, coarsening and solid-state transformation. The aim of this research has, in principle, been to allow us to influence microstructure evolution and properties, which affect many material properties. There have generally been two approaches to examining microstructure. One is experimental, based largely on observation and characterization. The latter is via the use of theoretical models. In the area of solidification modeling, models range in scope from semi-empirical geometrical models to the more recent phase field models, which have been proven to be robust enough to self-consistently model the physics of complex microstructure development in some classes of alloys. This thesis will be concerned with the development of a new phase field model for quantitative solidification, growth and interactions of polycrystalline grains in binary alloys.

Industrial casting has evolved significantly in the past few decades. More economical and energy efficient casters and processing facilities are becoming dominant. The need then to understand the solidification process in its entirety becomes paramount for the continual progress and evolution of alloys. To focus on a practical example, consider delta ferrite, the primary phase solidified in steel. Its behavior during the growth and coarsening process becomes more important than ever to understand, since it determines the downstream outcomes. While a great deal of modeling research –phase field or otherwise– has been focused on the properties of isolated dendritic

growth or directional solidification, less work, by comparison, has been committed to address the complex behavior of equiaxed dendritic growth process that dominates the interior cast structure. This thesis will address the latter problem.

It is the ultimate aim of this work to develop a tool that can be used to efficiently simulate segregation and coarsening in late stage solidification of aluminum and steel alloys. This phase of the work will develop the model and demonstrate its properties using steel as an example system. In the sequel, we will be applying it to a systematic study of coarsening in Al alloys.

The remainder of this thesis is organized as follows. Chapter 2 will briefly review solidification and grain growth, Chapter 3 will introduce the phase field method as it pertains to our work. We will then introduce our model and its derivation in Chapter 4, followed by a discussion in Chapter 5 on its numerical implementation on an adaptive mesh for simulation efficiency. The same chapter also examines the steady state and coalescence properties of the model. We then apply our model to the study of solidification and coarsening of δ ferrite in Chapter 6. Conclusions and suggestions of future directions for this work are summarized in Chapter 7.

Chapter 2

Review of Solidification

2.1 Introduction

Solidification is a phase transformation process from a liquid state to a solid state. An understanding of the process and its relation to microstructure morphology, is paramount in influencing and controlling the mechanical properties of the final solid product.

The most fundamental structure in a complete solid is that of a single grain, emerging from a single dendrite, emerging from a single nucleation event. The most fundamental and extensively studied solidification microstructure is the dendrite. The term dendrite generally includes the familiar tree-like structures as well as cellular and seaweed-like patterns. Much of the work in solidification has focused on understanding and characterizing the physics of dendritic growth. Some of this work is reviewed here.

2.2 Modeling Solidification

2.2.1 Nucleation

When a liquid system is undercooled below its melting temperature, a driving force is generated for solidification. This driving force, for nucleation, is $G = G_l - G_s$ and is proportional to the induced undercooling (ΔT). Figure 2.1 shows a typical plot

of ΔG. The driving force then determines the probability of a nucleation event. This can be *heterogeneous*, where a nuclei forms by aid and in the presence of impurities, or *homogeneous* where a nuclei forms from the liquid due to the presence of thermal fluctuations.

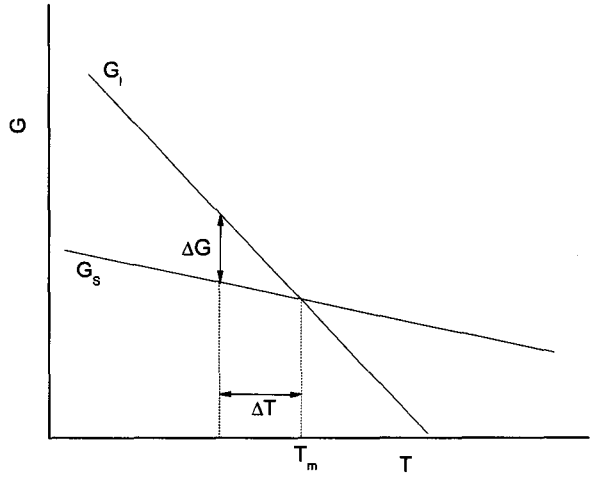

Figure 2.1: Solid and Liquid free energies as a function of temperature. Adapted from [1].

2.2.1.1 Homogeneous nucleation

In a given volume, the free energy associated with the formation of a nucleus is given by

$$G_{\text{hom}} = V\Delta G + A_{sl}\gamma_{sl}, \tag{2.1}$$

where V is the volume of the solid nucleus, A_{sl} the area of the solid-liquid interface and γ_{sl} is the solid-liquid interfacial energy. The energy difference, i.e. driving force,

is a negative quantity at a given temperature below melting, leading to the reduction of the over all free energy. However the creation of the solid nucleus introduces a separation, an interface, between the bulk phases which contributes a positive quantity to the energy. The total free energy, G_{hom}, can then assume a minimum based on the shape that the nucleus assumes. For the isotropic case, the shape that minimizes the energy is a sphere of radius r. We then have

$$G_{\text{hom}} = \frac{4}{3}\pi r^3 \Delta G + 4\pi r^2 \gamma_{sl}. \tag{2.2}$$

It is evident that because of the separate contributions from the volumetric and interfacial energies, that there exists a threshold for the radius of the sphere, below which a solid will not grow and would rather dissolve to maintain a minimum in the free energy. Applying $dG_{\text{hom}}/dr = 0$ and solving for r, we find the minimum or so-called critical radius and corresponding free energy, i.e. activation energy barrier, to be

$$r^*_{\text{hom}} = -\frac{2\gamma_{sl}}{\Delta G} \tag{2.3}$$

and

$$G^*_{\text{hom}} = \frac{16\pi\gamma^3_{sl}}{3\Delta G^2} \tag{2.4}$$

2.2.1.2 Heterogeneous nucleation

Heterogeneous nucleation often occurs at an undercooling less than that needed for homogeneous nucleation. This form of nucleation results from a decrease in the solid-liquid interfacial energy. Heterogeneous nucleation occurs in contact with impurities

in the melt. This then introduces new interfacial energies that must be considered in the free energy. When this impurity is the mould wall in contact with the liquid, we now take into account the mould-liquid interfacial energy, γ_{ml}, and the solid-mould interfacial energy, γ_{sm}. The associated free energy of such a situation is

$$G_{\text{het}} = V\Delta G + A_{sl}\gamma_{sl} + A_{sm}\gamma_{sm} - A_{sm}\gamma_{ml}. \tag{2.5}$$

where $\gamma_{ml} = \gamma_{sm} + \gamma_{sl}\cos\theta$ [1]. If the shape that minimizes the free energy is that of a sphere, with an assumed wetting contact angle, θ, to the mould wall, then

$$G_{\text{het}} = \left\{\frac{4}{3}\pi r^3\Delta G + 4\pi r^2\gamma_{sl}\right\}S(\theta). \tag{2.6}$$

where $S(\theta) = (2 + \cos\theta)(1 - \cos\theta)^2/4$ takes into account the contributions from the other interfacial energies and wetting angle. Now aside from $S(\theta)$, Eq. (2.6) is the same as that obtained for the homogeneous case, Eq. (2.2). Thus following in an analogous manner, we have the critical radius and corresponding energy barrier being

$$r^*_{\text{het}} = -\frac{2\gamma_{sl}}{\Delta G} \tag{2.7}$$

and

$$G^*_{\text{het}} = \frac{16\pi\gamma^3_{sl}}{3\Delta G^2}S(\theta) \tag{2.8}$$

Equation (2.8) reveals that the critical radius is independent of such impurities in the melt, while the energy barrier for the heterogeneous event is smaller by the factor $S(\theta)$ than that for the homogeneous case. This can be attributed to the assumed shape based on contact and the varying interfacial energies involved.

2.2.2 Kinetics of Solidification

Any solidification event entails the extraction of latent heat from a melt. Once nucleation has occurred and the nucleus grows, heat is transported away from the melt to the surrounding environment. This allows the formation of a solid, which is accompanied by the release of latent heat, and also allows the solid forming to reach the temperature of the surrounding environment. Considering the solidification of a pure material, one would have two diffusion equations to solve, each applied to the appropriate phase. This would be, assuming equal conductivities, densities and heat capacities for solid and liquid respectively,

$$\rho c_P \frac{\partial T}{\partial t} = \frac{\partial}{\partial x}\left(k_{cond}\frac{\partial T}{\partial x}\right) + \frac{\partial}{\partial y}\left(k_{cond}\frac{\partial T}{\partial y}\right) + \frac{\partial}{\partial z}\left(k_{cond}\frac{\partial T}{\partial z}\right), \tag{2.9}$$

where T is the temperature, ρ the density, c_P is the volumetric heat capacity for the pure material and k_{cond} is the thermal conductivity. At the fixed boundaries of the mould, suitable boundary conditions must be applied. An example of such a condition is that of zero flux. However at the moving solid-liquid interface, two conditions must be satisfied simultaneously, heat flux conservation and continuity of temperature,

$$L_f v_n = k_{cond}\frac{\partial T}{\partial n}\bigg|_s - k_{cond}\frac{\partial T}{\partial n}\bigg|_l, \tag{2.10}$$

and

$$T_{\text{interface}} \equiv T_s \equiv T_l = T_m - \Gamma\kappa - \beta v_n \tag{2.11}$$

where L_f is the latent heat released at the interface, v_n is the normal velocity of the interface, and the gradients in temperature are normal to the solid-liquid interface. In Eq. (2.11), also known as the Gibbs-Thomson condition, T_s and T_l are the interface

temperatures on the solid and liquid side of the interface respectively, T_m is the melting temperature of the pure material, β a kinetic coefficient and Γ is Gibbs-Thomson constant defined as,

$$\Gamma = \frac{\gamma_{sl} T_m}{L_f} \tag{2.12}$$

γ_{sl} is the surface tension and κ is the local curvature of the interface.

For the solidification of an alloy, we have analogous equations, where now concentration is the diffusing field. Specifically, the two main mechanisms at the interface, are release and diffusion of heat and the rejection and diffusion of solute. Since heat is assumed to diffuse more quickly than solute, temperature is often taken as a constant or spatially frozen. An additional simplification often made is to assume a so-called "one-sided" model of solidification, which assumes zero diffusivity in the solid. This serves as a good approximation since diffusion in solid may be orders of magnitude less than that of the liquid, generally 10^{-3}–10^{-5} that of the liquid in metals. For the special case of isothermal solidification, we have the following set of equations;

$$\frac{\partial c}{\partial t} = \frac{\partial}{\partial x}\left(D_l \frac{\partial c}{\partial x}\right) + \frac{\partial}{\partial y}\left(D_l \frac{\partial c}{\partial y}\right) + \frac{\partial}{\partial z}\left(D_l \frac{\partial c}{\partial z}\right), \tag{2.13}$$

$$c_l(1-k)v_n = -D_l \frac{\partial c}{\partial n}\bigg|_l, \tag{2.14}$$

$$c_l = \frac{c_o}{k} - \frac{\gamma_{sl} T_m}{|m_l| L_f}\kappa - \beta v_n, \tag{2.15}$$

where D_l is the liquid diffusion coefficient, v_n is the normal interface velocity, β the kinetic coefficient, c_o is the average solute composition of the alloy, γ_{sl} the surface

tension, T_m* the alloy melting temperature, m_l the liquidus slope, L_f the latent heat of fusion, κ is the local radius of curvature, k is the partition coefficient,

$$k \equiv \frac{c_s}{c_l}, \tag{2.16}$$

where c_s and c_l are the concentrations of the solute at the solid and liquid sides of the interface.

Combined, Eqs. (2.13–2.15) comprise a set of sharp interface equations that describe an isothermal alloy solidification at some fixed temperature below the liquidus. Equation (2.13), is the solute diffusion equation, Ficks Law, Eq. (2.14) is the mass conservation equation required at the solid-liquid interface and Eq. (2.15) is the alloy equivalent of the Gibbs-Thomson condition.

It should be noted that numerically, sharp interface models have several limitations. The mesh points that describe the interface must be tracked at all time. This is difficult in two dimensional simulations and becomes increasingly harder in three dimensions. Another important draw back is topological in nature. That being the inability to be able to properly handle interfaces that merge or impinge (in the case of polycrystalline growth). Generally, modeling complex microstructures in 2D and 3D with sharp interface models requires expert levels of prowess in numerical methods; numerical implementation of the phase field models is trivial by comparison. Yet another important limitation is that real materials do not have a sharp-interface, but indeed have a finite boundary layer (usually nano-scopic) which can strongly influence the kinetics of solidification.

*For dilute binary alloys, T_m is taken as the melting temperature of the majority component

2.2.3 Solutions of Sharp Interface Equations

A number of theories have emerged in an attempt to describe the growth of a single dendrite. Such descriptions involve measures of velocity of the tip, curvature of the tip, undercooling and their inter-relationship. The details of the derivation and analysis of the models and theories that exist is outside the scope of this thesis, hence we present a summary of the notable characteristics and results following the compilation of Saito [3] for a pure material.

2.2.3.1 Dendritic growth: parabolic tip

In the case of diffusion limited growth, no steady state solutions for velocity exists for the growth of a planar or spherical crystal [3]. However, if the crystal exists in local equilibrium, we allow for infinitely fast kinetics, and ignore surface tension, Ivantsov showed that a crystal with a parabolic tip grows steadily [4; 3]. The tip undercooling, velocity and radius are related by

$$\Delta = Pe^{P}E_1(P), \tag{2.17}$$

which is explicitly written as

$$\Delta = \sqrt{\pi P}e^{P}\mathrm{erfc}(\sqrt{\mathrm{P}}), \tag{2.18}$$

where $\Delta = (Tm - T_\infty)/L_f c_P^{-1}$ is the undercooling, with T_∞ being the far field bulk temperature, P is the Peclet number defined as

$$P = \frac{R}{l_d} = \frac{RV}{2\alpha}, \tag{2.19}$$

where R is the radius of crystal, V the velocity, and α the thermal diffusivity. Here, $E_1(P)$ is the exponential integral function of the form

$$E_1(P) = \int_P^\infty \frac{e^{-x}}{x} dx. \tag{2.20}$$

Finally, L_f is the latent heat of fusion and c_P the volumetric specific heat of the material, assumed equal in both phases.

The Ivantsov relation, Eq. (2.17), relates undercooling to tip speed and radius, but it does not allow us to determine V and R independently. Specifically, it is the product VR that is determined, which allows for an infinite number of solutions.

2.2.3.2 Instability of flat interface

The possibility of providing a second relationship to Eq. (2.17) was first addressed by a linear analysis performed by Mullins and Sekerka, and is now referred to as the Mullins-Sekerka instability [5; 6]. Their analysis begins by considering an undercooled crystal in a melt. In this scenario when latent heat is released it will be transported through the crystal rather than through the melt. If due to some fluctuations, parts of the crystal begin to grow faster than others, without capillarity, the crystal soon recovers a flat profile, since latent heat is transported less effectively at these fluctuation. However if the effect of surface tension is considered, the surface tension lowers the amount of undercooling at the growing fluctuations due to a positive curvature. This decrease in undercooling, lowers the driving force, thereby decreasing the growth rate of the growing fluctuations. The overall stability can then be stated as the struggle between the destabilizing effect of diffusion and the stabilizing effect due to energetics.

The stability analysis begins with assuming a sinusoidal perturbation with wavelength $\lambda = 2\pi/q$ of the interface as

$$\zeta(x, y; t) = Vt + a_q \exp(\omega_q t)\cos(qx). \tag{2.21}$$

ω_q is the growth rate corresponding to the wave number q, and specifies the stability of the flat interface. The interface is stable for negative ω_q and unstable for positive ω_q. Since the nature of the temperature is affected by the perturbation of the interface, it will also have an additional variation due to the perturbed interface. This variation is assumed to have the same form as Eq. (2.21), with a different amplitude a_q. After Eq. (2.21) and its corresponding perturbation for temperature are inserted into the diffusion equation, terms containing $\cos(qx)$ are collected. When the conservation equation and local equilibrium conditions are applied, a so-called dispersion relation is the result which gives an equation for the growth rate, namely,

$$\frac{\omega_q}{\alpha} = (\frac{2}{l_d} - d_o q^2)|q|\sqrt{1 - \frac{2d_o}{l_d} + \frac{d_o^2 q^2}{4}} - \frac{3d_o q^2}{l_d} + \frac{d_o^2 q^4}{2}. \tag{2.22}$$

where the wavelength corresponding to the maximum of Eq. 2.22 is $\lambda_s = 2\pi\sqrt{d_o l_d/2}$ for the case where solid diffusion is neglected, often called the "one-sided" case.

If surface tension is not considered in the stability analysis, i.e. $d_o = 0$, it is seen that

$$\frac{\omega_q}{\alpha} = \frac{2}{l_d}|q|. \tag{2.23}$$

Equation (2.23) is then always positive for all wave numbers, meaning that the interface is always unstable. However with out the stabilizing effect of surface tension, the result is an irregular structure, so-called fractal dendrite. There is a fractal the-

ory relevant to dendritic growth and the interested reader is referred to Ref. [3] for further more indepth information. Various attempts were made to associate the so-called Mullins and Sekerka instability wavelength λ_s to the structure of the dendrite (for example the tip radius) in order to provide a second relation between R and V, which could be used along with Eq. (2.17) to determine unique values for R and V vs. undercooling. These predictions, however, were to prove incorrect, without adding ad-hoc fitting parameters [7; 8; 9].

2.2.3.3 Microscopic solvability

Microscopic solvability is the most recent self-consistent theory that provided a second relationship between the velocity, radius and undercooling. Along with unique predictions of V and R, the theory also predicted that dendrite growth was impossible without anisotropic surface energy and that the possible values of dendrite tip speed are quantized. This theory is reviewed next.

Capillarity introduces a new characteristic length into Ivantsov's analysis. The capillary length $d_o = \gamma_{sl} c_P T_m / L_f^2$, which being a product of material parameters may be expected to scale other length scales in the analysis such as the tip radius, ρ, and the diffusion length l_d. The capillary length enters the analysis[†] via the surface stiffness $\tilde{\beta}$, or surface tension, β. Assuming a four fold rotational symmetry,

$$\beta(\theta) = \beta_o(1 + \tilde{\epsilon}\cos 4\theta). \tag{2.24}$$

The surface stiffness is then given by

[†]Shown here in two dimensions for simplicity.

$$\tilde{\beta} = \beta + \frac{\partial^2 \beta}{\partial \theta^2} = \beta_o(1 - 15\tilde{\epsilon}\cos 4\theta), \tag{2.25}$$

and the capillary length is given by

$$d = d_o(1 + \epsilon \cos 4\theta), \tag{2.26}$$

with d_o being the isotropic value of the capillary length and $\epsilon = 15\tilde{\epsilon}$ the strength of the anisotropy. From our previous discussion, we recall that when capillarity is considered there is a minimum stability length of $\lambda_s = 2\pi\sqrt{d_o l_d/2}$, such that if the dendrite tip radius is smaller than this wavelength it results in a stable flat interface while if the tip radius is larger that λ_s, there is an instability and the tip is on the order λ_s. A dimensionless parameter, the stability parameter, is thus introduced;

$$\sigma \equiv \frac{d_o l_d}{\rho^2} = \frac{d_o}{\rho P} = \frac{2\alpha d_o}{V\rho^2} = \frac{d_o V}{2\alpha P^2}. \tag{2.27}$$

The stability parameter scales with the capillary length, and that being contained in the Gibbs-Thomson condition, the stability parameter is coupled to the curvature, κ.

In applying an appropriate boundary condition to solve for the sharp interface equations, it is realized that far down the tail of the dendrite, one approaches the Ivantsov solution since the curvature becomes quite small. However, the condition that the gradient of the thermal field is symmetric (i.e. vanishes in the direction tangential to) the dendrite tip leads to a solvability condition for the stability parameter σ. The condition has the following main conclusions; (i) neglecting surface anisotropy, i.e. $\epsilon = 0$, does not give rise to a steady state dendritic growth, (ii)consideration of surface anisotropy, i.e. $\epsilon \neq 0$, results in a symmetric dendrite tip with steady state growth and tip oriented in the minimum of the surface stiffness, and (iii) the stability

parameter is a function of the anisotropy strength and results in the tip radius and velocity satisfying the scaling relation,

$$V\rho^2 = \frac{2\alpha d_o}{\sigma(\epsilon)} = \frac{2\alpha d_o}{\sigma_o}\epsilon^{-7/4}, \tag{2.28}$$

for small ϵ and σ. Combining Eq. (2.28) with the Ivantsov relation Eq. (2.18), the tip radius and velocity can be found uniquely for specific undercooling as

$$\rho = \frac{d_o}{\sigma_o}\frac{\epsilon^{-7/4}}{P(\Delta)} \sim d_o\frac{\pi}{\sigma_o}\Delta^{-2}\epsilon^{-7/4}, \tag{2.29}$$

$$V = \frac{2\alpha\sigma_o}{d_o}P^2(\Delta)\epsilon^{7/4} \sim \frac{2\alpha\sigma_o}{\pi^2 d_o}\Delta^4\epsilon^{7/4}. \tag{2.30}$$

The results of microscopic solvability have been verified for pure nickel in levitation experiments [10].

2.3 Late Stage Grain Growth, Coarsening and Solid State Processes

Solidification sets the initial dendritic network, however the final microstructure is also a product of the coarsening and interface kinetics that proceed the impingement of grains. This process is reviewed here.

During an annealing process of a polycrystalline material, the average size of grains increases. The process is driven by both diffusion and the reduction in interfacial energy, i.e. grain boundary energy. During this process, some grains decrease in size while others increase, this process is what is referred to as *grain growth*. This process can occur in single phase materials with crystals of varying orientations in close proximity. However when it occurs in materials where there exists a dissimilar

phase that separates the grains, it is referred to as *coarsening* [11; 12; 13]. Though the two are often used interchangeably, they are different and separate mechanisms are at work.

Fundamentally the underlying process during grain growth is the transfer of atoms across the grain boundary from one grain to another. While in coarsening, it is the separation of atoms (or components) from a grain, transport that occurs through the dissimilar phase and finally its precipitation onto the other grain [13]. Another process, which precedes both the above mentioned processes (grain growth and coarsening) is that of dendrite bridging or *coalescence.* This occurs during the last stages of solidification. This process characterizes the bridging of dendritic arms and grains, forming one coherent solid.

2.3.1 Grain Growth and Coarsening

There has been extensive research in grain growth and coarsening. Experimental work in this area has lead to theories characterizing their kinetics. The most relevant of these are summarized.

When solidification is complete in a polycrystalline system, due to the high grain boundary energy that exists at the joined interfaces of two or more grains, the system is in a meta-stable state. Experimental observations have noted that upon subjecting the system to a sufficiently high temperature (close to the melting temperature of the system), the average grain size (based on average $\langle d \rangle$), will increase [13].

The rate of change of $\langle d \rangle$ is inversely proportional to the amount of interface, which itself is inversely proportional to $\langle d \rangle$. However, the rate at which $\langle d \rangle$ changes is proportional to a constant K, which clearly has to be proportional to the surface energy. So the larger this constant K, the faster the grains want to grow to put

distance between its bulk and the receding interface. This can be put mathematically as;

$$\frac{d\langle d\rangle}{dt} = \frac{K}{\langle d\rangle}. \tag{2.31}$$

The exact solution of Eq. (2.31) is

$$\langle d\rangle - \langle d_0\rangle = Kt^{\frac{1}{2}}, \tag{2.32}$$

where $\langle d_0\rangle$, is the initial average diameter at $t = 0$, and K is generally a positive time-dependent constant [14; 15; 16; 17]. According to literature, the constants K and n (grain growth exponent) seem to be a product of the various factors that affect the process. Based on experimental observations, under ideal conditions and in systems of adequate purity, $n = 1/2$ [18] as in Eq. (2.32), gives the so-called *parabolic growth law*. However since conditions are always less than ideal, small exponents are usually reported in the presence of impurities [19; 20] or precipitation [21]. In the case of grain coarsening, diffusion of impurities to/from the interface changes the kinetics, amounting to an effective exponent $n = 1/3$ in Eq. (2.32) [22].

There are several reviews available for the reader interested in a more indepth look at this topic, the theory, history and future trends [11; 12; 23].

2.3.2 Coalescence

There has been an increasing interest recently to understand the atomic kinetics governing the impingement and merger of grain boundaries. This is driven by issues such as hot tearing, grain boundary melting at temperatures below bulk melting and effects of liquid films on grain boundaries. The point at which the final den-

dritic network forms a coherent solid network (coalescence)[‡], how it occurs and its consequences has been studied extensively [24; 25; 26; 27] but still has many open questions.

Rappaz and co-workers in Ref. [2], have recently put forth a set of sharp interface equations that describe the final stage solidification of dendrite arms and grains. They are reviewed here in some detail as they will be used later on by us to benchmark the appropriateness of our phase field theory to handle dendritic coalescence. This thermodynamically based work has been applied to cracking in super alloys [28], coalescence of equiaxed grains [29], an extension to consider multi-component alloys [30] and most recently to consider fluid flow in the mushy region [31].

According to the work of Rappaz and co-workers, a planar solid-liquid interface will coalesce only at a given undercooling of ΔT_b. For pure materials this undercooling is given by, the phenomenological expression

$$\Delta T_b = \frac{\Delta \Gamma_b}{\delta} = \frac{\gamma_{gb} - 2\gamma_{sl}}{\Delta s_f} \frac{1}{\delta}, \tag{2.33}$$

where δ is the thickness of an individual solid-liquid interface, $\Delta \Gamma_b$ is like a Gibbs-Thomoson coefficient, which is the difference between the grain boundary energy, γ_{gb}, and twice the solid-liquid interfacial energy $2\gamma_{sl}$ divided by the entropy of fusion Δs_f.

Based on research that has treated the coalescence of droplets and films utilizing the so-called "disjoining pressure" [32](which is based on van der Waals forces of attraction and repulsion), they proceed to describe coalescence in late stage solidification. This pressure leads to a negative or positive contribution depending on

[‡]This in past literature has been referred to as dendrite coherency point. It occurs when the impinging dendrite arms have formed a cohesive solid network with sufficient strength to sustain a tensile stress

the attraction or repulsion of the droplets. With this in mind and carefully considering the undercooling, ΔT_b, we realize that 3 distinct 'interfaces' can be distinguished. They are; (i) *attractive*, characteristic of dendrite arms belonging to the same primary trunk or between two crystals where there is zero misorientation. This gives $\gamma_{gb} = 0$ or $\gamma_{gb} < 2\gamma_{sl}$ and results in a very unstable liquid film allowing interfaces to merge immediately when within a distance δ from each other,(ii) *neutral*, where $\Delta T_b = 0$ and $\gamma_{gb} = 2\gamma_{sl}$ and (iii) *repulsive*, which results in $\gamma_{gb} > 2\gamma_{sl}$ due to $\Delta T_b > 0$[§]. In the latter case, this implies that there exists, at least until the given undercooling approaches ΔT_b, a stable liquid phase of finite thickness. When considering the solidification of an alloy, it is of importance to realize that coalescence is also greatly influenced by concentration of solute in the liquid film. This will be explored further in this thesis.

It should be noted that the distance, h, between the approaching grains affects the determinable excess energy, which becomes the grain boundary energy (γ_{gb}) when the distance is zero. Figure 2.2 depicts this trend of interface separation on excess energy. In order to quantify this excess energy, Rappaz and co-workers proposed the relation

$$\gamma(h) = 2\gamma_{sl} + (\gamma_{gb} - 2\gamma_{sl}) \exp\left(-\frac{h}{\delta}\right), \tag{2.34}$$

where δ is the interface thickness of an individual interface. The excess free energy of the combined system of two interfaces and a liquid film is thus given by,

[§]A grain boundary is attractive if no energy is required for coalescence and repulsive if a driving force is required for the last liquid film to vanish. This driving force is determined by the undercooling ΔT_b.

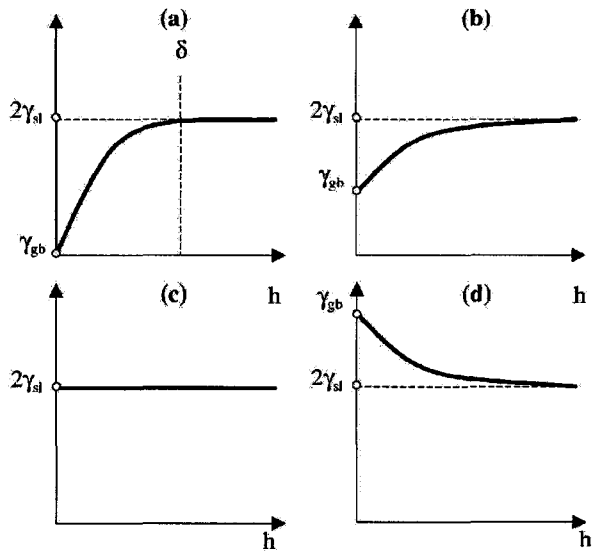

Figure 2.2: Excess energy of solid-liquid interface as a function of the width, h, between interfaces,. (a) no misorientation, $\gamma_{gb} = 0$. (b) $\gamma_{gb} < 2\gamma_{sl}$ (attractive boundary); (c)$\gamma_{gb} = 2\gamma_{sl}$ (neutral); (d) $\gamma_{gb} > 2\gamma_{sl}$ (repulsive boundary). Adapted from [2].

$$\begin{aligned} G(h) =& (G_l - G_s)h + \gamma(h) \\ =& L\frac{T_m - T}{T_m}h + \gamma(h) \\ =& \Delta s_f h \Delta T + \gamma(h), \end{aligned} \tag{2.35}$$

where G_l and G_s are the bulk liquid and solid free energies respectively. It can be easily shown that at a temperatures T, different from the melting temperature T_m , there will exist a minimum in Eq. (2.35), $h = h_{\min}$, which corresponds to a stable grain boundary liquid layer. Minimizing Eq. (2.35) using Eq. (2.34) gives the critical undercooling,

$$\Delta T^* = \frac{\gamma_{gb} - 2\gamma_{sl}}{\Delta s_f}\frac{1}{\delta}\exp\left(-\frac{h^*}{\delta}\right). \tag{2.36}$$

When $h^* = 0$ in the above equation, it is evident that there will be no liquid and coalescence occurs for the appropriate undercooling of ΔT_b given by Eq. (2.33).

The formulation of one dimensional sharp interface equations describing coalescence and bridging begins with a relation between the temperature and the fraction solid in the domain of interest (Λ). Using an enthalpy balance;

$$\acute{H} = \rho c_p \frac{dT}{dt} - L\frac{df_s}{dt}, \tag{2.37}$$

with

$$f_s(t) = \frac{x^*(t)}{\Lambda/2} \tag{2.38}$$

where $x^*(t)$ is position of the interface, ρc_p is the volumetric specific heat and $\acute{H}$ is the volumetric heat extraction rate. The flux balance (Eq. (2.14)), is also used in order to calculate the normal velocity of the interface (v_n). Incorporating Eq. (2.36) into the Gibbs-Thomson condition for an alloy leads to

$$\begin{aligned}\Delta T &= T_L - T \\ &= \frac{\gamma_{gb} - 2\gamma_{sl}}{\Delta s_f}\frac{1}{\delta}\exp\left(-\frac{h}{\delta}\right) + \frac{v}{\mu_k} \\ &= \frac{\Delta\Gamma_b}{\delta}\exp\left(-\frac{h}{\delta}\right) + \frac{v_n}{\mu_k}\end{aligned} \tag{2.39}$$

where, for alloys, $T_L = T_m + m_l c_l$ is the liquidus temperature corresponding to the local liquidus concentration c_l at the interface and μ_k the mobility of the interface. Along with the usual definition of equilibrium at the interface, $c_s = kc_l$, a mean concentration in the solid, is introduced

$$\bar{c}_s(t) = \frac{1}{x^*(t)} \int_0^{x^*(t)} c_s(x,t)dx, \tag{2.40}$$

where $x^*(t)$ is position of the interface. Equations (2.37–2.39) represent the sharp interface description of the grain boundary at coalescence, where temperature and concentration now contain effects of repulsion and attraction near impingement.

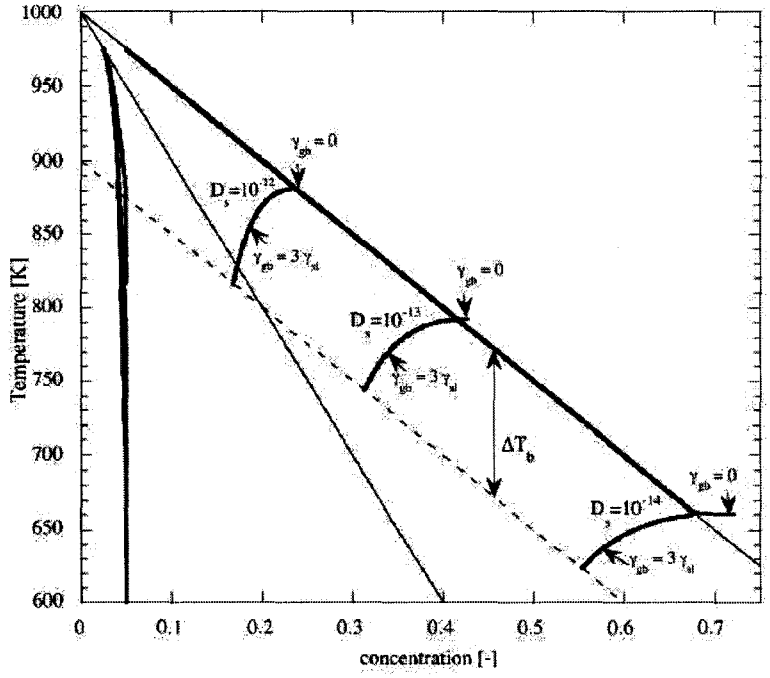

Figure 2.3: Effects of back diffusion on solidification and coalescence of binary alloy as predicted with the sharp interface model of Rappaz and co-workers. The black bold line to the far left represents the path taken by the concentration in the solid and the other follows the path in the liquid. Depicting a generic behavior, the results of solidification of attractive ($\gamma_{gb} = 0$) and repulsive boundaries ($\gamma_{gb} = 3\gamma_{sl}$) are shown. Adapted from [2].

Figure 2.3 summarizes the sharp interface results for coalescence behavior from the work of Rappaz and co-workers [2]. The figure shows the solidification path for three cases of back diffusion coefficients is similar, in the sense that the concentration of the liquid film follows the liquidus line perfectly, until the remaining last liquid

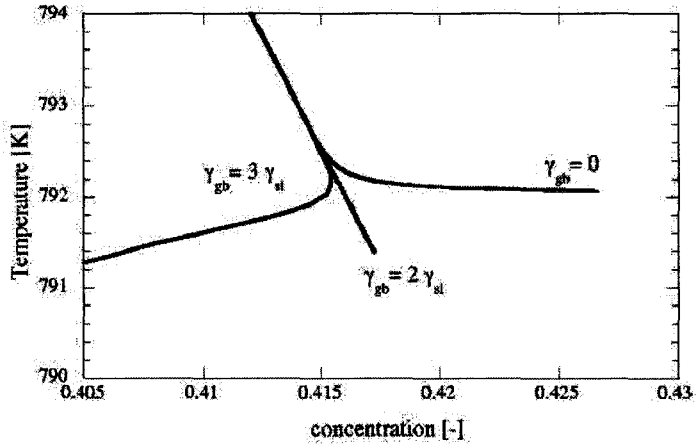

Figure 2.4: Effect of grain boundary energy in determining deviation from liquidus line predicted by sharp interface model [2].

film when a different amount of undercooling is required for the liquid film to diffuse away its impurity, allowing the interfaces to coalesce. This leads to a different path of the liquid film down the liquidus line, until the concentration decays toward the solidus, signaling coalescence. As the undercooling drops below the solidus the solid concentration start to approach the average concentration. Figure 2.4 shows for different grain boundary energies, a magnified view as the liquid concentration deviates in the last stages of solidification.

Chapter 3

Phase Field Method

3.1 Landau Theory

3.1.1 Ordering

Classically in thermodynamics, bulk variables are used to describe the state of material/system. These include, and are not limited to, temperature, composition, volume, presume, density, internal energy, entropy, and so on. These variables contribute to the free energy of the system , which then dictates the evolution of the system during a phase transformation. There are two major types of phase transformations, *first-order* and *second-order* transformations.

First-order transformations are characterized by a discontinuous first derivative of the Gibbs free energy with respect to temperature, $\partial G/\partial T$, at the critical transition temperature. Solidification from a melt and melting from a solid belong to this class of transformations. The discontinuity means there is also a discontinuous change in the enthalpy, H, corresponding to the evolution of latent heat [1].

Second-order transformations are identified by a continuous first derivative of the Gibbs free energy with respect to temperature, $\partial G/\partial T$, while having a discontinuous second derivative, $\partial^2 G/\partial T^2$, at the critical transition temperature. The consequence of a continuous first derivative is that the enthalpy, H, is also continuous. The

consequence of the discontinuity in the second derivative, however, leads to a change in the specific heat [1], i.e.

$$\left(\frac{\partial^2 G}{\partial T^2}\right)_P = -\left(\frac{S}{T}\right)_P = \frac{1}{T}\left(\frac{\partial H}{\partial T}\right)_P = \frac{C_P}{T}. \tag{3.1}$$

Phase transformations are often associated with a change of order in the emerging phases. As described by Porter and Easterling [1], to describe an ordered crystal being heated from low temperatures to above the disordering temperature, it is convenient to have a measure of the degree of order, in this case degree of crystallinity. To do so, they define a 'long-range' *order parameter* L, such that $L = 1$ is a fully ordered (crystalline) alloy where all atoms occupy their 'correct' sites and $L = 0$ is for a completely random distribution. If we consider this closely, we will realize that, a convention has been assumed for disordered and ordered phases, where tacitly the liquid assumes the basis of measure of disorder; this need not be the case however. Also upper and lower bounds have been given to the ordered and disordered phases respectively. This particular convention makes sense presently, since they define their order parameter based on mole fractions and probability of lattice occupation If we consider this closely, we will realize that, a convention has been assumed for disordered and ordered phases, where tacitly the liquid assumes the basis of measure of disorder; this need not be the case however. Also upper and lower bounds have been given to the ordered and disordered phases respectively. This particular convention makes sense presently, since they defined their order parameter based on mole fractions and probability of lattice occupation as

$$L = \frac{r_A - X_A}{1 - X_A}, \tag{3.2}$$

where X_A is the mole fraction of A in the alloy and r_A is the probability that a sublattice site is occupied by the 'right' kind of atom [1]. In another example of a crystal emerging from liquid, order parameters are the magnitudes of the fourier transform of the atomic density, corresponding to the principal reciprocal lattice vectors of the crystal. In both definitions of an order parameter, once a theory incorporating an order parameter(s) is developed, it can usually be re-scaled so that the order parameter varies between two convenient constants.

Keeping thermodynamics in mind, transitions from disorder to order can be seen as changes of symmetry as well. A parameter defining a bulk ordered phase can be differentiated from disordered phases by a non-zero average, $\langle\phi(\vec{x})\rangle$, of a local* order parameter field, $\phi(\vec{x})$. $\langle\phi(\vec{x})\rangle$ then displays the same symmetry as its corresponding phase [33]. At high temperature, above the critical temperature, by definition $\langle\phi(\vec{x})\rangle = 0$, which means complete disorder. Below the critical temperature, $\langle\phi(\vec{x})\rangle > 0$ and rises continuously from zero. In this case, the transition then is of second order with no latent heat evolution. If $\langle\phi(\vec{x})\rangle$ jumps discontinuously to a non-zero value below this critical temperature, then the transition is of first order and there is a latent heat evolution.

3.1.2 Landau Free Energy

This section works through the construction of a phenomenological free energy of a pure material, written in terms of the order parameter and temperature and with a first-order transition in mind we have,

*In this work, "local" means that the order can change on scales comparable to the interface width.

$$F[\phi, T] = \int_V f(\phi(\vec{x}, T))dV, \tag{3.3}$$

where V is the region held by the system and $f(\phi(\vec{x}, T))$ is the free energy density. Landau theory assumes that we can perform a Taylor expansion of the free energy density about $\phi = 0$ for temperatures in the proximity of the transition temperature[†],

$$f(\phi, T) = a_o(T) + a_1(T)\phi + \frac{1}{2}a_2(T)\phi^2 + \frac{1}{3}a_3(T)\phi^3 + \frac{1}{4}a_4(T)\phi^4 + \cdots, \tag{3.4}$$

where the phenomenological coefficients $a_o(T), a_1(T), a_2(T), a_3(T), a_4(T)$, etc. are yet unspecified functions of temperature. In principle, it is possible from microscopic models, to derive these coefficients. We aim to determine a link between these parameters to those of a material and its thermodynamics to ensure that our free energy possesses the correct behavior required for the phase transition described by the free energy density.

The coefficient $a_o(T)$ is the value of the free energy density, $f(\phi, T)$, in the disordered phase where T is far above the critical temperature T_c and described by $\phi = 0$. Dealing with a solidification transition we will denote $a_o(T)$ as $f_l(T)$.

Equilibrium order parameters, ϕ_s and ϕ_l, are characterized by the minima in the free energy,

$$\frac{\partial f(\phi, T)}{\partial \phi} = 0 \tag{3.5}$$

[†]Strictly speaking, Landau theory works for second order transformations near the critical point where such a Taylor expansion would properly capture the true form of the free energy, whose minimum change continuously from the single minima at the critical point. For first order transitions, the change of free energy below the melting temperature is abrupt and a fourth order Taylor expansion is not strictly correct. In this case the analysis presented here is qualitative.

and in knowing the disordered state is described by $\phi = 0$ implies that $\phi_l = 0$ and $a_1(T) = 0$. Retaining up to the ϕ^4-term, the free energy density we will be working with is given by

$$f(\phi, T) = f_l(T) + \frac{1}{2}a_2(T)\phi^2 + \frac{1}{3}a_3(T)\phi^3 + \frac{1}{4}a_4(T)\phi^4. \tag{3.6}$$

The condition $\partial f(\phi, T)/\partial\phi = 0$ gives us the following cubic equation

$$a_2\phi + a_3\phi^2 + a_4\phi^3 = 0, \tag{3.7}$$

the solutions of which are

$$\phi_l \equiv \phi = 0, \tag{3.8}$$

and is the equilibrium value for the disordered/liquid state. The other solution for the solid is

$$\phi_s \equiv \phi = \frac{-a_3 \pm \sqrt{a_3^2 - 4a_2a_4}}{2a_4}. \tag{3.9}$$

If we consider the solution of Eq. (3.7), we notice that the non-zero(Eq. (3.9)) solution requires some attention. At high temperatures far above that of the critical temperature, the non-zero solution is complex and the only allowed physical solution is Eq. (3.8). As temperature is decreased and approaches a new temperature from above, T_r, the solution to Eq. (3.9) becomes real at T_r such that

$$a_2(T_r) = \frac{a_3(T_r)^2}{4a_4(T_r)} \tag{3.10}$$

This however does not guarantee that either of the non-zero solutions to Eq. (3.9) represents a stable equilibrium state at $T < T_r$. At a temperature $T = T_m$, where $T_c < T_m < T_r$, according to thermodynamics, the free energies of solid and liquid are equal. This means that at this temperature, the two minima of $\phi = 0$ and $\phi \neq 0$, are equally deep. Mathematically

$$f(\phi_s, T_m) = f(\phi_l, T_m), \tag{3.11}$$

where ϕ_l and ϕ_s satisfy

$$\left.\frac{\partial f(\phi, T_m)}{\partial \phi}\right|_{\phi=\phi_s,\phi_l=0} = 0 \tag{3.12}$$

Rearranging and setting $T_r = T_m$ in Eq. (3.10), substituting into Eq. (3.9) and solving, we obtain the following equilibrium variables at T_m

$$\phi_l = 0 \tag{3.13}$$

$$\phi_s = \sqrt{-\frac{a_2(T_m)}{a_4(T_m)}} \tag{3.14}$$

Rescaling through $\phi = |\phi|/\phi_s$, we can thus re-write the free energy at the melting temperature as

$$f(\phi, T_m) = f_l(T_m) + H(T_m)\phi^2(1-\phi)^2, \tag{3.15}$$

where the combination

$$H(T_m) = \frac{a_2(T_m)^2}{a_4(T_m)}, \tag{3.16}$$

turns out to be related to the nucleation barrier for solidification.

We next expand Eq. (3.6) near $T = T_m$, and with the help of Eq. (3.15) obtain

$$\begin{aligned} f(\phi,T) &= f(\phi,T_m) + \frac{\partial f(\phi,T)}{\partial T} \\ &= f_l(T_m) + H(T_m)\phi^2(1-\phi)^2 + \left.\frac{\partial f_l(T)}{\partial T}\right|_{T_m}(T-T_m) \\ &+ \left(\left.\frac{\partial a_2(T)}{\partial T}\right|_{T_m}\phi^2 + \left.\frac{\partial a_3(T)}{\partial T}\right|_{T_m}\phi^3 + \left.\frac{\partial a_4(T)}{\partial T}\right|_{T_m}\phi^4\right)(T-T_m) \end{aligned} \quad (3.17)$$

The cubic term is the lowest order term capable of characterizing a first-order transition at T_m[‡]. It tilts the wells changing the depths of the energies of the minima, thus allowing for the discontinuous jump in ϕ, as T_m is approached. We simplify further by neglecting temperature dependence of the coefficients $a_2(T)$ and $a_4(T)$[§], giving

$$\begin{aligned} f(\phi,T) &= f_l(T_m) + H(T_m)\phi^2(1-\phi)^2 \\ &+ \left(\left.\frac{\partial f_l(T)}{\partial T}\right|_{T_m} + \left.\frac{\partial a_3(T)}{\partial T}\right|_{T_m}\phi^3\right)(T-T_m) \end{aligned} \quad (3.18)$$

From thermodynamics, we have $\partial f/\partial T = -S$, therefore at the melting temperature we make new definitions,

[‡]We can also use a linear term in ϕ, however this will lead to a free energy for which the minima in ϕ depend on temperature. It is simpler to calibrate the free energy via the cubic term, which makes ϕ_s independent of temperature, effectively transferring the temperature dependence to other variables.

[§]It should be noted that the temperature dependence of $a_2(T)$ cannot be ignored for second-order transitions.

$$\left.\frac{\partial f_l(T)}{\partial T}\right|_{T_m} + \left.\frac{\partial a_3(T)}{\partial T}\right|_{T_m} \phi^3 = -s_l + \left.\frac{\partial a_3(T)}{\partial T}\right|_{T_m} \phi^3 = -S(\phi, T_m) \tag{3.19}$$

and

$$\left.\frac{\partial a_3(T)}{\partial T}\right|_{T_m} = \frac{L}{T_m}, \tag{3.20}$$

giving us

$$f(\phi, T) = f_l(T_m) + H(T_m)\phi^2(1-\phi)^2 - S(\phi, T_m)(T - T_m) \tag{3.21}$$

If one were to solve this equation for ϕ_s, it is easily seen that it is only at $T = T_m$ that $\phi_s = 1$. At other temperatures ϕ_s is a function of temperature. To simplify the problem, it is simplest to redefine the entropy function from the cubic form in Eq. (3.19) to a form that enforces $\phi_s = 1$ for all values of T, thereby keeping the order parameter in the range $0 \leq \phi \leq 1$. We choose then

$$S(\phi, T_m) = s_l - \frac{L_f}{T_m} p(\phi), \tag{3.22}$$

where $p(\phi)$ is a phenomenological interpolation function odd in ϕ, satisfying the properties $p(0) = 0$, $p(1) = 1$ and $p'(\phi)|_{\phi=0,1} = 0$. Examples of commonly used functions are $p(\phi) = \phi^2(3-2\phi)$ and $p(\phi) = \phi^3(10-15\phi+6\phi^2)$. Substituting Eq. (3.22) into Eq. (3.21) we obtain the "double well" free energy density for a pure material

$$f(\phi, T) = g(T) + H(T_m)\phi^2(1-\phi)^2 - \frac{L_f(T - T_m)}{T_m} p(\phi). \tag{3.23}$$

Since $g(T) = f_l(T_m) - s_l(T - T_m)$ is equal in both phases it can be subtracted out at a fixed temperature. Figure 3.1 displays graphically the double well nature of this free energy with respect to the order parameter ϕ.

The choice of interpolation function $p(\phi)$ does not affect the bulk thermodynamics described by the free energy at all. It only affects the transition through the interface. This behavior through the interface can also be calibrated by choosing the other parameters collectively such as to model a specified surface tension. This will be discussed below.

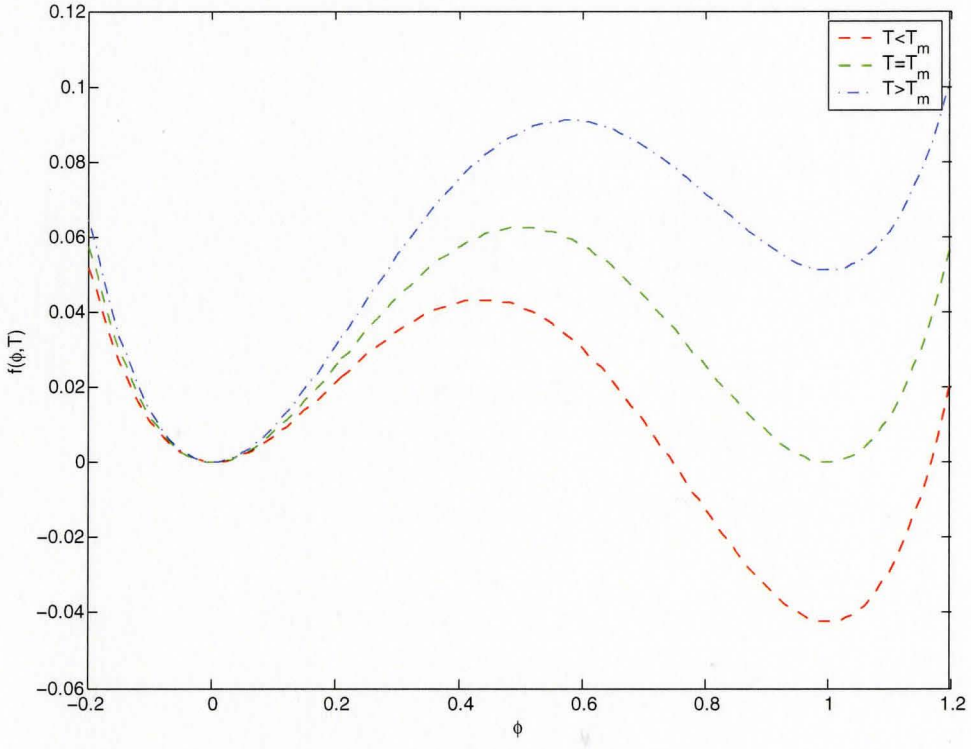

Figure 3.1: Schematic representation of the "double well" free energy.

3.1.3 Spatial Variations

In this phase field formalism, phase transitions occur via changes of the phase field or order parameter across a diffuse boundary representing the phase boundary. These contribute to the surface energy of the system.

Interfacial energy enters the Landau free energy via gradients in the order parameter. With this in mind an energy functional that incorporates surface energy can take the following form

$$F[\phi, T] = \int_V \left[\frac{\epsilon_\phi^2 |\nabla \phi|^2}{2} + f(\phi, T) \right] dV, \tag{3.24}$$

where ϵ_ϕ is the so called gradient energy coefficient, scales the width of the diffuse interface and scales the mobility of the interface, having units of $\sqrt{J/m}$, and $f(\phi, T)$ is the double well free energy density of Eq. (3.23). The one dimensional general shape of the order parameter and the total free energy density in Eq. (3.24) are plotted for an arbitrary choice of parameters in Fig. 3.2.

From Fig. 3.2 we can clearly see that far away from the interface, in the bulk of the system, the order parameter is constant. This is the reason why $\nabla \phi = 0$ in those regions, therefore there is no contribution to the surface energy of the system. However in the locality of the interface, the hump in Fig. 3.2, depicts how the free energy density is varying. Since the free energy functional is an integral over all space (one dimensional in this illustrative example), the integration in this region will allow us to attain the total value of the surface energy.

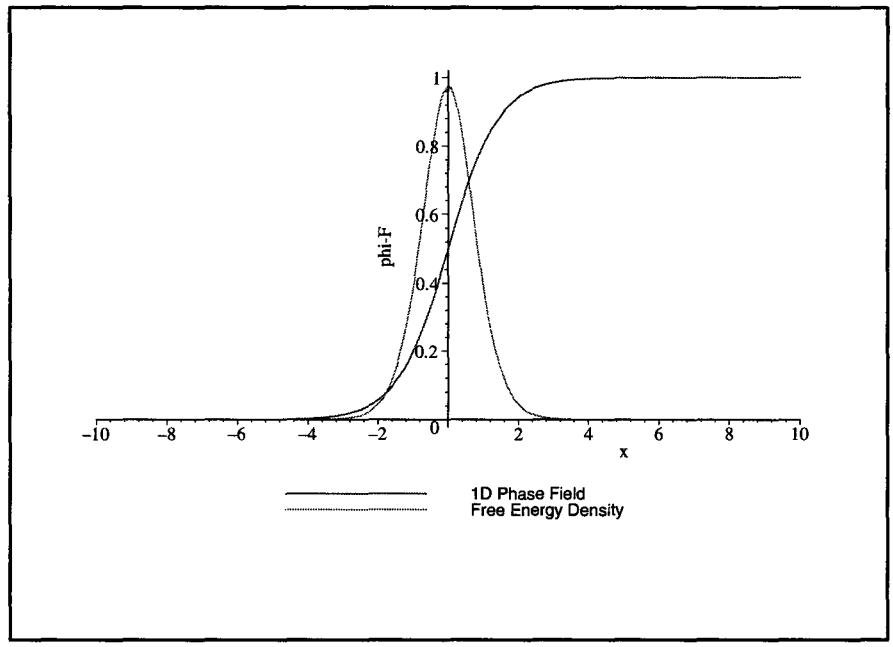

Figure 3.2: Schematic of the varying order parameter and the gradient energy associated with it in the vicinity of the interface.

3.2 Dynamics

In general the dynamics of the phase field proceed by minimizing the free energy functional discussed above. The phase field being a non-conserved field[¶], minimization of said function follows from the Allen-Cahn/Ginzburgh-Landau equation with an added term representing thermal fluctuations. The dynamic equation for a pure material then takes the form

$$\frac{\partial \phi}{\partial t} = -\Gamma_{\phi} \frac{\delta F[\phi, T]}{\delta \phi} + \eta(\vec{x}, t), \tag{3.25}$$

[¶]This simply means that the system can go from a complete state of disorder to one of complete order, i.e. a glass of water can go form being all liquid to all solid. A conserved order parameter must change such that its global average remains fixed. An example is concentration of impurities in alloys.

where Γ_ϕ is the mobility of the interface or can be written as the inverse of the characteristic kinetic time coefficient for atomic attachment, τ. $\frac{\delta F[\phi,T]}{\delta\phi}$ is a functional/variational derivative, which determines how the free energy density varies with the changes in the function ϕ. In general, application of a functional derivative yields the so-called Euler-Lagrange equation of the form,

$$\frac{\delta f(\chi, \nabla\chi)}{\delta\chi} = \frac{\partial f}{\partial\chi} - \nabla\frac{\partial f}{\partial\nabla\chi}, \tag{3.26}$$

allowing us to write Eq. (3.25) simply as

$$\begin{aligned}\frac{\partial\phi}{\partial t} &= -\Gamma_\phi\frac{\delta F[\phi,T]}{\delta\phi} + \eta(\vec{x},t) \\ &= -\Gamma_\phi\left(\frac{\partial f}{\partial\phi} - \epsilon_\phi^2\nabla^2\phi\right) + \eta(\vec{x},t),\end{aligned} \tag{3.27}$$

The interested reader should consult Ref. [33] for more details concerning the rules of functional differentiation. The last term in Eq. (3.25), $\eta(\vec{x},t)$, is a stochastic variable representing noise caused by thermal fluctuations. The motion of atoms below the scale on which ϕ is coarse grained defines this noise and describes the fluctuations. These fluctuations that occur at the interface, follow well defined statistics and obeys the well known fluctuation-dissipation theorem [33].

The conserved parameter in this problem is heat, which is characterized by temperature and described by a coupled diffusion of heat equation based on an enthalpy balance.

$$\rho c_p\frac{\partial T}{\partial t} = -\nabla\cdot\vec{J}_q + \rho L_f\frac{\partial\phi}{\partial t} - \vec{\nabla}\cdot\vec{\zeta}(\vec{x},t), \tag{3.28}$$

which is a conservation of flux equation in the absence of latent heat, $\vec{J}_q = -k_{cond}\vec{\nabla}T$ is the flux, the second term accounts for the release of latent heat at the interface as

it advances and the last term is the conserved stochastic noise variable which has the same statistical properties as the one in Eq. (3.26).

3.3 Anisotropy

To simulate dendritic structures we need to include a form of anisotropy in the phase field equations. Anisotropy enters into the model through the surface energy gradient term and mobility via an angular dependence, since classically it enters through the capillary length and kinetic coefficient term. It takes the form of $|\epsilon(\psi)\nabla\phi|^2/2$ and the mobility $\Gamma_\phi(\psi)$, where assuming the standard form, we have $\epsilon_\phi(\psi) = \epsilon_o(1+\epsilon_4\cos(m\psi))$, with ψ being the normal angle between the interface and x axis defined as $\psi = \arctan(\partial_y\phi/\partial_x\phi)$. The parameter m is the symmetry desired for the crystal ($m = 4$ for fourfold symmetry ...), ϵ_o is the isotropic value of the gradient coefficient and ϵ_4 is the anisotropic strength which can be experimentally determined [34; 35; 36; 37; 38; 39; 40; 41], at least in principle. Practically, it is very difficult. The parameter $\Gamma_\phi(\psi)$ can, but does not necessarily have to have the same form as gradient energy coefficient. After application of the variational derivative, the simple gradient term, in Eq. (3.27), is replaced by a set of terms which now describe the effect of anisotropy. Thus the previous $\epsilon_\phi^2\nabla^2\phi$ now becomes

$$\vec{\nabla}\cdot[\epsilon_\phi^2(\psi)\vec{\nabla}\phi] - \partial_x\left(\epsilon_\phi(\psi)\frac{\partial\epsilon_\phi}{\partial\psi}\frac{\partial\phi}{\partial y}\right) + \partial_y\left(\epsilon_\phi(\psi)\frac{\partial\epsilon_\phi}{\partial\psi}\frac{\partial\phi}{\partial x}\right) \tag{3.29}$$

With the inclusion of the above terms, dendritic solidification, with primary arms are possible and the inclusion of stochastic noise terms allows one to also simulate secondary arms as well.

3.4 Making Contact With Sharp Interface Kinetics

To use the phase field method as a representative case for equilibrium sharp interface models (often referred to as making them "quantitative"), a direct comparison needs to be made between these models. It is widely accepted that the phase field equations only represent the microscopic physics described by Eqs. (2.9–2.11) for the pure material and Eqs.(2.13–2.15) in the case of an alloy in the limit where the interface width becomes nano-scopic. However, it has recently become possible to emulate the sharp interface model with diffuse interfaces as well. This limit is usually addressed via asymptotic boundary layer analysis.

Asymptotic analysis works by considering a perturbation of the corresponding fields (e.g. temperature, phase, concentration) in two regions. The first region is the *inner* region (diffuse interface or microscopic region), where solutions scale with the length, $\varsigma = x/W_o$, where W_o is the interface width. The second region, the *outer* region (bulk phases or macroscopic region), is where solutions scale with the diffusion length $l = x/(D/v_n)$. One desires to then match the solutions of the inner solutions as $\varsigma \rightarrow \infty$, to the outer solutions as $l \rightarrow 0$. In so doing the phase field parameters are calibrated so that the outer solutions satisfy the appropriate boundary conditions when projected into a hypothetical sharp interface lying in the diffuse interface region. Matched asymptotic boundary layer analysis is well beyond the scope of this thesis. Only the results of such analyses on the phase field models –and their references– will be presented here.

3.5 Quantitative Phase Field Models of Solidification

3.5.1 Pure Material

The appeal of asymptotic analysis was, in a sense, rediscovered in the work of Karma and Rappel [42; 43; 44] for a pure material. In their work,the order parameter $\phi(\vec{x},t)$, is scaled onto $\phi = -1$ and $\phi = 1$, to represent liquid and solid respectively. The solid-liquid interface is defined by the surface defined by the point $\phi(x,y) = 0$. Their free energy functional is defined to be

$$F[\phi,u] = \int_V dV \left[W_o^2|\nabla\phi|^2 + f(\phi) + \lambda u g(\phi)\right], \tag{3.30}$$

where for convenience the temperature in the model is expressed in terms of the dimensionless temperature field $u \equiv (T - T_m)/(L/c_p)$, L is the latent heat, c_p the specific heat and λ is a constant being proportional to the inverse of the nucleation energy. It is straightforward but tedious to show that the free energy functional in Eq. (3.23) and Eq. (3.24) can be expressed as that in Eq. (3.30).

If we ignore the actual process of nucleation and consider kinetics alone, the parameter λ, can be considered a free parameter which can be treated as a numerical convergence parameter that can be tuned to accelerate the model's simulation speed, *without* affecting its ability to emulate the correct sharp interface model. The function $f(\phi) = -\frac{1}{2}\phi^2 + \frac{1}{4}\phi^4$ is the double well potential. $g(\phi)$ is an interpolating function, increasing monotonously and assuming limiting values of $g(\pm 1) = \pm 1$ and $g'(\pm 1) = 0$. A convenient form maintaining the bulk values is $g(\phi) = 15(\phi - 2\phi^3/3 + \phi^5/5)/8$. The gradient energy coefficient, W_o, scales the surface energy, and the work of Karma and Rappel [42; 43; 44] made the surface energy anisotropic by making $W(\hat{n}) = W_o a(\hat{n})$

where $\hat{n}$ is the local normal to the interface and W_o is the isotropic width for the solid-liquid interface. The form used was

$$a(\hat{n}) = (1 - 3\epsilon_4)\left(1 + \frac{4\epsilon_4}{1 - 3\epsilon_4}(n_x^4 + n_y^4 + n_z^4)\right) \tag{3.31}$$

where ϵ_4 is the fourfold anisotropy strength.

The dynamics of the phase field (ϕ), follows from Eq. (3.27), and ignoring any additive noise terms is

$$\tau_o \frac{\partial \phi}{\partial t} = W_o^2 \nabla^2 \phi + \phi - \phi^3 - \lambda u (1 - \phi^2)^2, \tag{3.32}$$

where, in the notation of the model in Eq. (3.23) $\tau_o = 1/(\Gamma H)$. The characteristic time constant for atomic attachment τ_o, can be made anisotropic through $\tau(\hat{n}) = \tau_o b(\hat{n})$, with τ_o being the constant for the isotropic case. For most casting situations, Eq. (2.11) should be simulated for the case of $\beta = 0$. This implies that the interface can be assumed to be in local equilibrium. It will be shown below that simulating the limit of $\beta = 0$ of the sharp interface model, Eq. (2.11), only becomes possible when $b(\hat{n}) = a(\hat{n})$ in the above phase field model. Finally, Eq. (3.32) is coupled to dynamics of the u field through a modified heat equation

$$\frac{\partial u}{\partial t} = D\nabla^2 u - \frac{1}{2}\frac{\partial \phi}{\partial t}, \tag{3.33}$$

which is the same as Eq. (3.28), where D is the thermal diffusion coefficient and the second term represents the release of latent heat. The dynamic equations, Eqs. (3.32) and (3.33), can be made simpler if conveniently considered in dimensionless form by rescaling space as $x \rightarrow x/W_o$ and time as $t \rightarrow t/\tau_o$. Then in Eq. (3.32) we can treat $\tau_o = W_o = 1$ while in Eq. (3.33) we treat $\bar{D}$ or $D \rightarrow D\tau_o/W_o^2$.

As stated above, the sharp interface can be recovered by selection of the appropriate parameters of the phase field model. Classically (the classical period here, not to be confused with that of ancient Greek history, implies 1980's.), this was achieved by letting $W_o \rightarrow 0$ and $\lambda \rightarrow 0$, such that the capillary length $d_o \propto W_o/\lambda$ and $\beta \propto \tau_o/\lambda W_o$ [45; 35]. For the case of negligible interface kinetics, $\beta = 0$, use of these limits would require τ_o to be excessively small. And the interface width being order of $10^{-9}m$, this would prevent simulation of large scale dendritic simulations over a reasonable time period.

The work of Karma and Rappel [42; 43] improved the mapping of the phase field model of Eqs. (3.32) and (3.33) to the sharp interface model, through a matched asymptotic analysis to second order (i.e. "thin interface limit"), for equal thermal conductivities in both liquid and solid. Their work showed that the following inter-relations would guarantee the recovery of the sharp interface model by the phase field model of Eqs. (3.32) and (3.33);

$$d_o = a_1 \frac{W_o}{\lambda} \tag{3.34}$$

and

$$\beta = \frac{a_1 \tau_o}{\lambda W_o}\left[1 - a_2 \frac{\lambda W_o^2}{D\tau_o}\right] \tag{3.35}$$

where $a_1 = 0.8839$ and $a_2 = 0.6267$ are constants that depend on the choice of functions for the double well and interpolation[‖]. The most noteworthy characteristic of Eq. (3.35) is that it permits the simulation of the case when $\beta = 0$ for relatively large ratios of W_o/d_o, merely by appropriate choice of the kinetic time constant τ_o.

[‖]The work of Karma and Rappel [43] and Kim and co-workers [37] show how these constants can be tailored to different choices of interpolation functions.

However, one will note that unique choice of the time constant is only possible when $b(\hat{n}) = a(\hat{n})$. If not, we would have dependence of these terms on the anisotropic nature of the constants. A matched asymptotic analysis [39], that treated a general free energy density $f(c, T, \phi)$ for pure materials and alloys –with equal diffusivity– was later reported, where the asymptotic relations had similar forms to Eqs. (3.34) and (3.35).

3.5.2 Binary Alloy solidification

A general phase field model for dilute binary alloy solidification has been developed in the work of Ref. [46]. A phase field model for isothermal binary alloy solidification of this type starts with the following functional

$$F[\phi, c, T] = \int_V dV \left[\frac{\epsilon_\phi^2}{2} |\nabla \phi|^2 + \frac{\epsilon_c^2}{2} |\nabla c|^2 + f(\phi, c, T) \right], \tag{3.36}$$

with $f(\phi, c, T) = f_s(c, T)p(\phi) + f_l(c, T)[1 - p(\phi)] + H f_{\mathrm{D}}(\phi)$, where $p(\phi)$ interpolates between 0 and 1 in the liquid and solid states, respectively. The function $f_l(c, T)$ and $f_s(c, T)$ are, respectively, the thermodynamic free energies for a liquid and solid. The function $f_D(\phi)$ is the same double well and H the nucleation barrier used in the pure materials. In the limit of a dilute ideal alloy the free energy is given by

$$f_\nu = c f_B(T) + (1 - c) f_A(T) + \frac{RT}{v_o} (c \ln c + (1 - c) \ln(1 - c)), \tag{3.37}$$

where $\nu = s, l$ and bulk free energies (f_A and f_B) can be taken from Calphad type thermodynamic databases. This form of the free energy density, Eq. (3.37), can easily be extended to regular and subregular solution models.

The alloy phase field model has the following equations of motion, neglecting corresponding noise terms;

$$\frac{\partial \phi}{\partial t} = -\Gamma_\phi \frac{\delta F}{\delta \phi}, \tag{3.38}$$

$$\frac{\partial c}{\partial t} = \vec{\nabla} \cdot \left[\Gamma_c(\phi, c) \vec{\nabla} \frac{\delta F}{\delta c} \right], \tag{3.39}$$

where the mobility of the concentration field is related to the diffusion coefficient, concentration and phase field and is defined as

$$\Gamma_c(\phi, c) = \frac{v_o}{RT} c(1-c)[D_s p(\phi) + D_l(1-p(\phi))]. \tag{3.40}$$

Equation (3.39) can be written as a mass conservation equation,

$$\frac{\partial c}{\partial t} + \vec{\nabla} \cdot \vec{J}_c = 0 \tag{3.41}$$

where $\vec{J}_c = -\Gamma_c \vec{\nabla} \mu$ is the flux density, where the chemical potential $\mu \equiv \delta F / \delta c$.

3.5.2.1 Interface effects - part I

The alloy phase field model in the previous section, like the model of a pure materials, can be shown to map onto the sharp interface equations discussed above (Eqs. (2.13–2.15)) when the interface width W_o becomes nano-scopic in size. As discussed previously in the context of a pure model, numerically simulating a phase field model with a physical interface width $W_o \sim 10^{-9} - 10^{-8}$m is unfeasible. The only way to conduct practical simulations is to stretch the interface artificially. This allows simulation times to be greatly reduced, particularly at low solidification rates

relevant to continuous casting. Unfortunately, artificially stretching the interface also enhances solute trapping and other non-equilibrium effects in the model. While these effects are all physical, they are only expected to show up at rapid cooling rates, not at low cooling rates. In effect, by thickening the interface for numerical convenience –at low cooling rates– we also force the model to deviate from the expected sharp interface kinetics/model discussed previously.

The precise nature of the non-equilibrium effects induced by the presence of a finite interface are; (a) chemical potential jump at the interface and a modification of the mass conservation at the interface due to (b) stretching of the interface because curvature is different on one side vs. the other when the interface is non-zero and (c) diffusion tangentially through the interface. As mentioned above, these are all physical but only relevant at rapid cooling rates when the solute (or thermal) diffusion length becomes comparable to the interface width.

This dilemma of using prohibitively small interfaces to avoid spurious kinetics due to thin (or "diffuse") interfaces plagued all phase field models until about 7 years ago when Karma and co-workers found a mathematical remedy to these problems, at least for the case of dilute binary alloys (done about 12 years ago for pure materials). The work of Karma [47] showed that all three kinetic effects described in the previous paragraph can be made to vanish simultaneously while still allowing one to exploit the benefits of a diffuse interface. A more rigorous derivation and matched asymptotic analysis followed which included an extension to include directional solidification [41]. For the particular case of ideal dilute binary alloy with two sided diffusion, a method for nullifying the spurious effects at the interface forgoes the usual variational formalism used in deriving the evolution equations for the phase field and concentration (i.e. abandoning the approach that lead to Eqs. (3.38) and (3.39)). Instead, the following changes to the classical phase field methodology are

made: (i)change the interpolation function for the chemical potential from the original one inherited from the energy functional; (ii)the introduction of a phenomenological flux, so-called the *anti-trapping* flux to the concentration equation and (iii) choose the specific interpolation function governing diffusion through the interface so that along with changes (i) and (ii) the artificial kinetic corrections mentioned above can be eliminated. Combined, the above three mentioned corrections gave the necessary degrees of freedom to allow complete elimination of the spurious effects. The modified version of Eqs. (3.38)–(3.39) satisfying all these considerations are:

$$\begin{aligned}\tau\frac{\partial\phi}{\partial t} =&\vec{\nabla}\cdot[W(\hat{n})^2\vec{\nabla}\phi]+\phi-\phi^3-\frac{\lambda}{1-k}(e^u-1)(1-\phi^2)^2\\ &+\partial_x\left(W(\hat{n})|\vec{\nabla}\phi|^2\frac{\partial W(\hat{n})}{\partial(\partial_x\phi)}\right)\\ &+\partial_y\left(W(\hat{n})|\vec{\nabla}\phi|^2\frac{\partial W(\hat{n})}{\partial(\partial_y\phi)}\right),\end{aligned} \tag{3.42}$$

and

$$\begin{aligned}\frac{\partial c}{\partial t} =&-\vec{\nabla}\cdot\vec{J}\\ =&\vec{\nabla}\cdot\left(Dcq(\phi)\vec{\nabla}u+a_tW_oc_l^0e^u\frac{\partial\phi}{\partial t}\frac{\vec{\nabla}\phi}{|\vec{\nabla}\phi|}\right),\end{aligned} \tag{3.43}$$

where $u=\ln(2c/c_l^0)/[1+k-(1-k)h(\phi)]$ is a dimensionless relative chemical potential. The second term in the concentration equation is the anti-trapping flux term. The parameter $a_t=1/2\sqrt{2}$ is the anti-trapping coefficient, which is generally dependent on the choice of interpolation functions. The function $q(\phi)$ is the interpolation function for diffusion of solute and has the form

$$q(\phi)=\frac{1-\phi}{(1+k-(1-k)h(\phi)}+\frac{\xi(1+\phi)}{2} \tag{3.44}$$

where for two sided diffusion $\xi = D_s/D_l$ and $\xi = 0$ otherwise, and has the same limits as $h(\phi)$ at $\phi = \pm 1$ and k is the partition coefficient. These interpolation functions $q(\phi)$ and $h(\phi)$, along with the anti-trapping coefficient a_t, are the degrees of freedom that allows one to eliminate the interface effects and emulate the sharp interface limit using a diffuse interface. Kim and co-workers also introduced a diffuse interface formulation for binary alloys phase field model [48]. However, the non-equilibrium effects cause by the artificially diffuse interface are not entirely eliminated by this approach and is less accurate than the approach of Karma and co-workers.

3.5.2.2 Interface effects - part II

An additional difficulty arising in phase field models –or any fundamental model that considers interface variations– is that an interface of finite thickness renders surface energy dependent on the concentration distribution across the interface. More specifically, when one calculates the equilibrium solution profiles, i.e. $\delta F/\delta\phi = 0$ and $\delta F/\delta c = const$, the solutions are coupled one to the other, and there is a concentration contribution to the Gibbs-Thomson condition. While physical, this makes calculation of the surface energy quite challenging. This limitation for general phase field models for alloys (discussed in Section 3.5.2),was first addressed by Kim and co-workers [48], where the introduction of separate concentration fields associated with each phase was shown to guarantee the decoupling of the fields in equilibrium. This decoupling makes it possible to express the surface energy of the phase field model as a constant (in terms of model parameters), which can be manually changed at any position and time to take on any dependence on concentration and temperature (e.g. such as that determined experimentally).

The method of Kim and co-workers defined the interfacial region as having two different concentration fields running through it, but a constant chemical potential. There were two additional equations that required solving within this formalism.The first was that physical concentration was expressed as

$$c = c_s p(\phi) + c_l(1 - p(\phi)), \tag{3.45}$$

and the constancy of the chemical potential had to be enforced via

$$\frac{\partial f_s(c_s, T)}{\partial c} = \frac{\partial f_l(c_l, T)}{\partial c} \tag{3.46}$$

Though in this formalism, the introduction of separate concentration fields allowed the calculation of the correct surface energy –even for a arbitrary binary alloy free energies– the kinetic effects described in Section 3.5.2.1 remained.

In the formalism of Karma and co-workers (described in Section 3.5.2.1), decoupling the phase and concentration profiles at steady state happens automatically by the specific choice of interpolation functions. As a result, in addition to their model emulating the correct sharp interface model, it can also be made to accept any surface energy parametrization at any location at the interface. Unfortunately, their formulation was only worked out for ideal, dilute alloys.

3.5.2.3 Extension of the anti-trapping formalism to non-ideal alloys

An extension to the work of Karma and co-workers has recently been reported by Tong *et al.* [49], to address solidification in binary alloys with nonlinear liquidus and solidus phase boundaries, i.e. for non-ideal alloys. In this work, a paradigm is laid out, whereby one can approximate the Gibbs free energy of a general alloy phase

diagram by the free energy function of that given by an ideal dilute alloy, modified, however, with effective temperature dependent coefficients. The equations of motion then become,

$$\begin{aligned}\tau_o(T)a_s(\hat{n})^2\frac{\partial\phi}{\partial t} =&\vec{\nabla}\cdot[W_o(T)^2a_s(\hat{n})^2\vec{\nabla}\phi] + \phi - \phi^3 \\ &-\frac{\lambda(T)}{1-k(T)}(e^u-1)(1-\phi^2)^2 \\ &+\vec{\nabla}\cdot\left(W_o(T)a_s(\hat{n})|\vec{\nabla}\phi|^2\frac{\partial a_s(\hat{n})}{\partial(\vec{\nabla}\phi)}\right)\end{aligned} \tag{3.47}$$

$$\frac{\partial c}{\partial t} = \vec{\nabla}\cdot\left(D(T)cq(\phi)\vec{\nabla}u + a_tW_o(T)c_l^0e^u\frac{\partial\phi}{\partial t}\frac{\vec{\nabla}\phi}{|\vec{\nabla}\phi|}\right). \tag{3.48}$$

Aside from the temperature dependent parameters, Eqs. (3.47) and (3.48), have the same *form* as Eqs. (3.42) and (3.43). This allows the use of the thin interface parameter relationships previously developed by Karma and co-workers to maintain the interface in local equilibrium while exploiting the benefits of a diffuse interface.

3.6 Multi-Component and Multi-Phase Field Models

Extensions to the phase field paradigm has also been developed to include the effect of multiple alloy components and phases [50; 51; 52; 53; 54; 55; 56; 57; 58]. To date most such models are plagued by the inability to performs efficient large scale simulations on experimentally relevant length scales and process parameters and are plagued by the thin-interface problems discussed above. They are therefore not reliable for quantitative simulation of solidification. One notable exception is the work of Kim [57], which in a recent approach, his equations of motion include an anti-trapping flux in the diffusion equation for each species of a multi-component, single

phase alloy. Another exception to the general rule of the first sentence is the work of Folch and Plapp [59]. They have used a multiple phase field model to simulate eutectic solidification in binary alloys. They too designed a new three-phase free energy and dynamical equations that exploit the results of Karma and co-workers to be able to examine eutectic and peritectic solidification. These works, however, will not be reviewed further here.

3.7 Polycrystalline Phase Field models

The aim of this thesis is to extend the work of Karma and co-workers and Tong and co-workers to single-phase solidification of polycrystal alloys. It is instructive, therefore, to review the two most widely used formulations that have previously been used to address the issue of polycrystalline solidification. This thesis will marry the first of these approaches with the approach of Karma and co-workers to develop a new model of polycrystalline solidification which incorporates quantitative dendritic growth kinetics with qualitatively correct grain boundary coalescence.

3.7.1 Multi-Order Parameter Phase Field Models

To describe multiple grains of a single phase (or also multiple phases), one can write a free energy functional that couples multiple order parameters. A basic model using multiple order parameters that considers grain growth for a pure material has the following energy functional [60; 61];

$$F = \int dV \left[\sum_{i=1}^{N} \frac{\epsilon_{\phi_i}^2}{2} |\vec{\nabla}\phi_i|^2 + \sum_{i=1}^{N} \left(-\frac{1}{2}\phi_i^2 + \frac{1}{4}\phi_i^4 \right) + \alpha_{obs} \sum_{i=1}^{N} \sum_{j \neq i}^{N} \phi_i^2 \phi_j^2 \right], \qquad (3.49)$$

where the first term gives rise to gradient energy and therefore grain boundary energy of grains. The second term represents a multi-well potential having $2N$ minima, allowing one to theoretically consider a large number of crystals for single phase systems (or several phases as was briefly alluded to in the last section). In this case the multi-well is chosen so its minima are at $\phi_i = \pm 1$, but another form could be chosen where the minima lie in $\phi_i = 0, 1$. The last term containing α_{obs}, is called the *double obstacle potential*. This potential is just an interaction energy that penalizes those fields that overlap more than is dictated by the potential height barrier α_{obs}. This free energy functional, for the case of $N = 2$ and neglecting the gradient term is depicted in Figure 3.3.

The kinetics of each order parameter ϕ_i is described by

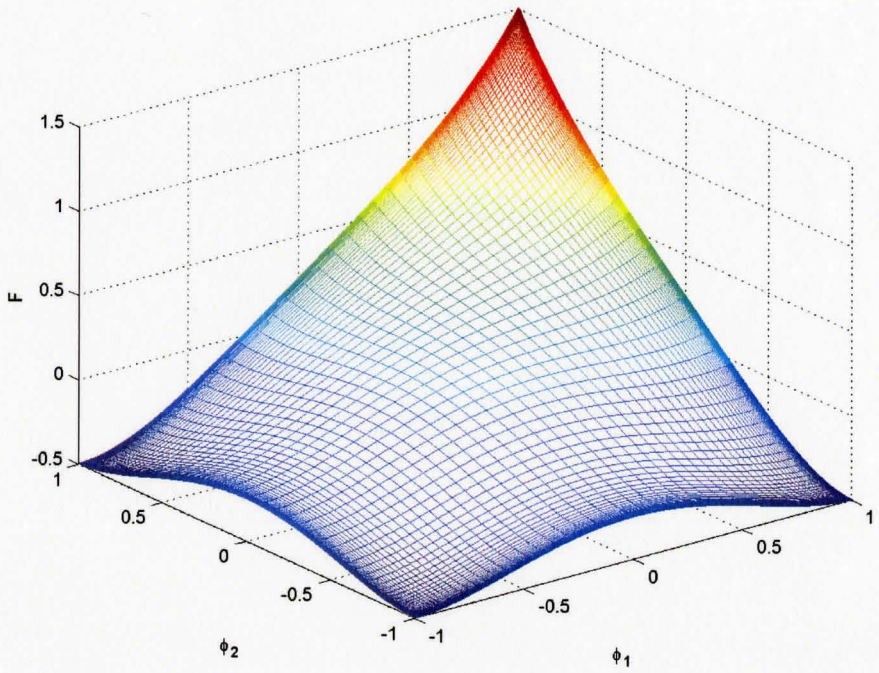

Figure 3.3: Multi-Phase field free energy functional, neglecting gradient term and with $\alpha_{obs} = 1$.

$$\begin{aligned}\frac{\partial \phi_i}{\partial t} &= -\Gamma_{\phi_i}\frac{\delta F}{\delta \phi_i} + \eta_i(\vec{x},t) \\ &= -\Gamma_{\phi_i}\Big[-\epsilon^2_{\phi_i}\nabla^2\phi_i - \phi_i + \phi_i^3 + 2\alpha_{obs}\phi_i\sum_{j\neq i}^{N}\phi_j^2\Big] + \eta_i(\vec{x},t), \end{aligned} \tag{3.50}$$

where $i, j = 1, 2, \ldots, N$,Γ_{ϕ_i} is the mobility of each grain and the noise term, $\eta_i(\vec{x},t)$, follows dissipation dynamics.

The above set of equations (Eq. (3.49) and (3.50)), describe a second order transition and therefore cannot describe solidification. This is used to describe the long time kinetics of grain growth and all that is required from the energy functional is the ability to produce infinite number of minima describing grains with different orientations. It can also be seen that, for the simple case when $N = 1$, the functional and kinetic equation will describe the coarsening kinetics of a single grain.

Following the single phase work of Wheeler *et al* [46], the work of Fan and Chen [62] extended the above set of previous equations to model grain growth in two-phase solids of an alloy. Fan *et al.* [63] studied Ostwald ripening in a poly-phase field model of a binary alloy with a free energy of the form [64; 65]

$$F = \int dV\Big\{\Big[\sum_{i=1}^{N}\frac{\epsilon^2_{\phi_i}}{2}|\vec{\nabla}\phi_i|^2 + f(c,\phi_i)\Big] + \frac{\epsilon_c^2}{2}|\vec{\nabla}c|^2\Big\}, \tag{3.51}$$

Adopting the approach of Kim [48] they define two types of concentrations, c_s and c_l. The physical concentration, c, across any grain boundary is then interpolated as (see Eq. (3.45))

$$c = c_s p(\phi_i) + c_l(1 - p(\phi_i)). \tag{3.52}$$

where $p(\phi_i)$ is an interpolation function with limiting values between [0,1]. The free energy density $f(c, \phi_i)$ is then written as [48; 64; 65],

$$f(c, \phi_i) = p(\phi_i) f_l(c_s, T) + (1 - p(\phi_i)) f_l(c_l, T) + H f_{\mathrm{D}}(\phi_i) \tag{3.53}$$

where H is the height of the double well, i.e. nucleation barrier, $f_{\mathrm{D}}(\phi_i))$ is the double well, and f_s and f_l are the chemical free energies of the form Eq. (3.37) and their extensions. The chosen functions are such that,

$$p(\phi_i) = \sum_{i}^{N} \phi_i^3 (6\phi_i^2 - 15\phi_i + 10) \tag{3.54}$$

and

$$f_{\mathrm{D}}(\phi_i) = \sum_{i=1}^{N} \phi_i^2 (1 - \phi_i)^2 + \alpha_{obs} \sum_{i=1}^{N} \sum_{j \neq i}^{N} \phi_i^2 \phi_j^2 \tag{3.55}$$

The evolution equations follow from the by-now familiar variational principle, where we have, neglecting noise terms

$$\begin{aligned} \frac{\partial \phi_i}{\partial t} &= -\Gamma_{\phi_i} \frac{\delta F}{\delta \phi_i} \\ &= -\Gamma_{\phi_i} \left[\frac{\partial f(c, \phi_i)}{\partial \phi_i} - \epsilon_{\phi_i}^2 \nabla^2 \phi_i \right], \end{aligned} \tag{3.56}$$

and

$$\begin{aligned} \frac{\partial c}{\partial t} &= \vec{\nabla} \cdot \left[\Gamma_c(\phi, c) \vec{\nabla} \frac{\delta F}{\delta c} \right] \\ &= \vec{\nabla} \cdot \left[\frac{v_o}{RT} c(1 - c)[D_s p(\phi_i) + D_l(1 - p(\phi_i))] \vec{\nabla} \cdot \left(\frac{\partial f(c, \phi_i)}{\partial c} - \epsilon_c^2 \nabla^2 c \right) \right]. \end{aligned} \tag{3.57}$$

Operationally, this model must first solve Eq. (3.46) at each point in space to obtain c_s and c_l for a given local concentration and temperature. The concentrations are then put back into $f(c, \phi_i)$ via Eq. (3.52) and then Equations (3.56) and (3.57) updated.

In this formulation, the classical sharp interface limit is used to tune the coefficients to the interfacial energy γ. Defining the interface width as 2Λ, $\gamma = \epsilon\sqrt{H}/3\sqrt{2}$ and $2\Lambda = \alpha\sqrt{2}(\epsilon\sqrt{H})$ [64; 65] where α is dependent on how the interface is defined** [48]. In the general philosophy of the phase field method, anisotropy is considered through angular dependence on the gradient energy and the mobility coefficients.

There is yet another school of multi-phase field modeling, first developed by Steinbach *et. al* [66] and which can be used to model poly-crystalline, multi-phase problems. The characteristic difference between the model of Chen and co-workers and that of Steinbach and co-workers is that in the latter formulation, there is a deviation from the order parameter definition for the phase field, to that of volume fraction. In doing so, it is required that at all time that $\sum_i^N \phi_i = 1$. This also then imposes a constraint through a Lagrange multiplier in order to enforce the conservation of volume fraction. It should be noted that while these models are referred to as "phase field models" they really break from the original traditions of phase field models because they are not using true order parameters.

The majority of multi-phase field models –whether used to model multiple phases or crystal orientations– fail to capture the correct sharp interface kinetics of free boundary motion. This is not a problem when applied to coarsening, ripening and select solid state problems, as the artificial kinetic corrections alluded to in Section 3.5.2.1 are typically negligible. However, most of these multi-phase models may not

**For example $\alpha \simeq 2.2$ when the interface is described by the level set of points satisfying $\phi(\vec{x}, t) = z_i$, where $0.1 < z_i < 0.9$ or $\alpha \simeq 2.94$ when described by the set of points $0.05 < z_i < 0.95$ [48]

be reliable in capturing the correct dendritic growth kinetics prior to dendrite coalescence, a critical feature for modeling the full spectrum of solidification.

3.7.2 Orientational Order Parameter Polycrystalline model

The second formulation used to address polycrystalline solidification is the orientational order parameter model (*theta-phi* model). In this formulation a second non conserved order parameter, $\theta(r,t)$, is required along with the phase field and the concentration/temperature field. The orientational field, θ, measures the orientation of a crystal with respect to some fixed coordinate system, with the field losing all meaning in the liquid phase.

The theta-phi formalism began with the work of Kobayashi and co-workers [67; 68] as an alternative to the multi-phase field approach. A brief introduction to model, for solidification of a pure material, was presented along with one dimensional simulation results and preliminary two dimensional test results. A more detailed work for solidification of a pure material and a full extension to two dimensional simulations, which considered grain boundary energy, impingement, coarsening and grain boundary melting was later presented [69]. It was then extended to binary alloy solidification by Gránásy and co-workers [70; 71; 72] where they considered nucleation and the subsequent growth processes in a binary alloy. The current state of the formulation for solidification of a binary alloy in two dimensions, based on work by Gránásy and co-workers, has this functional form;

$$F = \int_V dV \left[\frac{\epsilon_\phi^2 T}{2} |\vec{\nabla}\phi|^2 + \frac{\epsilon_c^2 T}{2} |\vec{\nabla}c|^2 + f(\phi, c) + f_{\text{ori}}(\phi, |\vec{\nabla}\theta|) \right], \tag{3.58}$$

where $f(\phi,c) = H(c)Tf_{\text{D}}(\phi) + p(\phi)f_s(c,T) + (1-p(\phi))f_l(c,T)$ is the free energy density and $f_{\text{ori}}(\phi, |\vec{\nabla}\theta|) = STp(\phi)|\vec{\nabla}\theta|$ is the orientational energy density. $H(c) =$

$(1-c)H_A+cH_B$ is energy scale proportional to the nucleation barrier height, where it has been defined to depend on concentration via the ith component. S is a constant and determines the energy of low-angle boundaries, i.e. grain boundary energy and given a double well of $f_{\mathrm{D}} = \phi^2(1-\phi)^2$, and an interpolation function of $p(\phi) = \phi^3(6\phi^2-15\phi+10)$. The θ, in current works, assumes a definition only in the crystalline phase ($\phi = 1$), scaled between 0 and 1, while it fluctuates in time and space in the disordered phase.

The dynamic equations for c and ϕ follow from the usual variation principles of the phase field methodology,

$$\frac{\partial \phi}{\partial t} = \Gamma_\phi \left[\epsilon_\phi^2 \nabla^2 \phi - H(c) T f'_{\mathrm{D}}(\phi) - p'(\phi) \Big(f_s(c,T) - f_l(c,T) + ST|\vec{\nabla}\theta| \Big) \right], \quad (3.59)$$

$$\begin{aligned} \frac{\partial c}{\partial t} =& \vec{\nabla} \cdot \left\{ \frac{v_o}{RT} c(1-c)[D_s p(\phi) + D_l(1-p(\phi))] \right. \\ & \left. \vec{\nabla} \cdot \left[(H_B - H_A) T f_{\mathrm{D}}(\phi) + p(\phi) \frac{\partial f_s}{\partial c}(c,T) + (1-p(\phi)) \frac{\partial f_l}{\partial c}(c,T) - \epsilon_c^2 \nabla^2 c \right] \right\}. \end{aligned} \quad (3.60)$$

Care must be taken in deriving the equation for the orientation order parameter and its treatment during simulation, since it is prone to produce singular diffusivities. Kobayashi and Giga [73], have outlined the proper steps to be taken in deriving such a variational and how it should be dealt with. The evolution equation is then,

$$\frac{\partial \theta}{\partial t} = \Gamma_\theta S T \vec{\nabla} \cdot \left[p(\phi) \frac{\vec{\nabla}\theta}{|\vec{\nabla}\theta|} \right]. \quad (3.61)$$

Anisotropy again enters through the gradient energy coefficient and mobility of the phase field, ϕ, through an angular dependence. Since this formulation is built on

earlier works, they can be made to emulate the classical sharp interface equations in the limit of vanishing interface width. They do not, however, possess a thin interface limit, (i.e the ability to emulate sharp interface kinetics when the phase field interface is diffuse).

3.8 Summary

We have in this chapter discussed the origins and phenomenology of the phase field method, its components, dynamics and evolution equations. We have touched on how it gives rise to interfacial energy and anisotropy, its formulation to simulate pure and alloy solidification. The matched asymptotic analysis to derive a thin interface limit and work in correcting the spurious effects (while exploiting the benefits of the thin interface analysis) due to the diffuse interface has made the method quite a powerful tool in conducting quantitative simulations of single phase single dendrite solidification.

Its natural extension to consider polycrystalline solidification, through the multi-phase field and the theta-phi formulations has demonstrated the versatility of the method as well. However, as discussed above, multi-phase field models still lack an appropriate thin interface parametrization required to accurately govern their kinetics during the free dendritic growth phase of solidification, prior to grain coalescence. The multi-phase field method by nature of its formulation requires a large amount of computation to solve the system of equations. The theta-phi models are not subject to such constraints. However, as with the multi-phase field models, models based on an orientational order parameter are similarly lacking a thin interface limit that can instruct the user how to parameterize them to model quantitatively dendritic growth during solidification phenomenon. It should be noted that when an appropriate thin

interface relations become known for theta-phi type models, there are several available advanced computational methods that are best implemented on these types of models. These include adaptive mesh refinement [74]. It should also be noted that recently a theta-phi model has been reported [75] with conditions of Eqs. (3.45) and (3.46) to ensure the decoupling of the concentration field, making an improvement to the model via ability to calculate the surface energy at steady state in terms of model parameters.

It is in the context of these limitations on multi-phase field models and orientational order parameter models that we present the main development of this thesis. It marries the simple binary alloy model of Karma and co-workers –which is well demonstrated to yield quantitative results for free dendritic growth [47; 41; 59; 76; 77]– with the multi-phase field methodology, which has been documented to produce the generic physics of grain boundary interactions [2; 62; 63; 78; 79; 80].

Chapter 4

Quantitative Multi-Phase Field Model for Polycrystalline Solidification

There have been numerous advances that have allowed more practical numerical simulations of phase field models. Some of these advances have been discussed previously, among them is the recent thin interface analysis [42; 43], elimination of the spurious effects due to the interface thickness [47; 41] and increased efficiency due to adaptive mesh algorithms [81; 74]. We extend the anti-trapping formalism and exploit the benefits of the thin interface limit to develop a simple quantitative polycrystalline model for solidification and subsequent growth of binary alloys. The main equations of the model are shown here. Detailed calculations pertaining to the various equations presented are shown in Appendix A.

4.1 Dilute Binary Alloy Model with Multiple Order Parameters

4.1.1 Free Energy

We commence with the free energy of a dilute, ideal binary alloy of species A and B, having N single phase crystals of varying orientation. An order parameter is used to define each grain ϕ_i $(1 \leq i \leq N)$, such that $0 < \phi_i < 1$, with $\phi_i = 0$ and $\phi_i = 1$ representing liquid and solid respectively. We formulate a free energy so that different

order parameters cannot completely overlap guaranteeing that in bulk solid $\phi_i = 1$ while all other parameters $\phi_j = 0$ (for $j \neq i$). The system can then be represented by a state vector $\vec{\phi} \equiv (\phi_1, \phi_2, \phi_3, \cdots, \phi_N)$. In this representation then, liquid is $\vec{\phi} \equiv 0$, and bulk solid of each grain i is $\vec{\phi} = \hat{e}_i \equiv (0, 0, 0, \ldots, \phi_i = 1, \cdots, 0, 0, 0)$, where $\hat{e}_i$ represents a unit vector in this space. The overlapping of two or more grains, i, j, k, etc., is defined by the vector $\vec{\phi} \equiv (0 \cdots \phi_i, \cdots \phi_j, \cdots, \phi_k, \cdots)$ where $0 < \phi_i, \phi_j, \phi_k < 1$ and for consistency, the interaction energy is chosen such that $0 \leq \phi_i + \phi_j + \phi_k + \cdots \leq 1$.

Starting with a free energy functional of,

$$F(c, \vec{\phi}, T) = \int d\mathbf{r} \left\{ \sum_{i=1}^{N} \frac{|\epsilon(\vec{\phi}, \Theta) \nabla \phi_i|^2}{2} + f(\vec{\phi}, c, T) \right\} \tag{4.1}$$

where $\epsilon(\vec{\phi}, \Theta)$ is the gradient energy coefficient for any solid-liquid interface or for any solid i and solid $j(\neq i)$, where Θ is the orientation of grain i referenced to some external axis. The bulk free energy density is $f(\vec{\phi}, c, T)$, is then expanded in c and temperature T, to first order, and to fourth order in the components of $\vec{\phi}$, yielding bulk dilute free energy of

$$\begin{aligned} f(\vec{\phi}, c, T) =& H \sum_{i}^{N} f_{\mathrm{D}}(\phi_i) + f_{\mathrm{int}}(\vec{\phi}) + \frac{RT_m}{v_o} \left[c \ln c - c \right] \\ &+ f^A(T_m) - \Delta T \left[s_l - \frac{L}{T_m} \tilde{g}(\vec{\phi}) \right] + \left[\epsilon_l + \Delta\epsilon \bar{g}(\vec{\phi}) \right] c. \end{aligned} \tag{4.2}$$

The constant H is the barrier height between liquid and solid, $f_{\mathrm{D}}(\phi_i) = \phi_i^2(1 - \phi_i)^2$ is the standard double well potential providing minima wells in pure liquid and pure solid. The function f_{int} sets the energy for interaction between grain i and all other grains $j(\neq i)$. $f^A(T_m)$, is the free energy of pure A calculated at its melting temperature T_m, $\Delta T = T - T_m$, R is the universal gas constant and v_o is the molar volume of solid. Liquid entropy is given by s_l, $\epsilon_l(\epsilon_s)$ are the internal energies of

the liquid(solid), $\Delta\epsilon = \epsilon_s - \epsilon_l$ and L is the latent heat of fusion. The function $\tilde{g}(\vec{\phi})$ interpolates the entropy between solid and liquid, while $\bar{g}(\vec{\phi})$ interpolates the internal energy in an analogous manner. $\tilde{g}(\vec{\phi})$ is constructed to satisfy $\tilde{g}(\vec{\phi} = 0) = 0$, $\tilde{g}(\vec{\phi} = \hat{e}_i) = 1$ and $0 < \tilde{g}(\vec{\phi}) < 1$ and $\bar{g}(\vec{\phi})$ has the same limits and chosen to have the specific form

$$\bar{g}(\vec{\phi}) = \frac{1}{\ln k} \ln \left[1 - (1-k)\tilde{g}(\vec{\phi})\right] \tag{4.3}$$

where k is the partition coefficient. We will define $\tilde{g}(\vec{\phi}) = \sum_i G(\phi_i)$ where $G(0) = 0$,$G(1) = 1$ and $G'(0) = 0$=$G'(1) = 0$ and takes the following algebraic form $G(\phi_i) = \phi_i^3(6\phi_i^2 - 15\phi_i + 10)$.

4.1.2 Phase Diagram

An analysis of the properties of the bulk free energy of Eq. (4.2) begins by computing the equilibrium phase diagram. The generalized chemical potential of this alloy, via $\delta F/\delta c = \mu$, is

$$\mu \equiv \frac{\partial f(\vec{\phi}, c)}{\partial c} = \frac{RT_m}{v_o} \ln c + \epsilon_l + \Delta\epsilon \bar{g}(\vec{\phi}). \tag{4.4}$$

At equilibrium, calculating $\mu = \mu_{\text{eq}}$ in bulk grain $i(\vec{\phi}_o = \hat{e}_i)$ and bulk liquid$(\vec{\phi}_o = 0)$, we obtain

$$\begin{aligned} \mu_s^{\text{eq}} &= \frac{RT_m}{v_o} \ln c_s + \Delta\epsilon + \epsilon_l, \\ \mu_l^{\text{eq}} &= \frac{RT_m}{v_o} \ln c_l + \epsilon_l, \end{aligned} \tag{4.5}$$

where c_s and c_l are equilibrium concentrations at some temperature T. Equilibrium also dictates that we set, $\mu_s^{\text{eq}} = \mu_l^{\text{eq}} \equiv \mu_{\text{eq}}$ giving us the partition coefficient;

$$k \equiv \frac{c_s}{c_l} = \exp\left(-\frac{v_o \Delta\epsilon}{RT_m}\right) \tag{4.6}$$

Performing a double tangent construction, with $f(c_s, \vec{\phi}_o = \hat{e}_i) - f(c_l, \vec{\phi}_o = \mathbf{0}) = \mu_{\text{eq}}(c_l - c_s)$, we get μ_{eq} and the relation for the liquidus line,

$$T = T_m - \left[\frac{RT_m^2(1-k)}{Lv_o}\right] c_l, \tag{4.7}$$

where the liquidus slope is defined by the quantity

$$m_l = -\frac{RT_m^2(1-k)}{Lv_o}. \tag{4.8}$$

4.1.3 Steady State Profiles and Interface Energies

4.1.3.1 Concentration Profile

The steady state concentration across solid-liquid interface is deduced through the equilibrium chemical potential μ_{eq}. This is given by

$$\mu_{\text{eq}} = \frac{RT_m}{v_o} \ln c_o(\mathbf{r}) + \epsilon_l + \Delta\epsilon \bar{g}(\vec{\phi}_o(\mathbf{r})), \tag{4.9}$$

where $c_o(\mathbf{r})$ is the equilibrium concentration across the interface and $\vec{\phi}_o(\mathbf{r}) = (0, 0, 0, \cdots, \phi_i^o(\mathbf{r}), \cdots, 0, 0, 0)$ tracks the planar interface between grain i and the liquid. Using μ_l^{eq} from Eq. (4.5) and solving for $c_o(\mathbf{r})$, we acquire

$$\frac{c_o(\mathbf{r})}{c_l^o} \equiv \frac{c_o(\vec{\phi}_o(\mathbf{r}))}{c_l^o} = \exp\Big(\ln(k)\,\bar{g}(\vec{\phi}_o)\Big), \tag{4.10}$$

where c_l^o is identified as the reference liquidus concentration at some quench temperature. With Eq. (4.10) resembling the form used in [41], we can rewrite it with Eq. (4.3) as

$$\frac{c_o(\vec{\phi}_o(\mathbf{r}))}{c_l^o} = \Big[1-(1-k)\tilde{g}(\vec{\phi}_o)\Big]. \tag{4.11}$$

The vector nature of this formulation and in Eq. (4.10), also allows the identification of the equilibrium concentration across a solid-solid planar interface between two solid grains. The equilibrium phase field vector is then given by $\vec{\phi}_o = (0,0,0,\cdots,\phi_i^o(\mathbf{r}),\cdots,0,0,0,\cdots,\phi_j^0(\mathbf{r}),\cdots,0,0,0)$, where now we have profiles of adjacent grains i and j.

4.1.3.2 Solid-liquid interface energy

The steady state (i.e. equilibrium) phase field profile across a planar interface is the solution of the equation, $\delta F/\delta\phi_i = 0$, in 1D it is

$$\begin{aligned} &W_o^2\frac{d^2\phi_i^o}{dx^2} - \frac{\partial f_D(\phi_i^o)}{\partial\phi_i^o} - \frac{1}{H}\frac{\partial f_{\text{int}}(\vec{\phi}_o)}{\partial\phi_i^o} + \\ &\frac{1}{H}\left[\frac{-\Delta T L}{T_m}\frac{\partial\tilde{g}(\vec{\phi}_o)}{\partial\phi_i^o} - \Delta\epsilon\frac{\partial\bar{g}(\vec{\phi}_o)}{\partial\phi_i^o}c_o(\vec{\phi}_o(\mathbf{r}))\right] = 0 \end{aligned} \tag{4.12}$$

where $W_o = \epsilon_{sl}/\sqrt{H}$ and ϵ_{sl} is the gradient energy coefficient evaluated for a solid-liquid interface. Manipulation using Eq. (4.8) to eliminate L and Eqs. (4.3) and (4.10) and requiring that the collection of terms in the square brackets equals zero, we obtain

$$-\frac{1}{H}\frac{\Delta TL}{T_m}\left[\tilde{g}'(\vec{\phi}_o)+\frac{T_m\Delta\epsilon}{L\Delta T}\bar{g}'(\vec{\phi}_o)c_o(\vec{\phi}_o)\right]=0, \tag{4.13}$$

where primes are derivatives are with respect to ϕ_i^o. Equations (4.12) and (4.13) suggests that concentration completely decouples from the local order parameter at equilibrium, making it feasible to calculate an expression for the surface energy of our solid-liquid interface or solid-solid interface entirely in terms of the steady state order parameter fields. We can then accurately emulate any experimental interface energy without needing to back-engineer the steady state concentration field across the interface, which is a difficult task.

Focusing on an isolated solid-liquid interface, where the interaction energy $f_{\text{int}} = 0$, and our equilibrium phase field is guaranteed viz. Eq. (4.13) to be $\phi_i^o(x) = \left[1-\tanh\left(x/\sqrt{2}W_o\right)\right]/2$, our interface energy is then fixed to be

$$\gamma_{sl} = IW_oH, \tag{4.14}$$

where $I = 1/(3\sqrt{2})$.

4.1.3.3 Solid-solid interface energy using a double obstacle potential

For any arrangement that the phase field profile may assume, at equilibrium, Eqs. (4.10) and (4.13) remain true. In the presence of a solid-solid grain boundary, i.e. when there is some overlap between two or more order parameters, we are assured of the decoupling of the concentration field from the phase field. In this situation however, $f_{\text{int}} \neq 0$ and the interface energy, i.e. grain boundary energy, is solved by the following set of coupled phase field equations,

$$W_o^2 \frac{d^2\phi_i^o}{dx^2} - \frac{\partial f_D(\phi_i^o)}{\partial \phi_i^o} - \frac{1}{H}\frac{\partial f_{\text{int}}(\vec{\phi}_o)}{\partial \phi_i^o} = 0$$
$$W_o^2 \frac{d^2\phi_j^o}{dx^2} - \frac{\partial f_D(\phi_j^o)}{\partial \phi_j^o} - \frac{1}{H}\frac{\partial f_{\text{int}}(\vec{\phi}_o)}{\partial \phi_j^o} = 0, \tag{4.15}$$

with grain i and $j(\neq i)$ being adjacent one to the other. We choose an interaction energy of the form

$$f_{\text{int}}(\vec{\phi}) = \alpha_{\text{obs}} \sum_i \sum_{j \neq i} \phi_i^2 \phi_j^2, \tag{4.16}$$

[82; 83; 64; 65], where α_{obs} is a constant for any two adjacent grains, and in general Eq. (4.15) must be solved numerically*.

Numerically, the solution to Eq. (4.15) can easily be found after which a relation can be made between the solid-solid interface energy, W_o and α_{obs}. Here we choose to reproduce the Read Shockely form of the interface energy, given by

$$\epsilon_{\text{ss}}(\theta, \psi) = \epsilon_o \theta \{1 - \ln(\theta/\theta_m)\}\{1 - \epsilon_4 \cos(4\Psi)\} \tag{4.17}$$

[82; 83], where ϵ_o is isotropic interfacial energy, θ is the local misorientation angle between grains i and j, θ_m is the maximum misorientation at which the grain boundary energy plateaus at a maximum. The angle $\Psi = \psi - \Theta$, where ψ is the local orientation of the grain boundary with respect to some reference axis, and Θ $(= \arctan(\partial_y \phi_i / \partial_x \phi_i))$ is the orientation of the grain i, with respect to some external

*An additional relation that comes from balancing the reduction of thermodynamic free energy (gained by creating one phase below the solidus) and increase in energy of the meta-stable interface material (modeled by the increased interaction term) will generate an additional relation between phi_i and $\phi_{j(\neq i)}$.

reference axis. The local misorientation is defined by means of the order parameters as

$$\theta(\mathbf{r}) = \frac{\sum_{i,j\neq i}^{N} \phi_i^2 \phi_j^2 \vartheta_{ij}}{\sum_{i,j\neq i}^{N} \phi_i^2 \phi_j^2} \tag{4.18}$$

[84], where ϑ_{ij} represents the global misorientation between grains.

4.2 Dynamics

The equation for dynamics follow from the usual phase field philosophy and has the standard form

$$\begin{aligned} \tau(\Psi)\frac{\partial \phi_i}{\partial t} =& \nabla \cdot [W^2(\Psi)\nabla\phi_i] - \partial_x\left(W(\psi)\frac{\partial W}{\partial \psi}\frac{\partial \phi}{\partial y}\right) + \partial_y\left(W(\psi)\frac{\partial W}{\partial \psi}\frac{\partial \phi}{\partial x}\right) \\ & -\frac{\partial f_D}{\partial \phi_i} - \frac{1}{H}\frac{\partial f_c}{\partial \phi_i} - \frac{1}{H}\frac{\partial f_{\text{int}}}{\partial \phi_i} \\ \frac{\partial c}{\partial t} =& \nabla \cdot \left(M(c,\vec{\phi})\nabla\mu\right) \end{aligned} \tag{4.19}$$

where μ is given by Eq. (4.4), $\tau(\Psi) = 1/(K_\phi(\Psi)H)$ and $W(\Psi) = \epsilon(\Psi)/\sqrt{H}$ are constants, K_ϕ is the phase field mobility assumed the same for all grains (ϕ_i). The function f_c is that denoted earlier in Eq. (4.2), the free energy density. The mobility of the concentration field in the dilute limit is given by

$$M(c,\vec{\phi}) = \frac{D_l v_o}{RT_m} q(\vec{\phi}) c. \tag{4.20}$$

$q(\vec{\phi})$ is the interpolation function for solute diffusion across the interface, and is modulated from its liquid phase value D_l to its solid phase value D_s, when $q(\vec{\phi} = 0) = 1$ and $q(\vec{\phi} = \hat{e}_i) = \xi$ respectively, where $\xi = D_s/D_l$.

To demonstrate the thin interface limit of our multi-order parameter model, it is instructive to re-cast $\partial_{\phi_i} f_c(\phi_i, c)$ in a form similar to that developed by Karma and co-workers [47; 41]. Moreover, in order for our model to emulate the correct sharp interface model in the presence of a thin interface, the diffusion equation, Eq. (4.19), must also be augmented with an anti-trapping flux term analogous to that presented in the singe crystal phase field model in Section 3.5.2.1. This flux vanishes when grains impinge and the interface velocity tends to zero.

To re-cast $\partial_{\phi_i} f_c(\phi_i, c)$, we start first with the following sequence of operations:

$$\begin{aligned}
\frac{\partial f_c(\vec{\phi}, c, T)}{\partial \phi_i} =& \frac{\Delta T L}{T_m}\tilde{g}'(\vec{\phi}) + \Delta\epsilon\bar{g}'(\vec{\phi})c \\
=& \frac{\Delta T L}{T_m}\tilde{g}'(\vec{\phi}) + \Delta\epsilon\frac{-(1-k)\tilde{g}'(\vec{\phi})}{\ln k[1-(1-k)\tilde{g}(\vec{\phi})]}c \\
=& \left(\frac{\Delta T L}{T_m} - \frac{c_0^l \Delta\epsilon(1-k)}{\ln k}\frac{c}{c_o(\vec{\phi})}\right)\tilde{g}'(\vec{\phi}) \\
=& \left(\frac{c_l^o \Delta\epsilon(1-k)}{\ln k}\right)\left(\frac{\ln k \Delta T L}{c_l^o T_m \Delta\epsilon(1-k)}c_o(\vec{\phi}) - c(x)\right)\frac{\tilde{g}'(\vec{\phi})}{c_o(\vec{\phi})} \\
=& \frac{c_l^o \Delta\epsilon(1-k)}{\ln k}\left(c_o(\vec{\phi}) - c(x)\right)\frac{\tilde{g}'(\vec{\phi})}{c_o(\vec{\phi})}
\end{aligned} \tag{4.21}$$

Equation (4.21) can be further simplified by introducing the dimensionless chemical potential relative to that of a flat, stationary interface, μ_E allowing us to re-write the last line in Eq. (4.21) as

$$
\begin{aligned}
u &= \frac{v_o}{RT_m}(\mu - \mu_{\mathrm{E}}) \\
&= \frac{v_o}{RT_m}\left(\frac{RT_m}{v_o}\ln c + \Delta\epsilon\bar{g}(\vec{\phi}) + \epsilon_l - \frac{RT_m}{v_o}\ln c_l^o - \epsilon_l\right) \\
&= \ln\left(\frac{c}{c_l^o}\right) - \ln k\bar{g}(\vec{\phi}) \\
&= \ln\left(\frac{c}{c_l^o\left[1-(1-k)\tilde{g}(\vec{\phi})\right]}\right).
\end{aligned} \tag{4.22}
$$

Where we stress that $c_l^o \equiv c_o(T)$, for some reference quench temperature T. This expression, Eq. (4.22), along with Eq. (4.11) can be used to write

$$
\begin{aligned}
\frac{1}{H}\frac{\partial f_c(\vec{\phi},c,T)}{\partial\phi_i} &= \frac{RT_m\ln k}{v_oH}\frac{\Delta T}{m_lc_l^o}\left(c(\vec{x}) - c_o(\vec{\phi})\right)\bar{g}'(\vec{\phi}) \\
&= \frac{RT_m\ln k}{v_oH}\frac{\Delta T}{m_lc_l^o}\frac{(1-k)c_l^o}{\ln k}(e^u-1)\tilde{g}'(\vec{\phi}) \\
&= \lambda\frac{(e^u-1)}{1-k}\tilde{g}'(\vec{\phi})
\end{aligned} \tag{4.23}
$$

where we have defined

$$
\lambda = \frac{RT_m(1-k)^2c_l^o}{v_oH} \sim \frac{1}{H} \tag{4.24}
$$

We then proceed to append to the concentration equation, the anti-trapping current, which has contribution currents from each order parameter. It is given by

$$
\vec{j}_{\mathrm{at}} = a_t(1-k)e^u\sum_i\frac{\partial\phi_i}{\partial t}\frac{\vec{\nabla}\phi_i}{|\vec{\nabla}\phi_i|}. \tag{4.25}
$$

Using Eq. (4.20), Eq. (4.23) and (4.25), the equations of motion, Eq. (4.19), become

$$\tau(\Psi)\frac{\partial\phi_i}{\partial t} = \vec{\nabla}\cdot[W^2(\Psi)\vec{\nabla}\phi_i] - \partial_x\left(W(\psi)\frac{\partial W}{\partial\psi}\frac{\partial\phi}{\partial y}\right) + \partial_y\left(W(\psi)\frac{\partial W}{\partial\psi}\frac{\partial\phi}{\partial x}\right)$$
$$-\phi_i^2(1-\phi_i)^2 - \phi_i\omega_{\text{obs}}\sum_{j\neq i}\phi_j^2 - \frac{\lambda}{(1-k)}(e^u-1)G'(\phi_i), \tag{4.26}$$

$$\frac{\partial c}{\partial t} = \vec{\nabla}\cdot\left(D_l q(\vec{\phi})c\vec{\nabla}u + \vec{j}_{\text{at}}\right), \tag{4.27}$$

where $\omega_{\text{obs}} = \alpha_{\text{obs}}/H$. If we make the coefficients τ,λ and k temperature dependent as described in [49], it is possible to use Eqs. (4.26)-(4.27) to describe non-ideal alloys. Full details of all the equations above are found in the appendix.

In the case of uniform cooling from the liquidus temperature to some final temperature, it is preferable to re-cast Eq. (4.22). Where we now take the chemical potential μ and define it relative to that of the initial liquid μ_∞. We then have

$$\begin{aligned} u &= \frac{v_o}{RT_m}(\mu-\mu_\infty) \\ &= \frac{v_o}{RT_m}\left(\frac{RT_m}{v_o}\ln c + \Delta\epsilon\bar{g}(\vec{\phi}) + \epsilon_l - \frac{RT_m}{v_o}\ln c_\infty - \epsilon_l\right) \\ &= \ln\left(\frac{c}{c_\infty}\right) - \ln k\bar{g}(\vec{\phi}) \\ &= \ln\left(\frac{c}{c_\infty\left[1-(1-k)\tilde{g}(\vec{\phi})\right]}\right), \end{aligned} \tag{4.28}$$

where $c_\infty \equiv c(T_o)$ is the average concentration of the alloy, which is also the initial liquid concentration for the initial liquidus temperature T_o. We can proceed then

$$\begin{aligned} \left(\frac{c(\vec{x})}{c_\infty} - \frac{c_o(\vec{\phi})}{c_\infty}\right)\bar{g}'(\vec{\phi}) &= \left[1-(1-k)\tilde{g}(\vec{\phi})\right](e^u-1)\bar{g}'(\vec{\phi}) \\ &= -\frac{(1-k)}{\ln k}\left(e^u - \frac{c_o^l}{c_\infty}\right)\tilde{g}'(\vec{\phi}), \end{aligned} \tag{4.29}$$

where $c_o^l = c_l(T)$, which is just the liquidus concentration at some final temperature T. We realize the fraction $\frac{c_o^l}{c_\infty}$ can be recast via equations defining the liquidus line.

$$\frac{c_o^l}{c_\infty} = \frac{T(t) - T_m}{T_o - T_m}, \tag{4.30}$$

where $T(t)$ is the changing temperature[†] and T_o is the initial liquid temperature. If we write $T(t) = T_o + \Delta T$, where we can consider $\Delta T = -\dot{q}t$ with $\dot{q}$ being some cooling rate. This and knowing the difference $T_o - T_m = m_l c_\infty$, Eq. (4.30) becomes

$$\begin{aligned}\frac{c_o^l}{c_\infty} =& 1 + \frac{\Delta T}{T_o - T_m} \\ =& 1 + \frac{\Delta T}{m_l c_\infty},\end{aligned} \tag{4.31}$$

The equations of motion, with changes only in the equation for ϕ_i, becomes

$$\begin{aligned}\tau(\Psi)\frac{\partial \phi_i}{\partial t} =& \nabla \cdot [W^2(\Psi)\nabla\phi_i] - \partial_x\left(W(\psi)\frac{\partial W}{\partial \psi}\frac{\partial \phi}{\partial y}\right) + \partial_y\left(W(\psi)\frac{\partial W}{\partial \psi}\frac{\partial \phi}{\partial x}\right) \\ & -\phi_i^2(1-\phi_i)^2 - \phi_i\omega_{\text{obs}}\sum_{j\neq i}\phi_j^2 - \frac{\lambda}{(1-k)}\left(e^u - 1 - \frac{\Delta T}{m_l c_\infty}\right)G'(\phi_i),\end{aligned} \tag{4.32}$$

$$\frac{\partial c}{\partial t} = \nabla \cdot \left(D_l q(\vec{\phi}) c \nabla u + \vec{j}_{\text{at}}\right). \tag{4.33}$$

Along with the changes to the equations of motion, Eqs. (4.32) and (4.33), and the dimensionless relative chemical potential, Eq. (4.28), there is one more change that follows from defining the chemical potential relative to a different reference state. Specifically, if we demand that at equilibrium in the solid, the steady state concentration should be approximately equal to the average concnetration, i.e. $c_o(\vec{\phi}_o(\mathbf{r})) \approx c_\infty$,

[†]This must be assumed to change slowly for the quasi-stationary temperature approximation being made here to apply.

then it is straight forward to show that the new equilibirum steady state equation for concentration is,

$$\frac{c_o(\vec{\phi}_o(\mathbf{r}))}{c_\infty} = \frac{1}{k}\left[1-(1-k)\tilde{g}(\vec{\phi}_o)\right]. \tag{4.34}$$

Chapter 5

Dendritic Growth and Coalescence Properties of Multi-Phase Field Model

This chapter will begin with the numerical implementation of our multi-phase field model and our extension of the Adaptive Mesh Refinement (AMR) algorithm by Greenwood [85]. We will then turn to the main focus, which is to study the properties, characteristics, and behavior of the model. Mainly; the free growth of dendrites, where we show the convergence of growth rates and segregation profiles, the steady state and equilibrium properties dealing with the coalescence behavior and finally the excess grain boundary energy.

5.1 Length Scale Disparity and Adaptive Mesh Refinement

The phase field equations being diffusion type equations, the easiest method to solve these partial differential equations is a simple finite difference scheme updating each grid point via explicit time marching. The domain of interest is turned into a uniform mesh of grids, with some grid spacing Δx, and the differentials being approximated by finite differences. With solidification, the final microstructure being on the order of scale of the diffusion length (D/V), 10^{-4} m or more, and the typical scale of an interface (W_o) on the order of 10^{-9} m, there exists a disparity in the change of length scale of about 10^5–10^6 m. Even with limiting simulations to two dimensional

domains, based on the scales alone, one would require about 10^{10}–10^{12} grids points on a uniform mesh to be resolved adequately. This amounts to impractically long computation times. Matched asymptotic analysis, by virtue of using a thicker interface (specifically, $10 < W_o/d_o < 100$, where $d_o \approx 10^{-9}m$) while maintaining sharp interface kinetics, was the first step in attempting to rectify this computational issue. The second is a numerical technique known as adaptive mesh refinement, which dynamically increases the number of grid points where they are needed (i.e. the interfacial region), and decreases it else where (i.e. bulk regions).

The adaptive mesh routine creates a disordered non-uniform mesh, where there is a higher density of grid points at the interfacial region than the bulk. Dynamically, this is accomplished by setting a refinement condition. A simple condition can be set via linear combination of gradients in phase and concentration as,

$$|\nabla\phi| + \varsigma|\nabla c| > threshold. \tag{5.1}$$

We have extended the algorithm developed by Michael Greenwood [85], for single phase solidification and extended it to simulate multiple, coupled order parameters. We have also added a homogeneous nucleation routine to seed simulations with random initial solid nuclei. This allows us the ability to generate, N randomly distributed and oriented grains to perform simulations. Figure 5.1 illustrates a time slice in the growth of nine randomly oriented dendrites growing into a domain at a fixed supersaturation.

5.2 Free Growth of Dendrites

One of the most critical features of our model is to require that during solidification, we recover the correct behavior of the free growing dendrites. The conver-

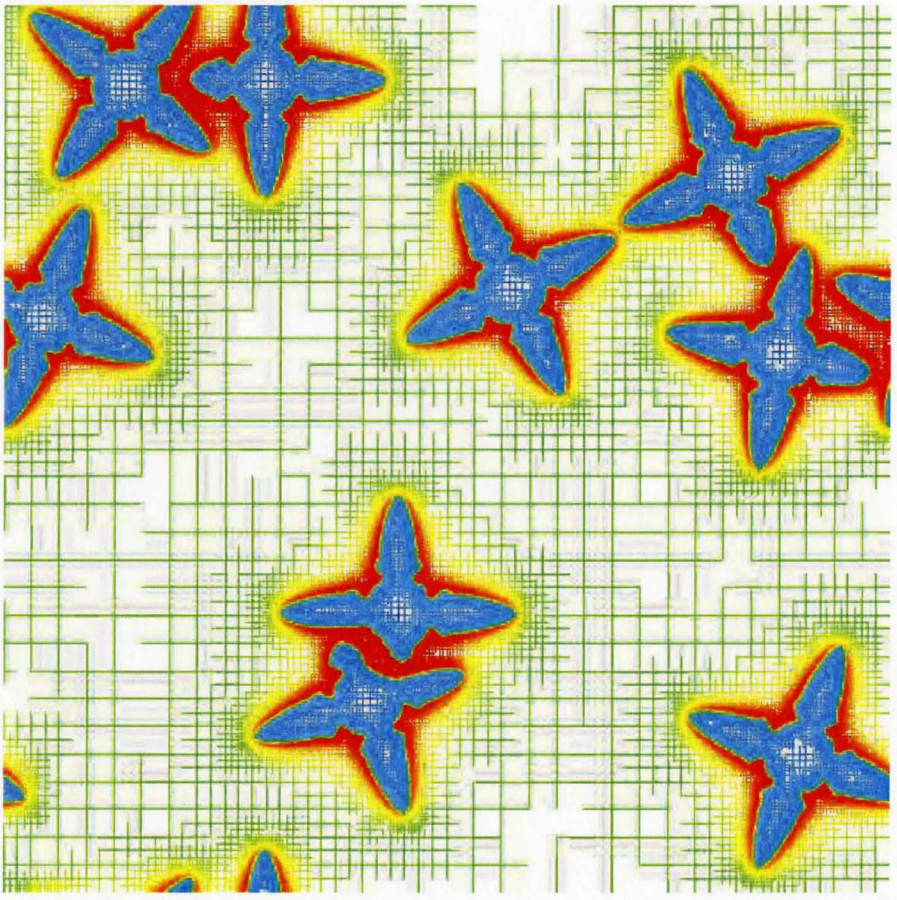

Figure 5.1: Concentration map of nine randomly distributed oriented dendrites. The interface has higher resolution adapted where it is needed in comparison to other areas.

gence of the model was studied by conducting two dimensional simulations of isothermal free dendritic growth. The anisotropy was chosen to be the standard fourfold $W(\psi) = W_o a_s(\psi)$, of the form $a_s(\psi) = 1 + \epsilon_4 \cos 4\psi$ and by choosing $\tau(\psi) = \tau_o a_s(\psi)^2$ and $\lambda = D\tau/a_2 W^2$, the kinetic coefficient term β is made vanish. Equations (4.26) and (4.27) were simulated with a simple finite difference Euler method scheme, where $W_o = \tau_o = 1$ for considering dimensionless form. Two grains were simulated ($N = 2$), each at an orientation of 45 degrees, with respect to the x-axis (horizontal). The other phase field model parameters used are listed in Table 5.1. The initial condition comprised of two circular seeds of radius $r = 22d_o$, $u = \ln[1 - (1 - k)\Omega]$, where the supersaturation $\Omega = (c_l - c_o)/(c_l - c_s)$ with c initially defined by Eq. (4.22).

Parameter	Value
ϵ_4	0.02
k	0.15
Δx	0.4
Δt	0.018
Ω	0.55
a_t	$1/2\sqrt{2}$

Table 5.1: Parameters for free growth

We plot the scaled dimensionless dendrite tip velocity vs scaled dimensionless time in Fig. 5.2 measured along the dendrite axes. As shown in Ref. [47], convergence of the model implies that results for different interface widths (W_o) must converge onto the same solution. The plots for the different ratios of d_o/W_o, must thus superimpose when there is convergence. As can be seen from Fig. 5.2, for the different ratios and for the two misoriented grains, we get full convergence of dendritic tip growth rates.

We also present the segregation results at a time interval along with the progression of the phase field at the same time interval in Fig. 5.3. Again, we get convergence of the concentration profiles according to what is predicted by the equilibrium phase

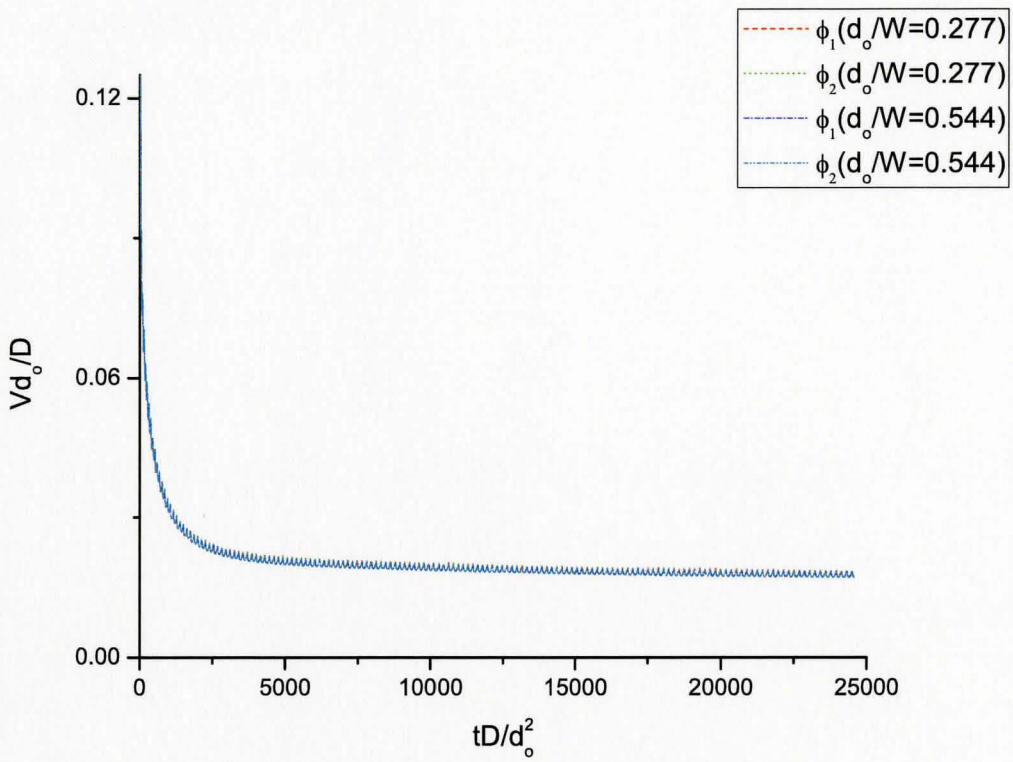

Figure 5.2: Scaled dendrite tip velocity vs scaled time for two different ratios of d_o/W_o, with parameters from Table 5.1.

diagram, i.e. solute partitioning according to the ratio k, for different values of the ratio d_o/W_o.

When solidification is complete or almost complete (when impingement begins), the anti-trapping current should vanish as it scales with the $\partial_t\phi$ term which stops changing as dendrite interfaces slow down. To ensure that indeed the $\vec{j}_{at}$ vanishes from the flux equation, we show a succession of plots depicting the current as the free growth progresses and the dendrites are on the verge of impingement. Combined, The different frames of Figure 5.4 show the evolution of the current as the two dendrite tips in Fig. 5.3 come together, clearly this figure (5.4), demonstrates that indeed the current term becomes negligible as the grains come close to impingement.

The quantitative capability of the present model has been demonstrated during the free growth regime of solidification. We can thus assert that during free growth we are able to emulate the correct kinetic behavior with our model, i.e. convergence with respect to varying interface thickness and correspondence with the sharp interface kinetics of Eqs. (2.13–2.15).

5.3 Coalescence

When free growth is complete, the microstructure consists of a dendritic network with semi-liquid pools in the inter-dendritic regions. In this section, coalescence properties of the model are tested. We follow, as a benchmark, the sharp interface and phase field work of Rappaz and co-workers [2]. As in their work, we consider our model in one dimension for convenience and clarity.

As discussed in Section 2.3, aid of back diffusion is necessary during coalescence in alloys. We consider a generic dilute binary alloy with parameters corresponding to those in Table 5.2.

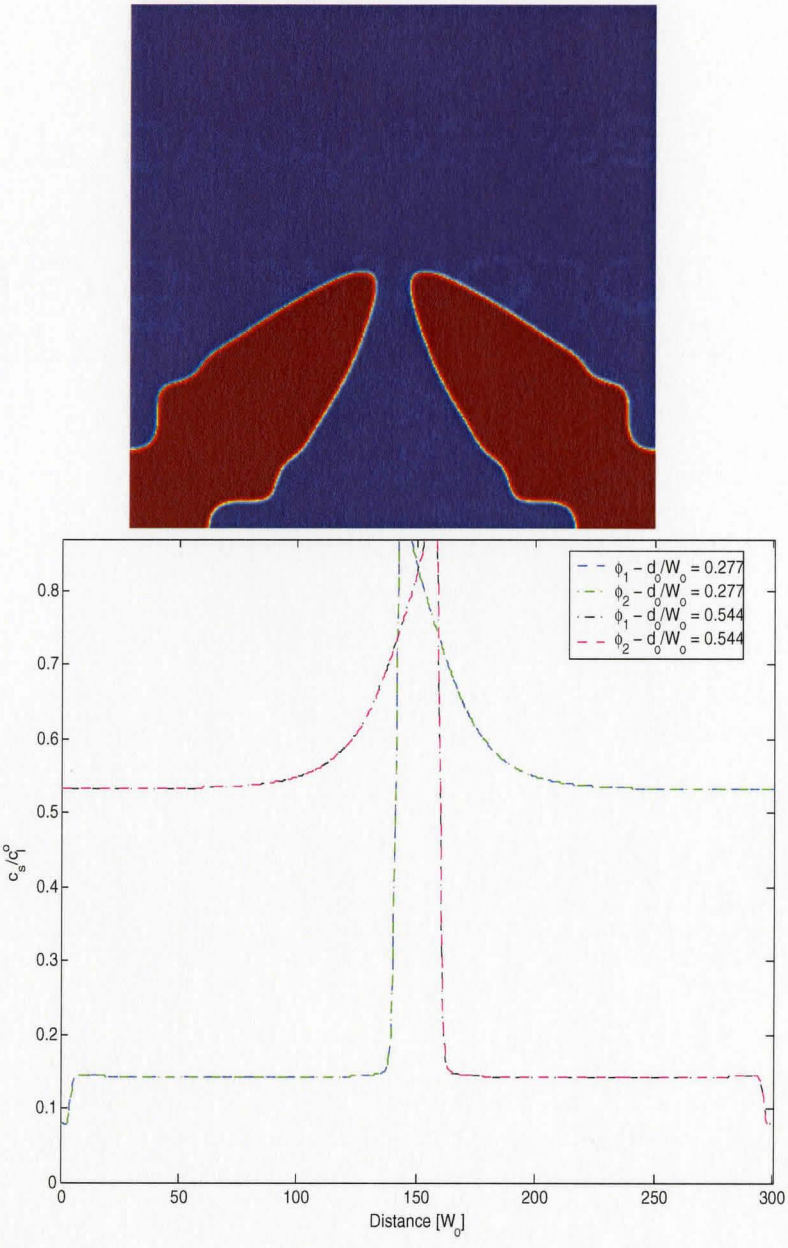

Figure 5.3: Phase field (top) and concentration (bottom) maps of the misoriented grains at time $1280\tau_o$.

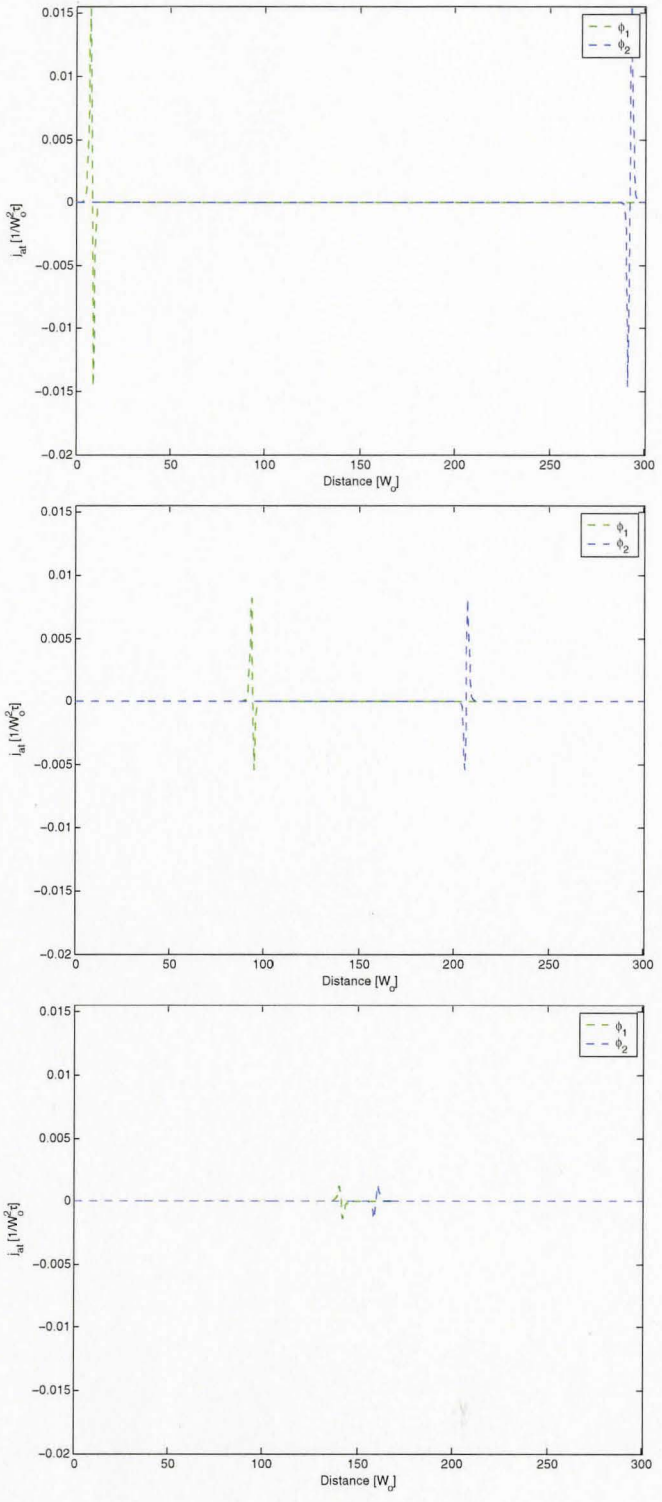

Figure 5.4: Time evolution of anti-trapping flux. From top to bottom at times of, $8\tau_o$, $720\tau_o$ and $1280\tau_o$ respectively.

T_m	1000K
m_l	-500K
k	0.15

Table 5.2: Parameters corresponding to a general dilute alloy

We begin our simulations either at or close to the liquidus temperature of our alloy. We utilize the equations of motion suited for the uniform cooling of an alloy from the liquidus, Eqs. (4.32) and (4.33). Along with the parameters of Table 5.2, and the definition $d_o = \gamma_{sl} T_m / (L|m_l|(1-k)c_o/k)$, freedom is given to choose our interface width, W_o or λ respectively. Simulating with negligible kinetic coefficient, $\beta = 0$, all other the parameters are determined from the thin interface equations, Eqs.(3.34) and (3.35). We set the diffusion in the solid, per the ratio ξ , discussed in Section 4.2, to investigate the importance of back diffusion.

5.3.1 Equilibrium Properties

It is important to ensure that our steady state and equilibrium predictions of the model are obeyed. These calculations are done with the parameters listed in Table 5.3. In this set of equilibrium calculations, we cool to a certain temperature, $\Delta T = 220$K below the initial liquidus temperature, at an average alloy concentration of $c_o = 0.05$, and hold until equilibrium is reached.

W	$5E-8$	m^2
γ_{sl}	1	$\mathrm{J/m}^2$
D_l	$1E-10$	m^2/s
$\dot{q}$	-5	K/s
L_f	$1E9$	$\mathrm{J/m}^3$
c_o	0.05	

Table 5.3: Dynamic simulation parameters

We first tested the case of zero misorientation. For this case, interface merger is defined as the condition when $\phi_1 + \phi_2 = 1$ (or $\phi_1 + \phi_2 = 0$ in units used here where $-1 < \phi_i < 1$). In Fig. 5.5, we show the evolution of the average concentrations in the solid and liquid superimposed on the phase diagram as equilibrium is reached. Also shown in Fig. 5.5 is the solid fraction, evolving from right to left. Figure 5.6 shows the corresponding equilibrium phase and concentration profiles. It is encouraging to note that, in the interface region, the calculated concentration profile from the phase field simulation matches the steady state prediction of Eq. (4.34) within about 4% or less. In this test, steady state was reached when $\phi_1 + \phi_2 \approx -0.05$. If the interaction parameter is tuned to make this sum closer to zero, the concentration would become flat and equal to the average value*.

For misoriented interfaces merger will not occur at $\phi_1 + \phi_2 = 1$ (or $\phi_1 + \phi_2 = 0$), which is controlled by the interaction term. A sufficiently large value of ω_{obs} can be chosen to avoid ever having complete overlap (within all practical cooling ranges). We run the same calculation for the same set of parameters as Fig. 5.6, except we change ω_{obs}. The results of such a change, which is equivalent to the consideration of different grain boundary energies, are shown in Fig. 5.7. Note that the calculated steady states and numerically equilibrated phase and concentration profiles once again are in good agreement for the different interaction parameters. Because the interaction parameter has been set so that the total interface order $\phi_1 + \phi_2$ is different in the interface, different degrees of grain boundary segregation are observed as per Eq. (4.11). We also remind the reader that the segregation at the grain boundary is a consequence of the steady state solutions of the phase fields via Eq. (4.11).

*The tediousness of tuning the interaction parameter to set the steady state properties can be avoided by using the volume fraction approach of Folch and Plapp [59]. Unfortunately that phase field free energy has presently only been developed for three order parameters and would be difficult to specialize for many order parameters.

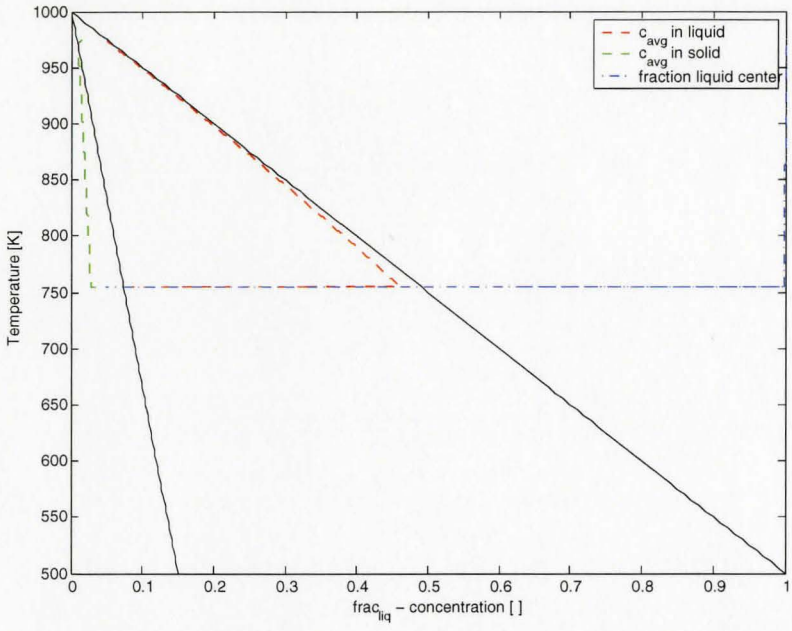

Figure 5.5: Average solid and liquid concentrations for isothermal quench simulations.

Meger becomes possible only because of the induced thermodynamic driving force that develops as a result of back diffusion. Prior to activation of back diffusion, the average concentration in the bulk solid is around c_o (i.e. equilibrium), the concentration in the last liquid film is far above c_o, however the concentration right on the solid side of the interface is higher than c_o but below that of the liquid film. On activation of back diffusion it is the concentration differences between the bulk solid and that of its boundary that induces this driving force. As back diffusion proceeds, the solid concentration ahead of the interface decreases, thereby decreasing the driving force, resulting in the diminished effect of back diffusion. Aside from the decrease in the concentration ahead of the interface, this driving force is also simultaneously competing with the grain boundary energy, which endeavours to preserve the structure and concentration on this boundary. When continuous cooling is considered, the grain boundary energy increases with increasing undercooling (discussed in the sections to

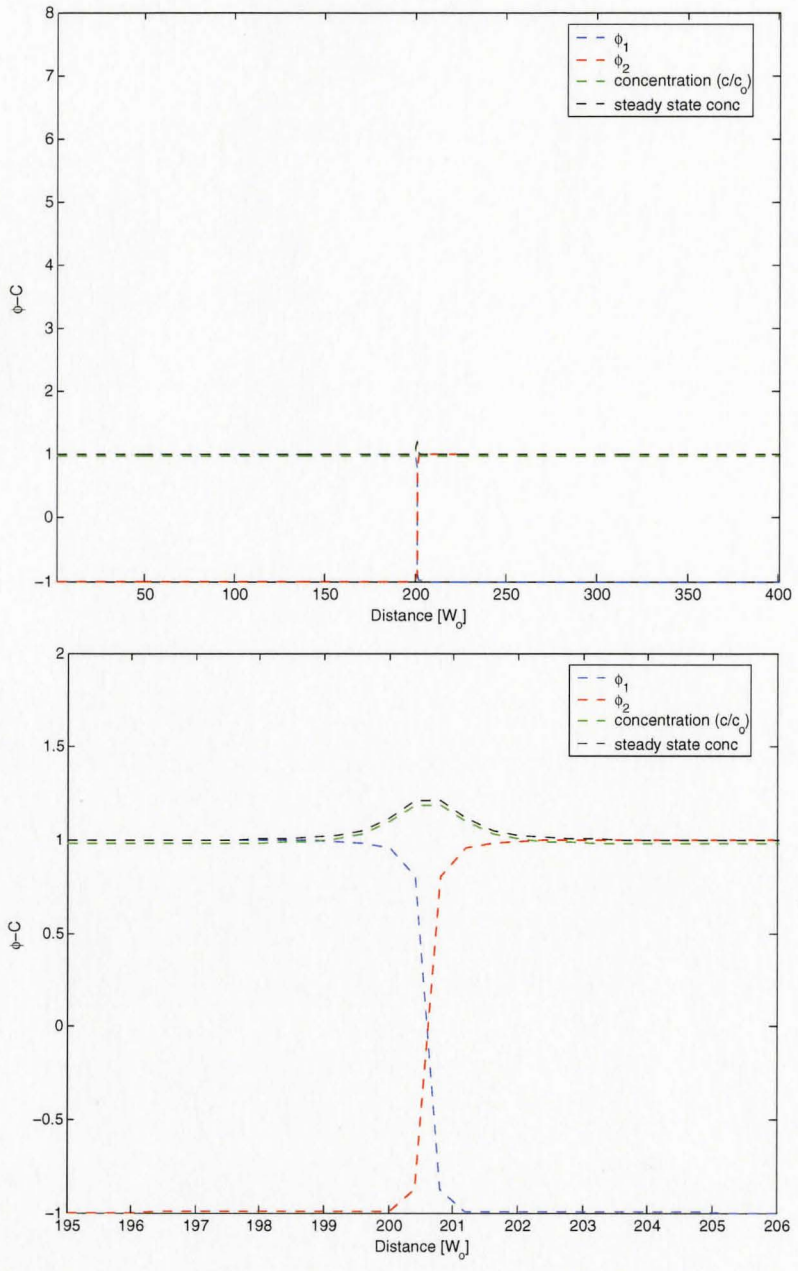

Figure 5.6: Equilibrium profiles of phase field and concentration for $\omega_{obs} = 255$ and $\xi = 10^{-2}$. Bottom figure shows the expansion in the area around the grain boundary, both after the system had reached a steady state.

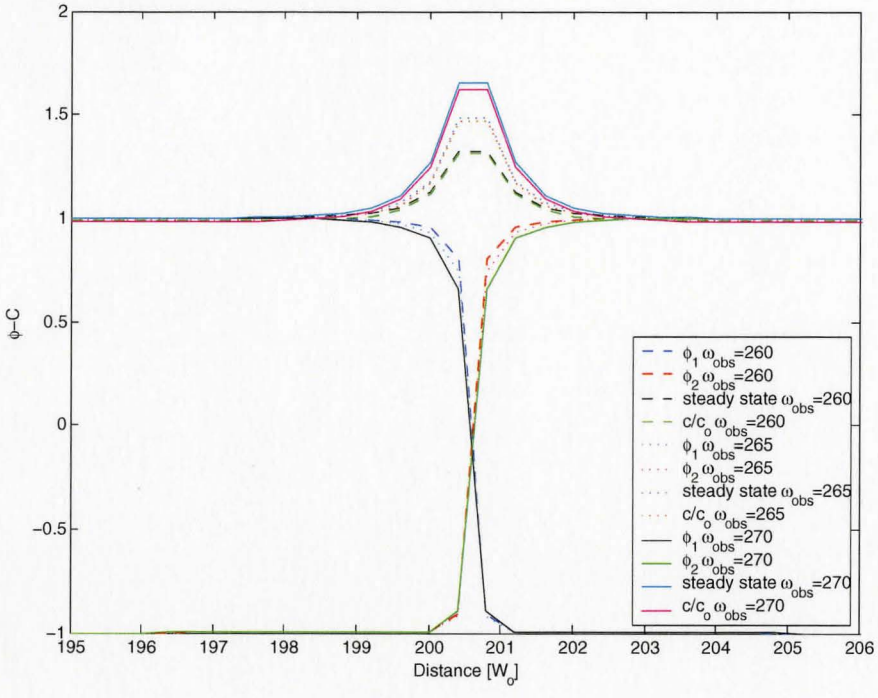

Figure 5.7: Equilibrium profiles of phase field and concentration for different values of the interaction parameter coefficient, ω_{obs}, after steady had been reached and with $\xi = 10^{-2}$.

follow). Therefore the final degree of merger is the compromise of the grain boundary energy in association with the thermodynamic driving force.

5.3.2 Continuous Cooling

We also perform a set of continuous cooling simulations where we observe the effect of different back diffusion coefficients on the solidification path of two coalescing one dimensional interfaces. The results of the calculations are presented in Figure 5.8, where the evolution of the liquid and solid average concentrations are shown superimposed on the dilute binary alloy phase diagram. The specific parameters used for the calculations are listed in Table 5.3. For the data in Fig. 5.8 $\omega_{\text{obs}} = 270$.

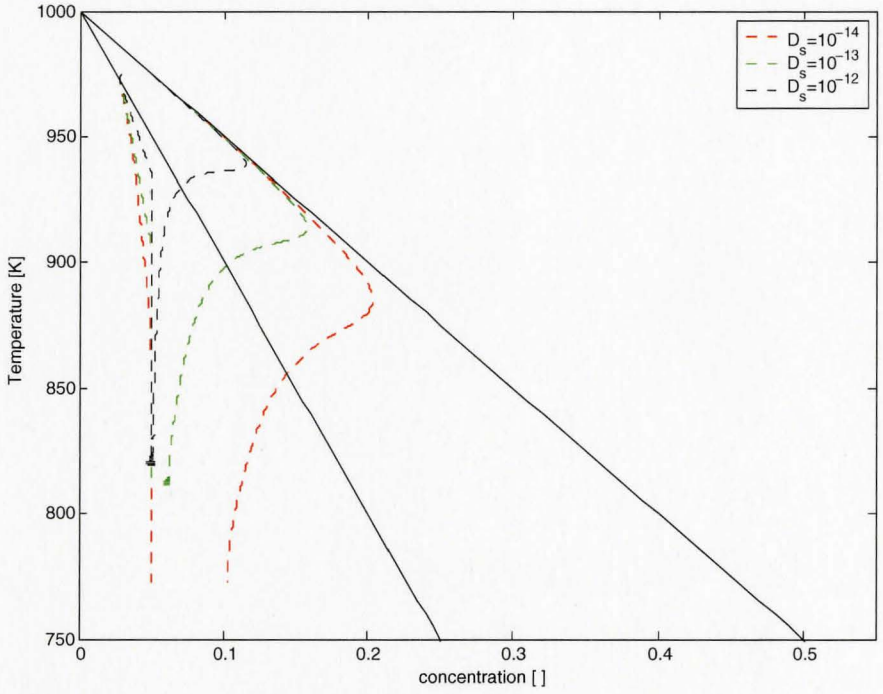

Figure 5.8: Effect of back diffusion on solidification and coalescence.

The behavior of the curves calculated agree qualitatively in every way with those of the sharp interface results discussed in Section 2.3 from Ref. [2]. The differences in

the appearance of the curves can be attributed to the diffusiveness of the interface of the phase field model employed here. From the parameters given we employ a rather thick interface for the purposes of free growth, however upon impingement the use of such a diffuse interface causes some spurious segregation effects. A way to reduce this effect may be to dynamically thin the interface on the onset of merger. In general, however, this deviation from the liquidus line is minor.

As can be seen the liquidus line is followed quite faithfully, until the interfaces approach and start affecting one another in the presence of a large amount of trapped solute in the inter-dendritic film between the grains. Due to the presence of back diffusion we notice a deviation of the average liquidus alloy concentration away from the liquidus line. We also notice the almost stepwise decline of the average liquidus concentration curves with decreasing solid diffusion coefficients. This may suggest the possibility of limits or an asymptotic nature of applying successive lower solid diffusion coefficients.

5.3.3 Grain Boundary Energy Calibration

At grain boundary coalescence, it is important to be able to compute the associated grain boundary energy. To demonstrate how, consider continuously or quasi-statically cooling to a given undercooling for a given interaction parameter ω_{obs}. This will cause two grains to increase their degree of merger, which can be quantified by the total order at the midway between the two grains, $\Phi(0) = \phi_1(0) + \phi_2(0)$. This is shown in Fig. 5.9, which plots Φ vs. ω_{obs} for four ΔT (for simplicity of notation, we drop the "0" from Φ). We recognize a trend in this plot, an increasing driving force (i.e. greater ΔT) and some sufficiently large ω_{obs} seems to result in the approximately

asymptotic behavior, $\Phi(0) \rightarrow 0$. This is evidenced by the almost asymptotic nature by which the curves are spaced together as ΔT increases.

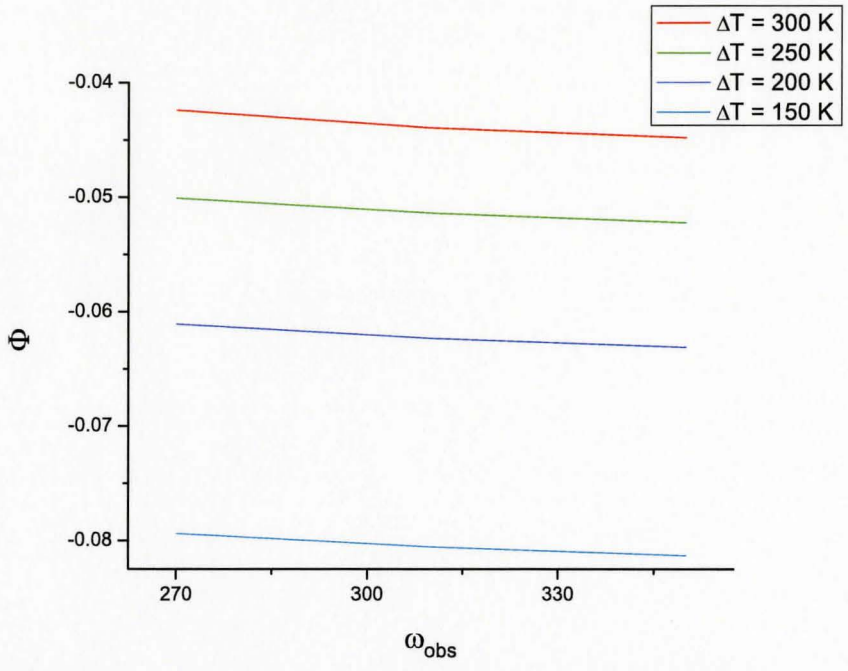

Figure 5.9: Degree of merger, Φ $(\phi_1 + \phi_2)$, as a function of the interaction parameter for selected final undercoolings.

At steady state (i.e. after grain merger stops) we can compute the energy associated with such a steady state construction. Numerically this is accomplished by the following equation

$$\gamma_{gb}(\Phi) = \int_{-\infty}^{\infty} \sum_{i=1}^{N} \left[W_o^2 \left(\frac{d\phi_i^o}{dx} \right)^2 - \frac{(\phi_i^o)^2}{2} + \frac{(\phi_i^o)^4}{4} + \omega_{\text{obs}} \sum_{j \neq i}^{N} (\phi_i^o)^2 (\phi_j^o)^2 - f_{\text{D}}(\pm 1) \right] dx, \tag{5.2}$$

where the ϕ_i^o denote the order parameter fields at steady state. Note that by construction of our model, the solute dependence of surface energy decouples at steady state, the multi-phase field analogue of the single phase solidification model of Karma

and co-workers [41]. The surface energies at merger is then a function only of the steady state order parameter fields. γ_{gb} is represented in Fig. 5.10 for different values of ω_{obs}.

If we consider the curve for the highest interaction parameter, we notice that if extrapolated, the trend suggests that γ_{bg} grows asymptotically as a power law. Furthermore, the form of the interaction potential implies that the exponent of this power law decreases as ω_{obs} increases. This behavior suggests that ω_{obs} can be tuned so as to control the rate of increase of γ_{gb} as $\Delta T \rightarrow \Delta T^*$, a very large undecooling[†]. It is noted that once a value of ω_{obs} is chosen, the surface energy corresponding to different values of grain boundary mis-orientation can be modulated by changing W_o according to Eq. (4.17).

The over all trend exhibited in Fig. 5.10 is an increasing in energy with an increasing in undercooling. This behaviour has also been reported in the work of Warren *et al.* [69] with the theta-phi model for a pure material. Though this observation may not be intuitive, the rise in energy with undercooling is due to the presence of an undercooled liquid like film. As undercooling is increased, the bulk solid becomes more and more stable, while the thin liquid like film at the grain boundary, which cannot completely solidify (Section 5.3.1), becomes more and more unstable increasing in energy. The grain boundary energy being a measure of the excess energy at the boundary then tallies more of the contribution of this latter energy resulting in the trend exhibited in Fig. 5.10.

[†]Strictly speaking, the diffusion coefficient responsible for back diffusion would be temperature dependent per the form $D = D_o \exp(Q/RT)$. ΔT^* we refer to would then correspond to a T^* at which point the diffusion coefficient would become negligibly small, halting back diffusion and thus merger.

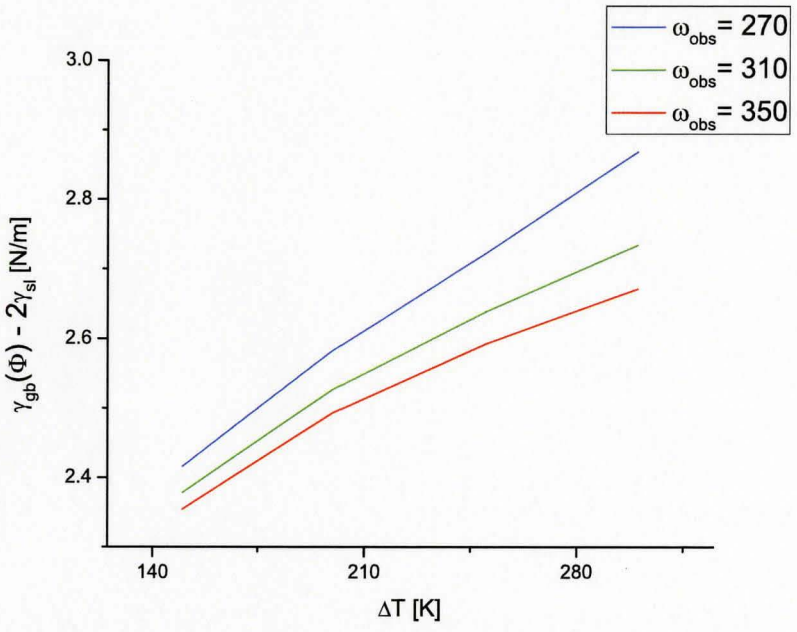

Figure 5.10: Driving force for interface closure versus the excess grain boundary energy for different interaction coefficients.

5.4 Summary

We have demonstrated in the preceding chapter the properties of our model. We have shown that during solidification we quantitatively emulate the right sharp interface kinetics. For several model parameters, convergence is achieved for tip growth rate as well as for segregation. Following the solidification process, we considered the coalescence properties of the model. In reporting on coalescence, we first showed the agreement of our calculated steady state profiles with those predicted analytically. We explored several steady state constructions as a function of altering ω_{obs} and again agreement was found with that predicted from the mathematics. Next we showed the importance of back diffusion and its effects on the solidification path. We found good agreement with previous sharp interface and multi-phase field results regarding this behavior. Finally we showed how to compute the solid-solid grain boundary energy

once steady state had been reached. Due to decoupling of the concentration field at steady state, this energy is a only a product of the steady state profiles of the phase fields.

Chapter 6

Solidification and Coarsening of δ Ferrite

In recent years, the steel industry has slowly been shifting to the use of a new technology to perform casting. This has moved the industry from the traditional ingot casting to the *thin slab cast direct rolling* (TSCDR) technology. This method is more cost and energy efficient compared to traditional methods and with its high through put has made it a commodity in hot mill production. It allows the continuous casting of slabs, which are then subsequently rolled without the need of cooling and then reheating in a furnace. This caster produces "thin" 50–70 mm thick slabs compared to the 200–250 mm slab thicknesses that are conventionally produced. Appended to the end of the caster just before the hot rolling mill is homogenization furnace which allows the slab to maintain a relatively constant temperature,1000–1150 °C for upwards of thirty minutes, while the slab is cast to the appropriate length for rolling [86; 87].

The process has become the choice when it comes to casting and processing of American Petroleum Institute (API) standard microalloyed steels. However a threshold has been reached due to the nature of the method. Conventionally thermomechanical processing was the primary source for the grain refinement of steels, and with the TSCDR this was still the practice. The API standards require products to have among other properties, a high strength, high toughness, and a low ductile to brittle transition temperature (DBTT). The TSCDR was well suited for this kind of production, as the direct link and control resulted to remarkable microstructure

refinement. But the increasing demand for hot-rolled products with much higher strength through fine and ultra fine grain sizes has resulted in an obstacle. Conventionally, the premise of microalloying was intended to refine microstructures through precipitation of carbides and nitrides that act as pinning forces to grain boundary motion thereby allowing an increase in strength. However in the case of the present technology, there seems to an issue of attaining all necessary characteristics. This is due to the introduction of the following changes due to the nature of technology [88; 89]: (i) the reduced size of the slab thickness means that thin slabs solidify more rapidly than traditional slabs. This means that there are smaller dendritic arm spaces leading to smaller segregation leading to more chemically homogeneous structure; and (ii)coarse austenite grain size before hot rolling; (iii)limited reduction via thermomechanical processing. These changes significantly influence and alter the effects of microalloying thereby affecting downstream operations. This implies that parameters governing the initial state of the process, i.e. solidification and subsequent coarsening of the primary solidification phase, are now important factors in the ability to produce higher grade steels.

Since the initial microstructure of the primary phase (δ ferrite) sets the template for subsequent microstructures, it becomes useful to use phase field models such as the one developed in this thesis to examine heating schedules that can lead to different delta growth and coarsening scenarios.

We end this thesis by demonstrating the robustness of our model to deal with solidification, impingement and coarsening of multiple grains, under cooling conditions that are extracted directly from industrial steel processing. The detailed quantification of delta ferrite grain distributions will be the topic of future studies, which will use the model developed herein.

We consider the $Fe - C$ phase diagram in the δ region where we consider the dilute limit. The corresponding phase diagram generated by ThermoCalc is shown in Fig. 6.1. From Fig. 6.1 and data from ThermoCalac we are able to put forth the parameters of the phase diagram if only considering the dilute limit. This data, which was used to set the phase diagram parameters for our simulations is reported in Table 6.1.

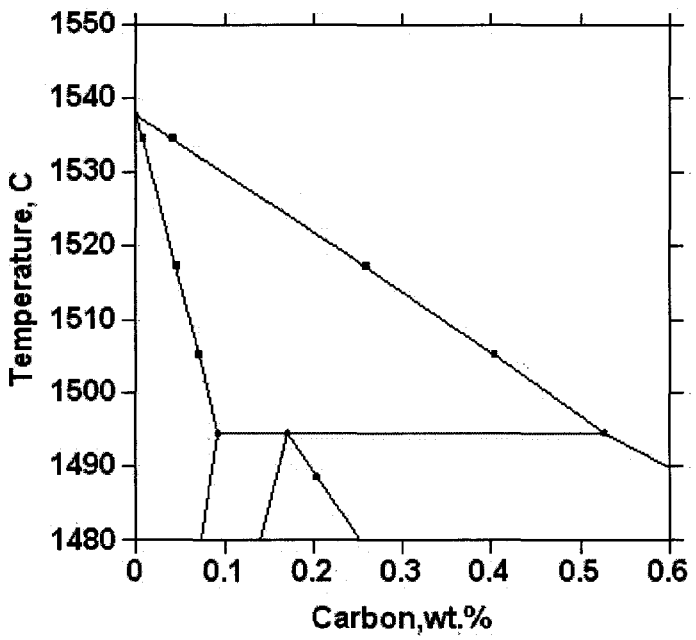

Figure 6.1: Phase diagram of Fe-C expanded in the two phase region considering δ-ferrite.

T_m	1538°C
m_l	−81°C/wt%
k	0.17

Table 6.1: Dilute phase diagram parameters for Fe-C.

For all other parameters for the simulation, we use the parameters listed in Table 6.2. The anisotropy was chosen to be the standard fourfold $W(\Psi) = W_o a_s(\Psi)$, of the form $a_s(\Psi) = 1 + \epsilon_4 \cos 4\Psi$ and by choosing $\tau(\Psi) = \tau_o a_s(\Psi)^2$ and $\lambda = D\tau/a_2 W^2$,

the kinetic coefficient term β is made to vanish. Equations (4.32) and (4.33) were simulated on the AMR algorithm where $W_o = \tau_o = 1$. We begin our simulation by homogeneously seeding 10 grains randomly each with a random orientation and random initial radii. The last was done so as to emulate different nucleation times for each seed.

W	$5E-8$	m^2
γ_{sl}	1.8	J/m^2
D_l	$1E-10$	m^2/s
D_s	$1E-11$	m^2/s
$\dot{q}$	-5	K/s
L_f	$1E11$	J/m^3
ϵ_4	0.02	
Δx	0.4	
Δt	0.001	
ω_{obs}	270	
a_t	$1/2\sqrt{2}$	
c_o	0.05	

Table 6.2: Simulation parameters for δ-ferrite process.

Several time slices of the simulation results are shown in Fig. 6.2, where the concentration field is plotted. In Fig 6.2 (the last insert), solidification is almost complete and in parts of the figure we already see signs of the onset of coalescence through coarsening. From this initial indication and from the one dimensional analysis, discussed in Chapter 5, the model is clearly capable and robust enough to describe the solidification, growth and coarsening regimes of this particular process and the final structure will be one composed of solid-solid boundaries. In a sequel study, a more indepth analysis will be conducted to fully quantify the coarsening properties and results for this process.

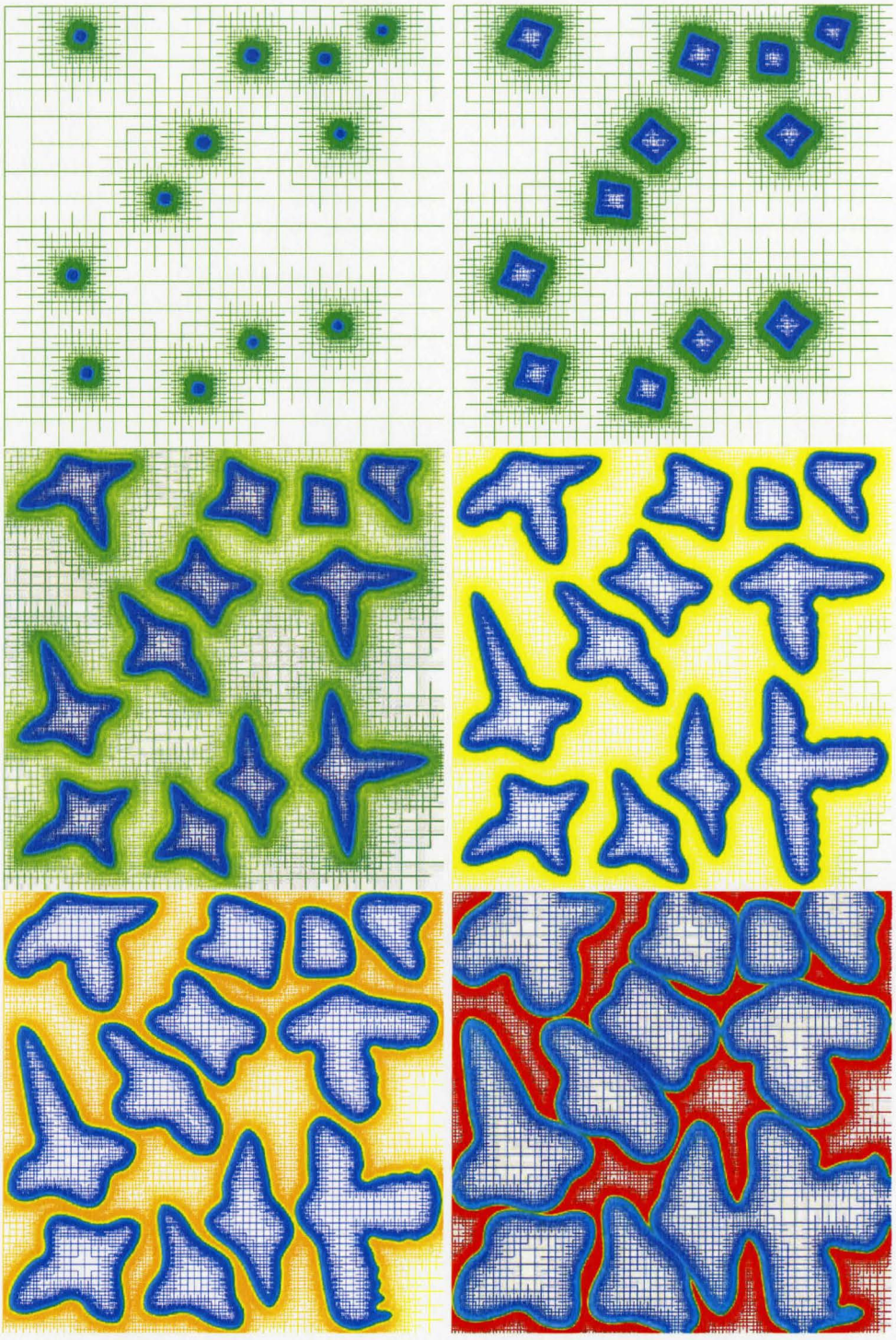

Figure 6.2: Time slices of δ-ferrite coarsening. Showing the concentration map, the high bright hues represent high solute content while the low blue hues represent low solute content. From top to bottom at times of, $10\tau_o$, $100\tau_o$, $200\tau_o$, $300\tau_o$, $400\tau_o$ and $580\tau_o$ respectively.

Chapter 7

Conclusions

We have developed a new multi-phase field model for quantitative simulation of polycrystalline solidification, impingement and coarsening. We have shown that its behavior during free growth is quite agreeable to those quantitative measurements of other simulations of free growing dendrites utilizing the anti-trapping formalism [47]. Further, the merging and coalescence properties of the model satisifies the results of the sharp interface and phase field calculations described by Rappaz and co-workers [2], for the case of repulsive grain boundaries. The necessity of back diffusion, and its effect on merger and energy characteristics has been revealed quite effectively. The issue of δ ferrite coarsening was then addressed and the robustness of our model for characterizing delta-ferrite coarsening –which will be completed in a sequel study– was demonstrated.

Though these results are promising, the model has the capabilities to address a wider spectrum of problems beyond delta ferrite coarsening, the model can also be used to study late stage segregation and coarsening during imposed recalescence in Al-Cu and Al-Mg alloys, a new poorly understood process of industrial relevance. In following this route, we discuss below suggestions for future directions of this work. We address such things as, but not limited to, dynamic nucleation, secondary phase transfromation and extension to multi-component alloys.

7.1 Future Work

7.1.1 Self-Consistently Incorporating Dynamic Nucleation

Conventionally in phase field formulations, nucleation is addressed with the Langevin noise terms in the evolution equations. This treament, however elegant, becomes numerically unfeasible as a high frequency of iterations is required to observe a single nucleation event. Presently, there exists two formualtions that circumvent this difficulty in order to acheieve dynamic nulceation.

7.1.1.1 Method I

The first is that by Simmons and co-workers [90; 91; 92; 93], where nucleation is considered explicitly through a stochastic law and rates are matched to those from a real material. The noise fluctuations in conventional models are replaced by a Poisson distribution process whereby areas are transformed from the parent phase to the product phase. This formulation has the following assumptions; (i) the time to nucleate is much less than the time step, Δt, (ii) if one or more nuclei forms in a given cell, the whole cell transforms, and (iii) the number of nuclei forming in time, Δt, is J the nucleation rate, multiplied by Δt. This allows the nucleation process to be approximated by the unity minus zero even probability of the Poisson distribution, P_n,

$$P_n = 1 - \exp(-J\Delta t). \tag{7.1}$$

Generally a random number is generated during simulation and its value compared to that in Eq. (7.1). If the random number is less than P_n, then the cell is transformed,

otherwise not. The nucleation rate, J, can assume a similar form as that derived from classical nucleation theory, can be obtained from any general model or can even be obtained from experimental data. Extension to this model was reported by Li *et al* [75] to consider heterogeneous nucleation during solidificatiton, where now the nucleation rate, J, is also a function of the contact angle, θ.

7.1.1.2 Method II

The second formulation is owed to the work of Gránásy and co-workers for homomgeneous nucleation [94; 70; 71; 95], and for heterogeneous nucleation [96; 97]. Given an energy functional of the form,

$$F = \int d\mathbf{r}\left\{\frac{\epsilon^2 T}{2}(\nabla\phi)^2 + f(\phi, c)\right\}, \tag{7.2}$$

where the free energy density $f(\phi, c) = WTg(\phi) + [1 - P(\phi)]f_s + P(\phi)f_l$ with W being the barrier height, T being the temperautre, $g(\phi)$ the double well potential, $P(\phi)$ an interpolation function and f_ν $(\nu = s, l)$ being the bulk chemical free energies available in Calphad and other thermodynamic databases. Given the evolution equations, i.e. the Euler Langrange equations, nucleation is modeled by finding the soltuions to the stationary equations,

$$0 = \frac{\delta F}{\delta \phi} \tag{7.3}$$

and

$$0 = \nabla\left[\Gamma_c \nabla \frac{\delta F}{\delta c}\right]. \tag{7.4}$$

For spherical symmetry, the phase field equation reduces to

$$\frac{\partial^2\phi}{\partial r^2} + \frac{2}{r}\frac{\partial\phi}{\partial r} = \frac{\Delta\mu(\phi, c)}{\epsilon^2 T} \tag{7.5}$$

where $\Delta\mu(\phi, c)$ is a chemical potential difference relative to that of the initial liquid. The energy required for a critical fluctuation, i.e. nucleation, is $W^* = F - F_o$. Variable F is calculated numerically by insertion of the solution of Eq. (7.5) and F_o is the energy of the initial liquid. W^* is the compared to the energy from classical nucleation theory W^*_{CNT}. The nucleation rate is then calculated as $J = J_o \exp(-W^*/kT)$.

Nulceation is then considered in simulations by: (i) inclusion of white noise of sufficient amplitude that forces nucleation; (ii) the simulation domain is seperated into domains according to location compositions. Stationary solutions are found for these compositions and critical fluctuations are placed according to a Poisson distribution every time step.

7.1.2 Secondary Phase Transformation and Multi-Component Alloys

The model developed in this work can in general be extended to naturally consider a secondary phase transfromation, from solid A to solid B. The multi-phase field approach makes this extension possible, however it is the self consistent derivation from a single energy functional that would truly determine the feasiblitiy of such an extension.

A possible direction that maybe be considered is the introduction of a new multi-oriented order parameter to represent the infinite orientations of the new nulceated solid B growing in the matirx of solid A. Such an energy functional can be

$$F(c, \vec{\phi}, \vec{\Phi}, T) = \int d\mathbf{r} \left\{ \sum_{i=1}^{N} \frac{|\epsilon(\vec{\phi})\nabla\phi_i|^2}{2} + f(\vec{\phi}, \vec{\Phi}, \nabla\Phi_i, c, T) \right\} \tag{7.6}$$

where the free energy density, $f(\vec{\phi}, \vec{\Phi}, \nabla\Phi_i, c, T)$, describes the energy associated with the primary order parameter(s) but now also contains information concerning the secondary order parameter(s) and its functions which will allow the interpolation between the distinct order parametes. A more indepth and extensive treatement is required to determine if this can be accomplished, even for the simplest case of a dilute binary alloy.

Recently the antitrapping formalism has been extended to a phase field model considering multi-component alloy systems [57]. This, however deals only with single phase, single grain solidification. There is still then, a need for a formulation that is capable of polycrystalline multi-component multi-phase solidification. And if the above mentioned transformation extension is successful, then we have a basis from which we can proceed with further improvements.

Appendix A

Derivation Quantitative Polycrystalline Model

This appendix expands on the work done in Chapter 4, where we showed the main steps and equations of the calculation. The following will go through a step by step derivation of the quantitative multi-phase field model built upon the work of [41].

We start by describing a dilute binary alloy having N crystals of varying orientation described a set of order parameters, ϕ_i $(1 \leq i \leq N)$, such that $\phi_i = 0$ is liquid and $\phi_i = 1$ is solid. Representing the system by a state vector, $\vec{\phi}$, liquid is then $\vec{\phi} = 0$, solid is i is $\vec{\phi} = \hat{e}_i \equiv (0, 0, 0, \ldots, \phi_i = 1, \cdots, 0, 0, 0)$ and overlap of grains is $\vec{\phi} \equiv (0 \cdots \phi_i, \cdots \phi_j, \cdots, \phi_k, \cdots)$ where $0 < \phi_i, \phi_j, \phi_k < 1$ where interaction is such that $0 \leq \phi_i + \phi_j + \phi_k + \cdots \leq 1$.

$$F(c, \vec{\phi}, T) = \int d\mathbf{r} \left\{ \sum_{i=1}^{N} \frac{|\epsilon(\vec{\phi}) \nabla \phi_i|^2}{2} + f(\vec{\phi}, c, T) \right\} \tag{A.1}$$

where $\epsilon(\vec{\phi})$ is the gradient energy coefficient and the free energy density is given

$$\begin{aligned} f(\vec{\phi}, c, T) =& H \sum_{i}^{N} f_{\mathrm{D}}(\phi_i) + f_{\mathrm{int}}(\vec{\phi}) + \frac{RT_m}{v_o} \left[c \ln c - c \right] \\ &+ f^A(T_m) - \Delta T \left[s_l - \frac{L}{T_m} \tilde{g}(\vec{\phi}) \right] + \left[\epsilon_L + \Delta \epsilon \bar{g}(\vec{\phi}) \right] c. \end{aligned} \tag{A.2}$$

The constant H is the barrier height between liquid and solid, $L = T_m(s_l - s_s)$ the latent heat of fusion,

$$f_{\mathrm{D}}(\phi_i) = \phi_i^2(1-\phi_i)^2 \tag{A.3}$$

is the standard double well potential providing $2N$ minima wells. f_{int} sets the energy for interaction. $f^A(T_m)$, is the free energy of pure A calculated at its melting temperature T_m, $\Delta T = T - T_m$, R is the natural gas constant and v_o is the molar volume of solid. Entropy is given by s_x, internal energy by ϵ_x, where $x = s$ or l. The function $\tilde{g}(\vec{\phi})$ and $\bar{g}(\vec{\phi})$ are yet undetermined interpolation function for entropy and internal energy respectively. $\tilde{g}(\vec{\phi} = 0) = 0$, $\tilde{g}(\vec{\phi} = \hat{e}_i) = 1$ and $0 < \tilde{g}(\vec{\phi}) < 1$ and $\bar{g}(\vec{\phi})$ has the same limits.

$$\mu \equiv \frac{\partial f(\vec{\phi}, c)}{\partial c} = \frac{RT_m}{v_o}\ln c + \epsilon_l + \Delta\epsilon\bar{g}(\vec{\phi}) \tag{A.4}$$

A.1 Phase Diagram

At equilibrium, solid-liquid co-existence, in bulk solid grain $i(\vec{\phi}_o = \hat{e}_i)$ and bulk liquid$(\vec{\phi}_o = 0)$, we obtain

$$\begin{aligned}\mu_s^{\mathrm{eq}} &= \frac{RT_m}{v_o}\ln c_s + \Delta\epsilon + \epsilon_l \\ \mu_l^{\mathrm{eq}} &= \frac{RT_m}{v_o}\ln c_l + \epsilon_l\end{aligned} \tag{A.5}$$

in equilibrium $\mu_s^{\mathrm{eq}} = \mu_l^{\mathrm{eq}} \equiv \mu_{\mathrm{eq}}$ giving us the partition coefficient;

$$\begin{aligned}
\frac{RT_m}{v_o}\ln c_s + \Delta\epsilon + \epsilon_l &= \frac{RT_m}{v_o}\ln c_l + \epsilon_l \\
\ln\frac{c_s}{c_l} &= -\frac{v_o\Delta\epsilon}{RT_m} \\
k \equiv \frac{c_s}{c_l} &= \exp\left(-\frac{v_o\Delta\epsilon}{RT_m}\right)
\end{aligned} \tag{A.6}$$

Performing a double tangent construction, with $f(c_s, \vec{\phi}_o = \hat{e}_i) - f(c_l, \vec{\phi}_o = \mathbf{0}) = \mu_{\text{eq}}(c_s - c_l)$, we get μ_{eq} and can get a relationship for the liquid line

$$\begin{aligned}
f(c_s, \vec{\phi}_o = \hat{e}_i) - f(c_l, \vec{\phi}_o = \mathbf{0}) &= \mu_{\text{eq}}(c_s - c_l) \\
-\Delta T s_s + \frac{RT_m}{v_o}(c_s\ln c_s - c_s) + c_s\epsilon_s - & \\
\left(-\Delta T s_l + \frac{RT_m}{v_o}(c_l\ln c_l - c_l) + c_l\epsilon_l\right) &= \mu_{\text{eq}}(c_s - c_l) \\
-\Delta T s_s + \frac{RT_m}{v_o}c_s\ln c_s - \frac{RT_m}{v_o}c_s + c_s\epsilon_s - & \\
\left(-\Delta T s_l + \frac{RT_m}{v_o}c_l\ln c_l - \frac{RT_m}{v_o}c_l + c_l\epsilon_l\right) &= \mu_{\text{eq}}(c_s - c_l) \\
-\Delta T s_s + \frac{RT_m}{v_o}c_s\ln c_s - \frac{RT_m}{v_o}c_s + c_s\epsilon_s + \Delta T s_l - \frac{RT_m}{v_o}c_l\ln c_l + \frac{RT_m}{v_o}c_l - c_l\epsilon_l &= \mu_{\text{eq}}(c_s - c_l) \\
-\Delta T s_s + \Delta T s_l + \frac{RT_m}{v_o}c_s\ln c_s - \frac{RT_m}{v_o}c_s + c_s\epsilon_s - \mu_{\text{eq}}c_s & \\
= \frac{RT_m}{v_o}c_l\ln c_l - \frac{RT_m}{v_o}c_l + c_l\epsilon_l - \mu_{\text{eq}}c_l &
\end{aligned} \tag{A.7}$$

substituting the definition of μ_{eq} from Eq. (A.5) and latent heat we have

$$-\frac{\Delta TL}{T_m}+\frac{RT_m}{v_o}c_s\ln c_s-\frac{RT_m}{v_o}c_s+c_s\epsilon_s-\frac{RT_m}{v_o}c_s\ln c_s-c_s\epsilon_s$$

$$=\frac{RT_m}{v_o}c_l\ln c_l-\frac{RT_m}{v_o}c_l+c_l\epsilon_l-\frac{RT_m}{v_o}c_l\ln c_l-c_l\epsilon_l$$

$$-\frac{\Delta TL}{T_m}=\frac{RT_m}{v_o}(c_l-c_s)$$

$$-\frac{\Delta TL}{T_m}=\frac{RT_m}{v_o}(c_l-kc_l)$$

$$\Delta T=-\frac{RT_m^2(1-k)}{Lv_o}c_l$$

$$T-T_m=-\frac{RT_m^2(1-k)}{Lv_o}c_l$$

$$T=T_m-\frac{RT_m^2(1-k)}{Lv_o}c_l \tag{A.8}$$

(A.9)

and recognizing that $T=T_m+m_lc_l$, then we have

$$m_l=-\frac{RT_m^2(1-k)}{Lv_o}. \tag{A.10}$$

A.2 Equilibrium Steady State profiles

A.2.1 Concentration: $c_o(\vec{\phi}_o(\mathbf{r}))$

In concentration we must consider the solution to the stationary equation corresponding to

$$\begin{aligned}
\frac{\delta F}{\delta c} &= \mu_{\text{eq}} \\
\frac{RT_m}{v_o}\ln c_o(\mathbf{r}) + \epsilon_l + \Delta\epsilon\bar{g}(\vec{\phi}_o(\mathbf{r})) &= \mu_{\text{eq}} \\
\ln c_o(\mathbf{r}) &= \frac{v_o}{RT_m}(\mu_{\text{eq}} - \Delta\epsilon\bar{g}(\vec{\phi}_o(\mathbf{r})) - \epsilon_l) \\
c_o(\mathbf{r}) &= \exp\left\{\frac{v_o}{RT_m}\left(\mu_{\text{eq}} - \Delta\epsilon\bar{g}(\vec{\phi}_o(\mathbf{r})) - \epsilon_l\right)\right\}
\end{aligned} \tag{A.11}$$

If we consider equilibrium in bulk liquid, then $\mathbf{r} \to \infty, \vec{\phi}_o(\mathbf{r}) \to 0$ and $c_o(\mathbf{r}) \to c_o^l$, the equilibrium liquid concentration

$$\begin{aligned}
c_o(\infty) = c_o^l &= \exp\left\{\frac{v_o}{RT_m}\left(\mu_{\text{eq}} - \Delta\epsilon\bar{g}(0) - \epsilon_l\right)\right\} \\
c_o^l &= \exp\left\{\frac{v_o}{RT_m}\mu_{\text{eq}} - \frac{v_o}{RT_m}\epsilon_l\right\},
\end{aligned} \tag{A.12}$$

from Eq. (A.11)

$$\frac{v_o}{RT_m}\mu_{\text{eq}} = \ln c_o(\mathbf{r}) + \frac{v_o}{RT_m}\Delta\epsilon\bar{g}(\vec{\phi}_o(\mathbf{r})) + \frac{v_o}{RT_m}\epsilon_l, \tag{A.13}$$

substituting into Eq. (A.12)

$$
\begin{aligned}
c_o^l = \exp\left[\ln c_o(\mathbf{r})\right] \exp\left[\frac{v_o}{RT_m}\Delta\epsilon\bar{g}(\vec{\phi}_o(\mathbf{r}))\right] \exp\left[\frac{v_o}{RT_m}\epsilon_l\right] \exp\left[-\frac{v_o}{RT_m}\epsilon_l\right] \\
c_o^l = c_o(\mathbf{r}) \exp\left[\frac{v_o\Delta\epsilon}{RT_m}\bar{g}(\vec{\phi}_o(\mathbf{r}))\right] \\
c_o(\mathbf{r}) = c_o^l \exp\left[-\frac{v_o\Delta\epsilon}{RT_m}\bar{g}(\vec{\phi}_o(\mathbf{r}))\right] \\
c_o(\vec{\phi}_o(\mathbf{r})) = c_o^l \exp\left[\ln k\,\bar{g}(\vec{\phi}_o(\mathbf{r}))\right]
\end{aligned}
\tag{A.14}
$$

A.2.2 Phase Field: ϕ_i^o

For the phase field, the equilibrium steady state across a solid-liquid interface, is the stationary solution of the variation with respect to ϕ_i. Considering isotropic and one dimensional for simplicity

$$
\begin{aligned}
\frac{\delta F}{\delta \phi_i} &= 0 \\
\epsilon^2\frac{d^2\phi_i^o}{dx^2} - \frac{\partial f_D(\phi_i^o)}{\partial\phi_i^o} - \frac{\partial f_{\text{int}}(\vec{\phi}_o)}{\partial\phi_i^o} + \left[-\frac{\Delta TL}{T_m}\frac{\partial\bar{g}(\vec{\phi}_o)}{\partial\phi_i^o} - \Delta\epsilon\frac{\partial\bar{g}(\vec{\phi}_o)}{\partial\phi_i^o}c_o(\vec{\phi}_o(\mathbf{r}))\right] &= 0 \\
\epsilon^2\frac{d^2\phi_i^o}{dx^2} - \frac{\partial f_D(\phi_i^o)}{\partial\phi_i^o} - \frac{\partial f_{\text{int}}(\vec{\phi}_o)}{\partial\phi_i^o} &= \frac{\Delta TL}{T_m}\frac{\partial\bar{g}(\vec{\phi}_o)}{\partial\phi_i^o} + \Delta\epsilon\frac{\partial\bar{g}(\vec{\phi}_o)}{\partial\phi_i^o}c_o(\vec{\phi}_o(\mathbf{r}))
\end{aligned}
\tag{A.15}
$$

Let us simplify the right hand side (R.H.S) of Eq. (A.15)

$$\begin{aligned}
\text{R.H.S} &= \frac{\Delta TL}{T_m}\frac{\partial\frac{\partial\tilde{g}(\vec{\phi}_o)}{\partial\phi_i^o}}{\partial\phi_i^o} + \Delta\epsilon\frac{\partial\frac{\partial\bar{g}(\vec{\phi}_o)}{\partial\phi_i^o}}{\partial\phi_i^o}c_o(\vec{\phi}_o(\mathbf{r})) \\
&= \frac{\Delta TL}{T_m}\left[\frac{\partial\tilde{g}(\vec{\phi}_o)}{\partial\phi_i^o} + \frac{T_m}{\Delta TL}\Delta\epsilon\frac{\partial\bar{g}(\vec{\phi}_o)}{\partial\phi_i^o}\right] \\
\text{with } \Delta T &= -\frac{RT_m^2}{Lv_o}(1-k)c_o^l \\
\text{R.H.S} &= -\frac{RT_m^2L}{Lv_oT_m}(1-k)c_o^l\left[\frac{\partial\tilde{g}(\vec{\phi}_o)}{\partial\phi_i^o} - \frac{Lv_oT_m}{RT_m^2L(1-k)c_o^l}\Delta\epsilon\frac{\partial\bar{g}(\vec{\phi}_o)}{\partial\phi_i^o}c_o(\vec{\phi}_o(\mathbf{r}))\right] \\
&= -\frac{RT_m}{v_o}(1-k)c_o^l\left[\frac{\partial\tilde{g}(\vec{\phi}_o)}{\partial\phi_i^o} - \frac{\Delta\epsilon v_o}{RT_m}\frac{1}{(1-k)c_o^l}\frac{\partial\bar{g}(\vec{\phi}_o)}{\partial\phi_i^o}c_o(\vec{\phi}_o(\mathbf{r}))\right] \\
&= -\frac{RT_m}{v_o}(1-k)c_o^l\left[\frac{\partial\tilde{g}(\vec{\phi}_o)}{\partial\phi_i^o} + \frac{\ln k}{(1-k)c_o^l}\frac{\partial\bar{g}(\vec{\phi}_o)}{\partial\phi_i^o}c_o(\vec{\phi}_o(\mathbf{r}))\right] \\
\text{with } \frac{\Delta TL}{T_m} &= -\frac{RT_m}{v_o}(1-k)c_o^l \\
\text{R.H.S} &= \frac{\Delta TL}{T_m}\frac{1}{1-k}\left[\frac{\partial\tilde{g}(\vec{\phi}_o)}{\partial\phi_i^o}(1-k) + \ln k\frac{c_o(\vec{\phi}_o(\mathbf{r}))}{c_o^l}\frac{\partial\bar{g}(\vec{\phi}_o)}{\partial\phi_i^o}\right] \\
\text{and from Eq. (A.10) } L &= -\frac{RT_m^2}{m_lv_o}(1-k) \\
\text{R.H.S} &= -\frac{\Delta TL}{T_m}\frac{RT_m^2}{m_lv_o}(1-k)\frac{1}{1-k}\left[\frac{\partial\tilde{g}(\vec{\phi}_o)}{\partial\phi_i^o}(1-k) + \ln k\frac{c_o(\vec{\phi}_o(\mathbf{r}))}{c_o^l}\frac{\partial\bar{g}(\vec{\phi}_o)}{\partial\phi_i^o}\right] \\
&= -\Delta T\frac{RT_m}{m_lv_o}\left[\frac{\partial\tilde{g}(\vec{\phi}_o)}{\partial\phi_i^o}(1-k) + \ln k\frac{c_o(\vec{\phi}_o(\mathbf{r}))}{c_o^l}\frac{\partial\bar{g}(\vec{\phi}_o)}{\partial\phi_i^o}\right] \quad \text{(A.16)}
\end{aligned}$$

Rewriting Eq. (A.15)

$$\epsilon^2\frac{d^2\phi_i^o}{dx^2} - \frac{\partial f_D(\phi_i^o)}{\partial\phi_i^o} - \frac{\partial f_{\text{int}}(\vec{\phi}_o)}{\partial\phi_i^o} = -\Delta T\frac{RT_m}{m_lv_o}\left[\frac{\partial\tilde{g}(\vec{\phi}_o)}{\partial\phi_i^o}(1-k) + \ln k\frac{c_o(\vec{\phi}_o(\mathbf{r}))}{c_o^l}\frac{\partial\bar{g}(\vec{\phi}_o)}{\partial\phi_i^o}\right]$$

And realizing that for a single solid-liquid interface the interaction energy $f_{\text{int}} = 0$ we have

$$\epsilon^2\frac{d^2\phi_i^o}{dx^2} - \frac{\partial f_D(\phi_i^o)}{\partial\phi_i^o} = -\Delta T\frac{RT_m}{m_lv_o}\left[\frac{\partial\tilde{g}(\vec{\phi}_o)}{\partial\phi_i^o}(1-k) + \ln k\frac{c_o(\vec{\phi}_o(\mathbf{r}))}{c_o^l}\frac{\partial\bar{g}(\vec{\phi}_o)}{\partial\phi_i^o}\right] \quad \text{(A.17)}$$

Looking closely at equation Eq. (A.17), we notice that for generic choices for $\bar{g}(\vec{\phi})$ and $\tilde{g}(\vec{\phi})$, no analytic solutions exist for ϕ_i^o and in general would need to be solved numerically. And more importantly, we recognize that this calculated numeric solution and its properties would depend on the concentration and alloy dependent coefficients on the R.H.S. This however can be avoided if somehow the R.H.S. was made to vanish.

We then take Eq. (A.17)

$$
\begin{aligned}
-\Delta T \frac{RT_m}{m_l v_o}\left[\frac{\partial \tilde{g}(\vec{\phi}_o)}{\partial \phi_i^o}(1-k) + \ln k \frac{c_o(\vec{\phi}_o(\mathbf{r}))}{c_o^l}\frac{\partial \bar{g}(\vec{\phi}_o)}{\partial \phi_i^o}\right] &= 0 \\
\text{then } \epsilon^2 \frac{d^2\phi_i^o}{dx^2} - \frac{\partial f_D(\phi_i^o)}{\partial \phi_i^o} &= 0 \\
\epsilon^2 \frac{d^2\phi_i^o}{dx^2} - 2H\phi_i^o(1-2\phi_i^o)(1-\phi_i^o) &= 0 \qquad \text{(A.18)}
\end{aligned}
$$

It has been shown, that Eq. (A.18) yields the equilibrium solution of

$$
\phi_i^o(x) = \frac{1}{2}\left[1 - \tanh\left(\frac{x}{\sqrt{2}W_o}\right)\right] \qquad \text{(A.19)}
$$

Where a new length scale, the interface (solid-liquid) width, has been introduced, $W_o = \epsilon_{sl}/\sqrt{H}$. We can now turn our attention to the R.H.S portion of the equation and realize how it can be made to vanish. Taking

$$-\Delta T \frac{RT_m}{m_l v_o}\left[\frac{\partial \tilde{g}(\vec{\phi}_o)}{\partial \phi_i^o}(1-k) + \ln k \frac{c_o(\vec{\phi}_o(\mathbf{r}))}{c_o^l}\frac{\partial \bar{g}(\vec{\phi}_o)}{\partial \phi_i^o}\right] = 0$$

$$\frac{\partial \tilde{g}(\vec{\phi}_o)}{\partial \phi_i^o}(1-k) + \ln k \frac{c_o(\vec{\phi}_o(\mathbf{r}))}{c_o^l}\frac{\partial \bar{g}(\vec{\phi}_o)}{\partial \phi_i^o} = 0 \tag{A.20}$$

$$\text{from Eq. A.14 } \frac{c_o(\vec{\phi}_o(\mathbf{r}))}{c_o^l} = \exp\left[\ln k\, \bar{g}(\vec{\phi}_o(\mathbf{r}))\right]$$

$$\frac{\partial \tilde{g}(\vec{\phi}_o)}{\partial \phi_i^o}(1-k) + \ln k \exp\left[\ln k\, \bar{g}(\vec{\phi}_o(\mathbf{r}))\right]\frac{\partial \bar{g}(\vec{\phi}_o)}{\partial \phi_i^o} = 0$$

$$\frac{\partial \tilde{g}(\vec{\phi}_o)}{\partial \phi_i^o} = -\frac{\ln k}{(1-k)}\frac{\partial \bar{g}(\vec{\phi}_o)}{\partial \phi_i^o}\exp\left[\ln k\, \bar{g}(\vec{\phi}_o(\mathbf{r}))\right] \tag{A.21}$$

OR

$$\frac{\partial \bar{g}(\vec{\phi}_o)}{\partial \phi_i^o} = -\frac{1-k}{\ln k}\frac{\partial \tilde{g}(\vec{\phi}_o)}{\partial \phi_i^o}\exp\left[-\ln k\, \bar{g}(\vec{\phi}_o(\mathbf{r}))\right] \tag{A.22}$$

If we take the condition for $\partial \tilde{g}(\vec{\phi}_o)/\partial \phi_i^o$ in Eq. (A.2.2) and integrate it with respect to $\vec{\phi}_o$ then

$$\tilde{g}(\vec{\phi}_o) = -\frac{1}{(1-k)}\exp\left[\ln k\, \bar{g}(\vec{\phi}_o(\mathbf{r}))\right] + Const$$

$$\text{solving for } Const\ \tilde{g}(\vec{\phi}_o = 0) = 0 = -\frac{1}{(1-k)} + Const$$

$$Const = \frac{1}{(1-k)}$$

$$\text{giving } \tilde{g}(\vec{\phi}_o) = \frac{1 - \exp\left[\ln k\, \bar{g}(\vec{\phi}_o(\mathbf{r}))\right]}{(1-k)} \tag{A.23}$$

OR

$$1 - (1-k)\tilde{g}(\vec{\phi}_o) = -\exp\left[\ln k\, \bar{g}(\vec{\phi}_o(\mathbf{r}))\right]$$

$$\ln k\, \bar{g}(\vec{\phi}_o) = \ln\left[1 - (1-k)\tilde{g}(\vec{\phi}_o)\right] \tag{A.24}$$

Using Eq. (A.24) and taking the exponential of both sides we get

$$\exp\left[\ln k\,\bar{g}(\vec{\phi}_o)\right] = \exp\left\{\ln\left[1-(1-k)\tilde{g}(\vec{\phi}_o)\right]\right\}$$
$$\text{and from Eq. (A.14) } \exp\left[\ln k\,\bar{g}(\vec{\phi}_o)\right] = \frac{c_o(\vec{\phi}_o(\mathbf{r}))}{c_o^l}$$
$$c_o(\vec{\phi}_o(\mathbf{r})) = c_o^l\left[1-(1-k)\tilde{g}(\vec{\phi}_o)\right]. \tag{A.25}$$

For the situation where we have a solid-solid boundary, we still wish that the steady state solution is free from contamination from concentration and alloy dependent coefficients. The interaction energy however, will not be zero and the following equations must be solved numerically;

$$W_o^2\frac{d^2\phi_i^o}{dx^2} - \frac{\partial f_D(\phi_i^o)}{\partial\phi_i^o} - \frac{1}{H}\frac{\partial f_{\text{int}}(\vec{\phi}_o)}{\partial\phi_i^o} = 0$$
$$W_o^2\frac{d^2\phi_j^o}{dx^2} - \frac{\partial f_D(\phi_j^o)}{\partial\phi_j^o} - \frac{1}{H}\frac{\partial f_{\text{int}}(\vec{\phi}_o)}{\partial\phi_j^o} = 0. \tag{A.26}$$

A.3 Simplifying The Free Energy Density

We wish to take the free energy density $f(\vec{\phi}, c, T)$, and simplify the form it assumes entering the equations of motion. We start with

$$f(\vec{\phi},c,T) = H\sum_{i}^{N} f_{\mathrm{D}}(\phi_i) + f_{\mathrm{int}}(\vec{\phi}) + \frac{RT_m}{v_o}\left[c\ln c - c\right]$$
$$+f^{A}(T_m) - \Delta T\left[s_l - \frac{L}{T_m}\tilde{g}(\vec{\phi})\right] + \left[\epsilon_L + \Delta\epsilon\bar{g}(\vec{\phi})\right]c$$
$$\frac{\partial f(\vec{\phi},c,T)}{\partial\phi_i} = -\frac{\partial f_D}{\partial\phi_i} - \frac{\partial f_{\mathrm{int}}}{\partial\phi_i}$$
$$+\left[\frac{-\Delta TL}{T_m}\frac{\partial\tilde{g}}{\partial\phi_i} - \Delta\epsilon\frac{\partial\bar{g}}{\partial\phi_i}c(\vec{\phi})\right]$$

from Eqs. (A.22) and (A.24) we can write it in terms of just $\frac{\partial\tilde{g}}{\partial\phi_i^o}$

$$= -\frac{\partial f_D}{\partial\phi_i} - \frac{\partial f_{\mathrm{int}}}{\partial\phi_i} + \left[-\frac{\Delta TL}{T_m} + \frac{\Delta\epsilon(1-k)}{\ln k}\frac{1}{[1-(1-k)\tilde{g}(\vec{\phi}_o)]}c_o(\vec{\phi}_o)\right]\frac{\partial\tilde{g}}{\partial\phi_i}$$
$$= -\frac{\partial f_D}{\partial\phi_i} - \frac{\partial f_{\mathrm{int}}}{\partial\phi_i} + \left[-\frac{\Delta TL}{T_m} + \frac{\Delta\epsilon(1-k)}{\ln k}\frac{1}{[1-(1-k)\tilde{g}(\vec{\phi})]}\frac{c_o^l}{c_o^l}c(\vec{\phi})\right]\frac{\partial\tilde{g}}{\partial\phi_i}$$
$$= -\frac{\partial f_D}{\partial\phi_i} - \frac{\partial f_{\mathrm{int}}}{\partial\phi_i} - \left[\frac{\Delta TL}{T_m} - \frac{\Delta\epsilon\, c(\vec{\phi})(1-k)}{\ln k}\frac{c_o^l}{c_o(\vec{\phi}_o)}\right]\frac{\partial\tilde{g}}{\partial\phi_i}$$
$$= -\frac{\partial f_D}{\partial\phi_i} - \frac{\partial f_{\mathrm{int}}}{\partial\phi_i} - \frac{c_o^l\Delta\epsilon(1-k)}{\ln k\, c_o(\vec{\phi}_o)}\left[\frac{\Delta TL}{T_m}\frac{\ln k}{\Delta\epsilon\, c_o^l(1-k)}c_o(\vec{\phi}_o) - c(\vec{\phi})\right]\frac{\partial\tilde{g}}{\partial\phi_i} \qquad \text{(A.27)}$$
$$\text{with } L = -\frac{RT_m^2}{m_l v_o}(1-k)$$

we look at the first term in [ ] brackets

$$\frac{\Delta TL}{T_m}\frac{\ln k}{\Delta\epsilon\, c_o^l(1-k)} = -\frac{RT_m^2}{m_l v_o}(1-k)\frac{\Delta T}{T_m}\frac{\ln k}{\Delta\epsilon c_o^l(1-k)}$$
$$= -\frac{RT_m}{\Delta\epsilon v_o}\frac{\ln k\,\Delta T}{m_l c_o^l}$$
$$= \frac{1}{\ln k}\frac{\ln k\,\Delta T}{m_l c_o^l}$$
$$= \frac{\Delta T}{m_l c_o^l} = \frac{\Delta T}{\Delta T} = 1$$

(A.28)

$$\text{from Eq. (A.2.2)} \frac{1}{c_o(\vec{\phi}_o)} \frac{\partial \tilde{g}}{\partial \phi_i} = -\frac{\ln k}{(1-k)c_o^l} \frac{\partial \bar{g}}{\partial \phi_i}$$

$$\text{looking at the terms multiplying the [ ] brackets}$$

$$\frac{c_o^l \Delta\epsilon(1-k)}{\ln k} \frac{1}{c_o(\vec{\phi}_o)} \frac{\partial \tilde{g}}{\partial \phi_i} = -\frac{c_o^l \Delta\epsilon(1-k)}{\ln k} \frac{\ln k}{(1-k)c_o^l} \frac{\partial \bar{g}}{\partial \phi_i}$$

$$= -\Delta\epsilon \frac{\partial \bar{g}}{\partial \phi_i} = \frac{RT_m}{v_o} \frac{\partial \bar{g}}{\partial \phi_i} \ln k \tag{A.29}$$

going back to Eq. (A.3)

$$\frac{\partial f(\vec{\phi}, c, T)}{\partial \phi_i} = -\frac{\partial f_D}{\partial \phi_i} - \frac{\partial f_{\text{int}}}{\partial \phi_i} - \frac{RT_m \ln k}{v_o} \left[\frac{\Delta T}{m_l c_o^l} c_o(\vec{\phi}_o) - c \right] \frac{\partial \bar{g}}{\partial \phi_i}$$

$$\text{from Eq. (A.28)} - \frac{\partial f_D}{\partial \phi_i} - \frac{\partial f_{\text{int}}}{\partial \phi_i} - \frac{RT_m \ln k \, \Delta T}{v_o m_l c_o^l} \left[c_o(\vec{\phi}_o) - c \right] \frac{\partial \bar{g}}{\partial \phi_i} \tag{A.30}$$

We get the following equation of motion

$$\frac{1}{HK_{\phi_i}} \frac{\partial \phi_i}{\partial t} = W_o^2 \nabla^2 \phi_i - \frac{\partial f_D(\phi_i)}{\partial \phi_i} - \frac{1}{H} \frac{\partial f_{\text{int}}}{\partial \phi_i} - \frac{RT_m \Delta T}{v_o m_l c_o^l} \left[c_o(\vec{\phi}_o) - c \right] \frac{\partial \bar{g}}{\partial \phi_i}$$

$$\tau \frac{\partial \phi_i}{\partial t} = W_o^2 \nabla^2 \phi_i - \frac{\partial f_D}{\partial \phi_i} - \frac{1}{H} \frac{\partial f_{\text{int}}}{\partial \phi_i} + \frac{1}{H} \frac{RT_m \ln k \, \Delta T}{v_o m_l} \left[\frac{c - c_o(\vec{\phi}_o)}{c_o^l} \right] \frac{\partial \bar{g}}{\partial \phi_i} \tag{A.31}$$

The phase field equation can be written another way if we so choose. We will define a variable u, a dimensionless chemical potential and proceed.

$$
\begin{aligned}
u &= \frac{v_o}{RT_m}(\mu - \mu_{\text{eq}}) \\
&= \frac{v_o}{RT_m}\left[\frac{RT_m}{v_o}\ln c + \Delta\epsilon\bar{g}(\vec{\phi}) - \frac{RT_m}{v_o}\ln c_o^l\right] \\
&= \ln\frac{c}{c_o^l} + \frac{\Delta\epsilon v_o}{RT_m}\bar{g}(\vec{\phi}) \\
&= \ln\frac{c}{c_o^l} - \ln k\bar{g}(\vec{\phi}) \\
&= \ln\frac{c}{c_o^l} - \ln\left[1-(1-k)\tilde{g}(\vec{\phi})\right] \\
u &= \ln\left[\frac{c}{c_o^l[1-(1-k)\tilde{g}(\vec{\phi})]}\right]
\end{aligned}
\tag{A.32}
$$

Or it can be re-written as

$$
\frac{c}{c_o^l} = e^u[1-(1-k)\tilde{g}(\vec{\phi})] \tag{A.33}
$$

And in following previous works, we introduce another interpolations function $h(\vec{\phi})$, which has the same limits ($h(\vec{\phi}=0)=0$ and $h(\vec{\phi}=\hat{e}_i)=1$) as the other interpolation functions but does not necessarily satisfy $h'(\vec{\phi}=0)=0$ and $h'(\vec{\phi}=\hat{e}_i)=0$. We choose $h(\vec{\phi}) = \sum_i H(\phi_i)$, where $H(\phi_i)=\phi_i$. We then opt to make this exchange in Eq. (A.32)

$$
u = \ln\left[\frac{c}{c_o^l[1-(1-k)h(\vec{\phi})]}\right] \tag{A.34}
$$

And realizing that in doing so Eq. (A.14) also becomes

$$
c_o(\vec{\phi}) = c_o^l\left[1-(1-k)h(\vec{\phi})\right]. \tag{A.35}
$$

We take Eq. (A.33) and revisit Eq. (A.31), specifically the collection of concentration terms in [ ] brackets.

$$\frac{c - c_o(\vec{\phi}_o)}{c_o^l} = \frac{c}{c_o^l} - \frac{c(\vec{\phi}_o)}{c_o^l}$$

$$\text{using Eqs. (A.33) and (A.25)} \quad = e^u[1-(1-k)\tilde{g}(\vec{\phi})] - [1-(1-k)\tilde{g}(\vec{\phi})]$$

$$\frac{c - c_o(\vec{\phi}_o)}{c_o^l} = [1-(1-k)\tilde{g}(\vec{\phi})](e^u - 1) \tag{A.36}$$

with

$$\begin{aligned}\frac{\partial \bar{g}}{\partial \phi_i} &= -\frac{1-k}{\ln k}\frac{\partial \tilde{g}}{\partial \phi_i}\exp\left[-\ln k\,\bar{g}(\vec{\phi})\right] \\ &= -\frac{1-k}{\ln k}\frac{\partial \tilde{g}}{\partial \phi_i}\frac{1}{[1-(1-k)\tilde{g}(\vec{\phi})]}\end{aligned} \tag{A.37}$$

We proceed with

$$\begin{aligned}\frac{1}{H}\frac{RT_m \ln k\,\Delta T}{v_o m_l}\frac{c - c_o(\vec{\phi}_o)}{c_o^l}\bar{g}(\vec{\phi}) &= \frac{1}{H}\frac{RT_m \ln k\,\Delta T}{v_o m_l}[1-(1-k)\tilde{g}(\vec{\phi})](e^u-1)\frac{\partial \bar{g}}{\partial \phi_i} \\ &= -\frac{1}{H}\frac{RT_m \ln k\,\Delta T}{v_o m_l}\frac{1-k}{\ln k}\frac{\partial \tilde{g}}{\partial \phi_i}\frac{[1-(1-k)\tilde{g}(\vec{\phi})](e^u-1)}{[1-(1-k)\tilde{g}(\vec{\phi})]} \\ &= -\frac{1}{H}\frac{RT_m \ln k\,\Delta T}{v_o m_l}\frac{1-k}{\ln k}\frac{\partial \tilde{g}}{\partial \phi_i}(e^u-1) \\ &= -\frac{1}{H}\frac{RT_m \ln k\,\Delta T}{v_o m_l}\frac{1-k}{1-k}\frac{c_o^l}{c_o^l}\frac{1-k}{\ln k}\frac{\partial \tilde{g}}{\partial \phi_i}(e^u-1) \\ &= -\frac{1}{H}\frac{RT_m(1-k)^2 c_o^l}{v_o}\frac{\Delta T}{m_l c_o^l}\frac{\partial \tilde{g}}{\partial \phi_i}\frac{(e^u-1)}{1-k} \\ \frac{1}{H}\frac{RT_m \ln k\,\Delta T}{v_o m_l}\frac{c - c_o(\vec{\phi}_o)}{c_o^l}\bar{g}(\vec{\phi}) &= -\frac{1}{H}\frac{RT_m(1-k)^2 c_o^l}{v_o}\frac{\partial \tilde{g}}{\partial \phi_i}\frac{(e^u-1)}{1-k}\end{aligned} \tag{A.38}$$

Substituting Eq. (A.38) back into Eq. (A.31)

$$\begin{aligned}\tau\frac{\partial\phi_i}{\partial t} &= W_o^2\nabla^2\phi_i - \frac{\partial f_D}{\partial\phi_i} - \frac{1}{H}\frac{\partial f_{\text{int}}}{\partial\phi_i} + \frac{1}{H}\frac{RT_m \ln k\,\Delta T}{v_o m_l}\left[\frac{c-c_o}{c_o^l}\right]\frac{\partial\bar{g}}{\partial\phi_i} \\ &= W_o^2\nabla^2\phi_i - \frac{\partial f_D}{\partial\phi_i} - \frac{1}{H}\frac{\partial f_{\text{int}}}{\partial\phi_i} - \frac{1}{H}\frac{RT_m(1-k)^2}{v_o}\frac{\partial\tilde{g}}{\partial\phi_i}\frac{(e^u-1)}{1-k} \\ &= W_o^2\nabla^2\phi_i - \frac{\partial f_D}{\partial\phi_i} - \frac{1}{H}\frac{\partial f_{\text{int}}}{\partial\phi_i} - \frac{\lambda}{1-k}(e^u-1)\frac{\partial\tilde{g}}{\partial\phi_i}\end{aligned} \tag{A.39}$$

And we have defined

$$\lambda = \frac{1}{H}\frac{RT_m(1-k)^2 c_o^l}{v_o} \tag{A.40}$$

Concentration equation follows nonvariationally

$$\frac{\partial c}{\partial t} = \vec{\nabla}\cdot\left(D_l q(\vec{\phi})c\vec{\nabla}u + \vec{j_{\text{at}}}\right). \tag{A.41}$$

Where a new, so-called "anti-rapping current $\vec{J}_{\text{at}}$ has been introduced, which corrects for solute trapping due to thickness of the interface. In this work, the current assumes the form

$$\vec{j}_{\text{at}} = a_t(\vec{\phi})W_o c_o^l e^u \sum_i^N \frac{\partial\phi_i}{\partial t}\frac{\vec{\nabla}\phi_i}{|\vec{\nabla}\phi_i|} \tag{A.42}$$

The anti-trapping coefficient, $a_t(\vec{\phi})$, simply relates the different bulk diffusion through

$$a_t(\vec{\phi}) = \frac{(h(\vec{\phi})-1)(1-q(\vec{\phi}))}{\sqrt{2}(\sum_i \phi_i^2 - 1)} \tag{A.43}$$

where $q(\vec{\phi})$ interpolates between diffusion coefficients. For the case of one sided diffusion $a_t = 1/2\sqrt{2}$ which is the coefficient that has been used in previous studies.

Bibliography

[1] D. A. Porter and K. E. Easterling. *Phase Transformations in Metals and Alloys 2nd ed.* Stanley Thornes Ltd, 2001.

[2] M. Rappaz, A. Jacot, and W. J. Boettinger. *Metallurgical and Materials Transactions A*, 34(3):467–479, 2003.

[3] Y. Saito. *Statistical Phsyics of Crystal Growth*, page 629. World Scientific Publishing Co. Pte. Ltd., 1996.

[4] G. P. Ivantsov. *Dokl. Akad. Nauk USSR*, 58:1113, 1947.

[5] W. W. Mullins and R. F. Sekerka. *J. Appl. Phys.*, **34**:323, 1963.

[6] W. W. Mullins and R. F. Sekerka. *J. Appl. Phys.*, **35**:444, 1964.

[7] W. Kurz and D. J. Fisher. *Acta Metall.*, **29**:11, 1981.

[8] J. D. Hunt. *Solidification and Casting of Metals.* The Metals Society, London, 1979.

[9] D. Bouchard and J. S. Kirkaldy. *Met. and Mater. Trans. B*, **28B**:651, 1997.

[10] J. Bragard, A. Karma, Y. H. Lee, and M. Plapp. *Interface Sci.*, 10:121, 2002.

[11] H. V. Atkinson. *Acta. Metall.*, 36:469–491, 1988.

[12] P. W. Voorhees. *Annu. Rev. Mater. Sci.*, 22:197–215, 1992.

[13] G. S. Rohrer. *Annu. Rev. Mater. Sci.*, 35:99–126, 2005.

[14] P. A. Beck, J. C. Kremer, and L. Demer. *Phys. Rev.*, 71:555, 1947.

[15] J. E. Burke. *J. Appl. Phys.*, 18:73–91, 1947.

[16] P. A. Beck, M. L. Holzworth, and H. Hu. *Phys. Rev.*, 73:526–527, 1947.

[17] J. E. Burke. *Trans. Metall. Soc. AIME*, 180:1028, 1949.

[18] E. Grey and G. Higgins. *Acta. Metall.*, 4:309–321, 1973.

[19] K. Lücke and K. Detert. *Acta. Metall.*, 11:628–637, 1957.

[20] J. W. Cahn. *Acta. Metall.*, 10:789–798, 1962.

[21] C. Zener. *Reans. Metall. Soc. AIME*, 175:15–51, 1948.

[22] G. W. Greenwood. *Acta. Metall.*, 4:243–248, 1956.

[23] V. E. Fradkov and D. Udler. Two-dimensional normal grain growth: topological aspects. *Advances in Physics*, 43:739–789, 1994.

[24] D. R. Poirier, S. Ganesan, M. Andrewst, and P. Ocansey. Isothermal coarsening of dendritic equiaxial grains in a1-15.6wt.%cu alloy. *Mat. Sci. Eng. A*, 148:289–297, 1991.

[25] L. Arnberg, G. Chai, and L. Bäckerud. *Mat. Sci. Eng. A*, 173:101–103, 1993.

[26] G. Chai, L. Bäckerud, T. Rolland, and L. Arnberg. *Metall. Mat. Trans. A*, 26A:965, 1995.

[27] N. L. M. Veldman, A. R. Dahle, D. H. St.John, and L. Arnberg. *Metall. Mat. Trans. A*, 32A:147, 2001.

[28] N. Wang aand S. Mokadem and M. Rappaz andW. Kurz. *Acta Materialia*, 52:3173–3182, 2004.

[29] V. Mathier, A. Jacot, , and M. Rappaz. *Modelling Simul. Mater. Sci. Eng.*, 12:479–490, 2004.

[30] Q. Du and A. Jacot. *Acta Maeterialia*, 53:3479–3493, 2005.

[31] S. Vernde and M. Rappaz. *Philos. Mag.*, 86:3779–3794, 2006.

[32] P. G. de Gennes. *Rev. Mod. Phys.*, 57(3):827–863, 1985.

[33] P. M. Chaikin and T. C. Lubensky. *Principles of condensed matter physics.* Cambridge University Press, Cambridge, Great Britain, 1995.

[34] G. Caginalp. *Anal. of Phys.*, 172:136, 1986.

[35] G. Caginalp and W. Xie. *Phys. Rev. E*, 48:1897, 1993.

[36] J. A. Warren and W. J. Boettinger. *Acta Metall. Mater. A*, 43:689, 1995.

[37] Y.-T. Kim, N. Provatas, J. Dantzig, and N. Goldenfeld. *Phys. Rev. E*, 59:2546, 1999.

[38] J. H. Jeong, N. Goldenfeld, and J. A. Dantzig. Phase field model for three-dimensional dendritic growth with fluid flow. *Physical Review E*, 64:041602–1–041602–14, 2001.

[39] K. R. Elder, M. Grant, N. Provatas, and J. M. Kosterlitz. *Phys. Rev. E*, **64**:21604, 2001.

[40] W.J. Boettinger, J.A. Warren, C. Beckermann, and A. Karma. *Annu Rev. Mater. Res.*, **32**:163, 2002.

[41] B. Echebarria, R. Folch, A. Karma, and M. Plapp. *Phys. Rev. E.*, 70:061604–1, 2004.

[42] A. Karma and W.-J. Rappel. *Phys. Rev. E*, 53:R3017, 1996.

[43] A. Karma and W.-J. Rappel. *Phys. Rev. E*, 57:4323, 1998.

[44] A. Karma and W.-J. Rappel. *Phys. Rev. E*, 60:3614, 1999.

[45] G. Caginalp. *Arch. Rat. Mech. Anal.*, 92:205, 1986.

[46] A. A. Wheeler, W. J., Boettinger, and G. B. McFadden. *Phys. Rev. A*, 45:7424, 1992.

[47] A. Karma. *Phys. Rev. Lett*, 87:115701, 2001.

[48] S. G. Kim, W. T. Kim, and T. Suzuki. *Phys. Rev. E*, **60**:7186, 1999.

[49] C. Tong, M. Greenwood, and N. Provatas. *Phys. Rev. E*, **77**:1, 2008.

[50] P. R. Cha, D. H. Yeon, and J. K. Yoon. *Acta Mater.*, **49**:3295–3307, 2001.

[51] M. Ode, S. G. Kim, and T. Suzuki. *ISIJ Inter.*, **41**:1076–1082, 2001.

[52] K. Wu and Y. Wang Y. A. Chang and. *Scripta Mater.*, **50**:1145–1150, 2004.

[53] K. Sakai. *J. Crsyt. growth*, **237–239**:144–148, 2002.

[54] S. G. Kim, W. T. Kimb, T. Suzukic, and M. Ode. *Annu. Rev. Mater. Res.*, **261**:135–159, 2004.

[55] B. Nestler, H. Garcke, and B. Stinner. *Phys. Rev. E*, **71**:041609–1, 2005.

[56] R. R. Mohanty and Y. Sohn. *Journal of Phase Equilibria and Diffusion*, **27**:676–683, 2006.

[57] S. G. Kim. *Acta Mater.*, **55**:4391–4399, 2007.

[58] T. Kitashima, J. Wang, and H. Harada. *Intermetallics*, **16**:239–245, 2008.

[59] R. Folch and M. Plapp. *Phys. Rev. E.*, **72**:011602, 2005.

[60] L.-Q. Chen and W. Yang. *Phys. Rev. B*, **50**:15752, 1994.

[61] L.-Q. Chen. *Script. Metall. et Mater.*, **32**:115, 1995.

[62] D. Fan and L.-Q. Chen. *Acta Metallurgica*, **45**:3297, 2002.

[63] D. Fan, S. P. Chen, L.-Q. Chen, and P. W. Voorhees. *Acta Materialia*, **50**:1897, 2002.

[64] J. Z. Zhu, T. Wang, A. J. Ardell, S. H. Zhou, Z. K. Lui, and L. Q. Chen. *Acta Materialia*, **52**:2837, 2004.

[65] J. Z. Zhu, T. Wang, S. H. Zhou, Z. K. Lui, and L. Q. Chen. *Acta Materialia*, **52**:833, 2004.

[66] I. Steinbach, F. Pezzolla, B. Nestler M. Seebelberg, R. Prieler, and G. J. Schmitz. *Physica D*, **94**:135, 1999.

[67] R. Kobayashi, J. A. Warren, and W. C. Carter. *Physica D*, **119**:415, 1998.

[68] J. A. Warren, W. C. Carter, and R. Kobayashi. *Physica (Amsterdam)*, **261A**:159, 1998.

[69] J. A. Warren, R. Kobayashi, A. E. Lobkovsky, and W. C. Carter. *Acta Materialia*, **51**:6035, 2003.

[70] L. Gránásy, T. Pusztai, and T. Börzsönyi. *Physical Review Letters*, **88**:206105–1, 2002.

[71] L. Gránásy, T. Pusztai, and T. Börzsönyi. *Journal of Crystal Growth*, **237-239**:1813, 2002.

[72] L. Gránásy, T. Pusztai, J. A. Warren, J. F. Douglas, T. Börzsönyi, and V. Ferreiro. *Nature of Materials*, **2**:92, 2003.

[73] R. Kobayashi and Y. Giga. *J. Stat. Phys.*, **95**:1187, 1999.

[74] N. Provatas, M., B. Athreya, N. Goldenfeld, and J. Dantzig. *International Journal of Modern Physics B*, 19:4525, 2005.

[75] J. J. Li, J. C. Wang, Q. Xu, and G. C. Yang. *Acta Materialia*, **55**:825, 2007.

[76] J. C. Ramirez, C. Beckermann, A. Karma, and H. J. Diepers. *Phys. Rev. E*, 69:051607, 2004.

[77] M. Greenwood, M. Haataja, and N. Provatas. *Phys. Rev. Lett.*, 93:246101, 2004.

[78] D. Fan and L.-Q. Chen. *Acta Metallurgica*, **45**:611, 1996.

[79] C. E. Krill III and L.-Q. Chen. *Acta Materialia*, **50**:3057, 2002.

[80] N. Moelans, B. Blanpain, and P. Wollants. *Acta Materialia*, **55**:2173, 2006.

[81] N. Provatas, N. Goldenfeld, and J. Dantzig. *Phys. Rev. Lett.*, 80:3308, 1998.

[82] A. Kazaryan, Y. Wang, S. A. Dregia, and B. R. Patton. *Phys. Rev. B*, **61**:275, 2000.

[83] A. Kazaryan, Y. Wang, S. A. Dregia, and B. R. Patton. *Phys. Rev. B*, **63**:184102, 2001.

[84] N. Ma, A. Kazaryan, S. A. Dregia, and Y. Wang. *Acta Materialia*, **52**:3869, 2004.

[85] Mike Greenwood. *Ph.D Thesis.* McMaster University, 2008.

[86] C. Klinkenberg and K.-E. Hensger. *Materials science forum*, 500:253, 2005.

[87] Tihe Zhou. *Ph.D Thesis.* McMaster University, 2008.

[88] J. M. Rodriguez-Ibabe. *Materials science forum*, 500:49, 2005.

[89] K. R. Lottey and M. Militzer. Microstructure evolution in fine-grained microalloyed steels. *Materials science forum*, 500:347, 2005.

[90] J. P. Simmons, C. Shen, , and Y. Wang. *Scripta Materialia*, 43(10):935 – 942, 2000.

[91] C. Shen, J. P. Simmons, K. Wu, and Y. Wang. In M. Fahrmann J. C. Zhao and T. M. Pollock, editors, *Materials Design Approaches and Experiences.* TMS, 2001.

[92] Y. H. Wen, J. P. Simmons, C. Shen, C. Woodward, and Y. Wang. *Acta Materialia*, 51(4):1123 – 1132, 2003.

[93] J. P. Simmons, Y. H. Wen, C. Shen, , and Y. Z. Wang. *Mat. Sci. and Eng. A*, 365(4):136 – 143, 2004.

[94] L. Gránásy, T. Börzsönyi, T. Pusztai, and P. F. James. Critical Comparison of Modern Theories of Crystal Nucleation in Unary and Binary Systems. In O. Minster and B. Schürmann, editors, *Microgravity Research and Aplications in Physical Sciences and Biotechnology*, volume 454 of *ESA Special Publication*, page 629, 2001.

[95] L. Gránásy and T. Pusztai. *Jour. Chem. Phys.*, **117**:10121, 2002.

[96] L. Gránásy, T. Pusztai, T. Börzsönyi, G. I. Tóth, G. Tegze, J. A. Warren, and J. F. Douglas. *Philos. Mag.*, **86**:3757.

[97] L. Gránásy, T. Pusztai, D. Saylor, and J. A. Warren. *Phys. Rev. Lett.*, **98**:035703–1.